

Mechanisms of Shape Transformation and Retraction in Axons

by

Anagha Sanjay Datar



A thesis submitted to the Jawaharlal Nehru University
for the degree of DOCTOR OF PHILOSOPHY

November 2014

DECLARATION

I, hereby, declare that this thesis is composed independently by me at Raman Research Institute, Bangalore, India, under the supervision of Prof. Pramod Pullarkat. The subject matter presented in this thesis has not previously formed the basis of the award of any degree, diploma, associateship, fellowship or any other similar title in any other University.

Prof. Pramod Pullarkat
Raman Research Institute


Anagha Sanjay Datar

CERTIFICATE

This is to certify that the thesis entitled **Mechanisms of Shape Transformation and Retraction in Axons** submitted by Anagha Sanjay Datar for the award of the degree of DOCTOR OF PHILOSOPHY of Jawaharlal Nehru University is her original work. This has not been published or submitted to any other University for any other degree or diploma.

Prof. Ravi Subrahmanyam
Director
Raman Research Institute

Prof. Pramod Pullarkat
Thesis Supervisor

ACKNOWLEDGEMENTS

At this important juncture in my academic life, I feel overcome by the urge to express my feeling of gratitude towards many people who have helped me directly or indirectly in finishing my PhD thesis.

The first and the most due expression of thanks goes to my PhD supervisor, Dr. Pramod Pullarkat who introduced me to the intricate and challenging field of Biophysics and got me started on the experimental work to which I was a complete novice. He showed immense amount of patience throughout these years and constantly encouraged me to tackle the complex problems by breaking them down in logical steps. He was a great pushing force in making me apply for the Charpak Fellowship, which opened the door to an important learning experience in my Phd life. I would like to thank Patricia Bassereau (Institute Curie, Paris) and Thomas Bornschögl who gave me an opportunity to work in their lab and their invaluable time for helpful discussions. I feel deep sense of gratitude towards Prof. Jacques Prost whom I look up to for his unquestionable authority in the field of Biophysics, accompanied with a truly down to earth and friendly attitude, especially towards amateurs like me.

During my PhD years, Prof. Madan Rao and Prof. V. A. Raghunathan assessed my progress every year, not only as a part of the annual review process, but with a genuine concern about my work and a wish to see me improve my capabilities. I sincerely thank them. I would also like to thank Dr. Aurnab Ghose (IISER, Pune) and Dr. Sandhya Kaushika (DBS, TIFR Mumbai) and the respective lab members for making their lab resources available for my work. Thanks are also due to Prof. T. N. Seshadri (University of Delhi) for helpful discussions and constant encouragement.

I am immensely grateful to the technical staff of RRI, especially Mr. Ishaq, Mr. Dhason, Mr. Ram and Mr. Venu, Mr. Achan and Mr. Paul from the mechanical workshop for helping my experiments run smooth. I would also like to thank RRI Administration department for taking care of most of the formal/official procedures from time to time.

I am lucky to get a wonderful bunch of lab-mates who became my local family in RRI. PhD life would have been much harder without them being around. Thus, I thank Renu, Roli, Venu, Som, Sushil, Shubham, Chandrasekhar, Sampada, Alka and Susav for being there. The work-culture in the Biophysics lab remained healthy and cheerful, owing to them. I am thankful to my hostel mates namely Nipanjana, Abhijit and Raj Hossein who were helpful to me. I thank S. Radhika and Seunghyun for the fun moments we enjoyed together. It was a great pleasure to be in the company of Habiba and my littlest and cutest friend Isa.

I take this opportunity also to thank my good old friends Asmita Redij, Kshitij Thorat, Madhura Marathe and Santidan Biswas for all the fantastic times we have shared and hopefully will keep sharing, no matter the distance between.

It always fills me with gratitude and happiness to have found Madhura, Giri and Pragya as my life-long friends. I thank them for being always there for me.

During my PhD years it was due to Mrs. Ratna Sharma - my music teacher and her warm affectionate presence that I could temporarily forget the work related worries and indulge in something I love to do besides academics. I am immensely grateful to her.

Words fall short to express my feeling of gratitude towards my parents in law who have been a constant source of encouragement and support. Finally, it feels great to get a chance to say something about my parents, my brother Amogh, my grandparents and Shreyas! They have been strongly supportive and incredibly patient as always. To put it simply, they have been just wonderful. It is not possible to thank them enough for their love and support. I can only hope to make them proud.

Anagha Sanjay Datar

Bangalore

July, 2014

SYNOPSIS

The brain and rest of the nervous system are pivotal for control of the body and communication among its various parts. A neuronal cell which is the basic unit of this system, has a very specialized form and function. Axons of neuronal cells, with a characteristic long and thin tube-like shape, play an important role in transmitting electrochemical signals and carrying out intra-cellular trafficking of synaptic vesicles and cytoskeletal polymers. In this thesis work we have tried to explore and understand the shape dynamics of axons of neuronal cells, subjected to different conditions. The stability of the tube-like shape of axons which are typically hundreds of μm long and $\sim 1\mu m$ in diameter, is important for the sound functioning of neurons. It is found in neuro-degenerative conditions for example, brain stroke, Alzheimer's disease and stretch injuries that the axonal shape is distorted resulting in radius modulations or retraction of the axons. The mechanisms of these phenomena are not very well studied. Our experiments attempt to mimic similar shape changes using biochemical and mechanical perturbations and observe the live dynamics in order to understand the underlying mechanism. The structural details of the thesis are as follows:

Chapter I. Introduction

This chapter describes the structural details of the system under the experimental study, which is axons of neuronal cells from chicken embryonic dorsal root ganglia (part of the peripheral nervous system). Axons are long membrane-bounded extensions with approximately cylindrical organization of the cytoskeletal filaments. The long microtubules (MTs) are arranged in a co-axial manner surrounded by network of neuro-filaments (NFs) and a cortical layer of f-actin underlying the axonal membrane. In some of the neuro-degenerative conditions mentioned in the beginning, it is seen that the microtubules or their associated proteins get modified or reorganized, which could be one of the possible reasons behind the degeneration of the axon.

Such a geometry of axons can be mimicked in the laboratory by disrupting the microtubule structure in axons using a drug called Nocodazole (Noco). Although

this phenomenon is known for several decades, the physical mechanism and the dynamics of the beading process remain poorly studied. The chapter describes the prevailing hypothesis of traffic jams of intra-axonal transport being the reason behind Noco beading. Another known mechanism of inducing the radius-modulated shape is by subjecting axons to conditions which give rise to increase in axonal membrane tension. Hypo-osmotic shock induced pearling of axons is a well studied example of this case. We describe the basic details of this mechanism. The validity of each of these two hypotheses is tested in Chapter II in the context of Noco beading.

In the latter part of the chapter, we discuss the phenomenon of axonal retraction, which is commonly seen in removal of unwanted neuronal connections in developing organisms. Similar retraction can be induced *in vitro* by exposure to certain biochemical factors. Our experiments (presented in Chapter II) show that pharmacological disruption of f-actin in axons can effect in a similar type of retraction.

Thus, this chapter gives the necessary background for our experimental work and builds an insight into the system and the problem addressed in the rest of the thesis.

Chapter II: Shape transformations of Axons induced by Pharmacological Disruption of the Cytoskeleton

This chapter describes the experimental results of investigation on the process of Noco induced beading and Latrunculin-A (a drug that disrupts dynamic f-actin) induced retraction of axons. We begin with the quantitative characterization of the Noco induced beading which involves measuring the relevant length and time scales of beading.

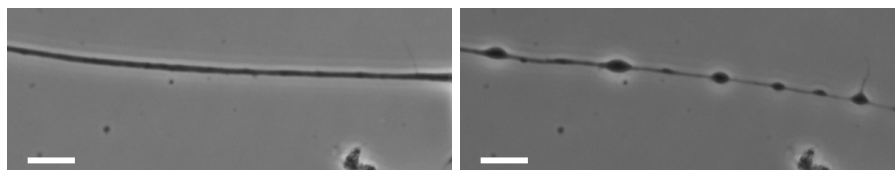


FIGURE 1: A chicken embryo DRG axon before (left) and after (right) Noco treatment. The latter morphology is called as axonal beading or swellings. Bar: $10\mu m$

Next, we consider the possible mechanisms for Noco-beading and test their validity as follows:

- **Pearling instability induced by rise in the membrane tension:** It is known that when axons are exposed to a sudden dilution of the surrounding medium, they undergo an osmotic shock which gives rise to Rayleigh-Plateau like instability which is a reversible shape change depending upon the magnitude of the shock. A similar change in the osmolarity across the axonal membrane may occur after Noco treatment, where the MT polymers are replaced by tubulin monomers, increasing the particle number (and osmolarity) inside the axon by a huge amount. Thus, the action of Noco may effect to an application of osmotic shock, causing the observed beading. We tested this hypothesis, by comparing features of pearling instability due to hypos-osmotic shock with those of Noco beading. For instance, in the case of osmotic pearling, there exists a linear dependence between initial radius of the axon R_0 and periodicity of pearling λ ; while we show that firstly, Noco beading is not periodic and the average distance between beads for a given axon d has no correlation with R_0 . Further, the trademark observations of osmotic pearling *viz.*, rapidly rising volume and curved surface area of axons before the onset of the shape instability were not seen in the case of Noco beading. On the basis of measurements described in Chapter IV, we also show that the small rise in the axonal membrane tension after Noco treatment is insignificant in comparison with the critical tension value σ_c required to be exceeded for the onset of pearling instability. Thus, we conclude that the mechanism of Noco-beading must be different from the pearling instability induced by rise in the membrane tension.
- **Traffic jams in intra-axonal transport:** Another mechanism leading to the observed beading can be due to traffic jams resulting from loss of the microtubule tracks at multiple positions along an axon, leading to accumulation (or traffic jams) of the organelles and synaptic vesicles. This is hypothesized to result in the subsequent beading. Our observations show that the axonal transport continues to take place even after bead formation and the beads

themselves can move along the axon, sometimes resulting into bead-merging events. Further, we also tried inducing local traffic jams by exposing only a small length of an axon to Noco. In order to do this we developed a set-up which employed a micro-injection device with two micro-pipettes for infusion and suction of the drug. It was seen that this did not result in the beading of the exposed part of axon. To conclude, the traffic jam hypothesis is inconsistent with the observations regarding Noco-beading.

Measurements described in Chapter 4 show that the axons maintain a small but finite membrane tension, even after cytoskeleton depolymerization. This leads us to hypothesize a mechanism for Noco-beading arising *not* from a rise in the membrane tension but from a significant reduction in the bulk compression modulus value of axons after Noco treatment, so that the critical membrane tension required for the cylindrical shape to become unstable, becomes comparable to the small rest membrane tension value itself. Further, the fluorescence labelling of the cytoskeletal elements shows that not only tubulin (probably in the subunit form as a result of the action of Noco) but also neurofilaments get strongly accumulated in the beaded regions of axons, leaving the segment between the beads almost devoid of them. This leads us to hypothesize another mechanism for Noco beading, where the axonal cytoskeleton is under a pre-stress and addition of Noco releases this pre-stress, resulting in the observed local accumulations of tubulin and neurofilaments along an axon. Such a pre-stress could arise from the active contractility of acto-myosin assembly. But our experiments show that inhibition of this contractility does not inhibit Noco-beading. Therefore the origin of such a pre-stress is unknown.

The last part of this chapter describes our observations of axonal retraction induced by exposure to Latrunculin-A or Lat-A which is an f-actin disrupting drug. We describe the process of retraction, plot the evolution in time and present fluorescence imaging of partially retracted axons labelled for cytoskeletal proteins. Even in this case, it can be seen that axonal neurofilaments and tubulin undergo remarkable reorganization after an f-actin targeted drug treatment, strengthening our hypothesis of an existence of a pre-stress in the axonal cytoskeleton which gets released when any one of the cytoskeletal filament structures is disrupted. To test

this hypothesis further, we performed laser mediated, very local disruption of the cytoskeleton and study its effect on the axonal shape as described ahead.

Chapter III: Shape dynamics in Laser-Transected Axons

In this project we studied the effects of a local disruption of the axonal integrity by ablating axons at the midpoint along their length using a focussed high power laser. In response, axons show interesting shape deformations such as snapping and buckling like a stretched rubber band (fig. 2), along with beading (fig. 3) and long length retraction.

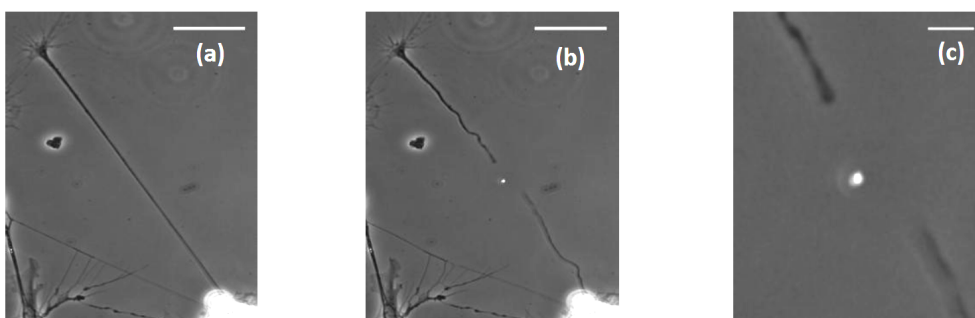


FIGURE 2: Snapping and buckling after laser ablation. An axon (a) before and (b) after a laser cut. Bar: for (a) and (b) $40\mu m$, for (c) $8\mu m$

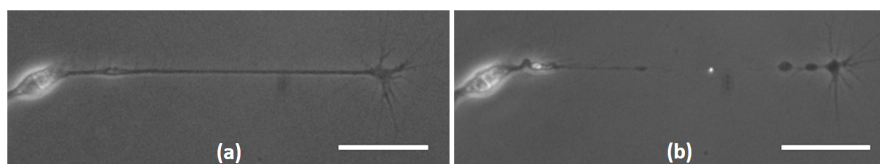


FIGURE 3: Axonal beading after laser ablation. An axon before (left) and 15 seconds after (right) a laser cut. Bar: $40\mu m$

These shape transformations after laser cut are also observed in the depleted ATP condition. This implies that here, the mechanism of the shape change is passive. In addition we see similar responses of the cytoskeleton alone after a partial ablation of axon where the membrane tube remains intact but the cytoskeleton is locally disrupted. This observation supports our hypothesis that the axonal cytoskeleton is under stress and undergoes relaxation by either retracting or beading within the membrane tube, when there is a disruption or discontinuity in its organization. We verify that the observations are independent of the method of cutting the axon by performing mechanical transection of axons.

Chapter IV: Membrane dynamics in axons probed using tether pulling technique

Here we present our experiments on membrane tension measurements and membrane dynamics of axons, probed using the technique of pulling membrane tubes or tethers from axonal membrane. The relevant force measurements were done using a set up of optical tweezers and a calibrated quadrant photo diode based system. We measured the static tether force and compared the membrane tension values for control or untreated axons, and axons treated with Noco or Lat-A (fig. 4). It shows that axons maintain a rest membrane tension (a function of the tether force) at almost the same order of magnitude even after cytoskeletal disruption.

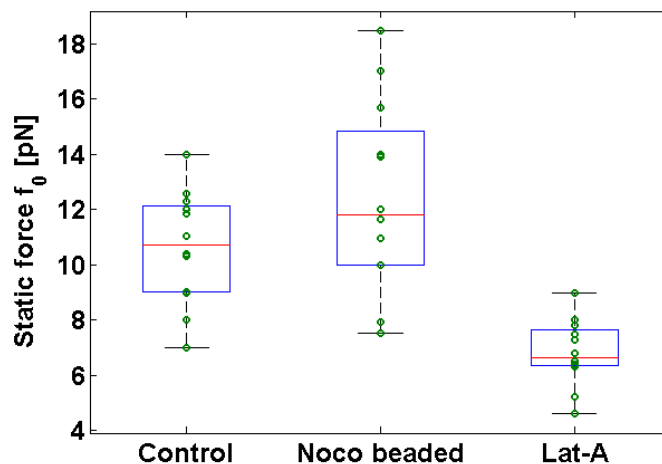


FIGURE 4: Distribution of static tether force f_0 for control, nocodazole beaded and lat-A treated axon populations (sample size : 12 each). Each green open circle corresponds to f_0 measured on a different axon. On each box, the central mark (red line) is the median, the edges of the box are the 25th and 75th percentiles and the whiskers extend to the most extreme data points.

We also observed interesting dynamic response of the tether force when a pre-formed axonal tether is step-elongated or step displaced along the surface of the axon. A theoretical model is presented and compared with the experimental findings of the tether force relaxation behaviour after application of step-elongation. The lateral displacement of the tether results in sliding of the tether-base along the axonal surface. This is an interesting observation owing to the fact that such a behaviour is not seen in many other types of cells. Additionally, we reported occurrence of spontaneous peaks in the tether force in absence of any external perturbation. We show that these peaks with a slow rise and a very fast rupture,

are strongly f-actin dependent and very similar to the forces exerted by filopodia of HeLa cells. Our findings point towards an unusual cytoskeletal organization in axons, where connections between the membrane and the cortical cytoskeleton appear to be more sparse and weaker in comparison with other cell types but the actin cortex can affect the apparent membrane tension and transiently influences the dynamics of membrane tethers.

Thus, this thesis probes into the dynamics of the processes related to axonal shape stability and transformations. Our observations indicate important role played by presence of pre-stress in the axonal cytoskeleton and the rest membrane tension. The multiple methods of inducing beading and retraction explored in this thesis, might be different morphological manifestation of the same driving mechanism. Such studies are of vital importance as understanding mechanisms underlying the involved processes can provide clues to better understanding of axonal degeneration leading to atrophies.

Prof. Pramod Pullarkat
Raman Research Institute

Anagha Sanjay Datar

Publications

- A. Datar, T. Bornschlögl, P. Bassereau, J. Prost, and P. A. Pullarkat
‘Dynamics of Membrane Tethers Reveal Novel Aspects of Cytoskeleton-Membrane Interactions in Axons’
Accepted in the **Biophysical Journal**

Contents

1	Introduction	1
1.1	Structure of a neuronal cell	3
1.1.1	Cytoskeleton of a neuronal cell	4
1.1.2	Axonal Transport	6
1.2	Microtubule disruption and axonal shape deformations	6
1.3	Axonal pearling due to rise in membrane tension	8
2	Shape transformations of Axons induced by Pharmacological Disruption of the Cytoskeleton	17
2.1	Methods	19
2.1.1	Measurement of volume and curved surface area of axons	20
2.1.2	Keeping an axon in focus using z-stack imaging	21
2.1.3	Local application of a drug	21
2.1.4	Fluorescence labelling	23
2.1.4.1	Tubulin	24
2.1.4.2	Neurofilaments	24
2.1.4.3	f-actin	25
2.1.4.4	Labelling with Calcein	25
2.1.5	Imaging	26
2.2	Results and Discussion	26
2.2.1	Characterization of noco beading	26
2.2.1.1	Percentage of beading with respect to concentration of Noco and exposure time	27
2.2.1.2	Spatial Distribution of beads	29
2.2.1.3	Effect of ATP depletion on Noco-beading	30
2.2.2	Verifying the known mechanisms of axonal beading	32
2.2.2.1	Pearling instability due to Hypo-osmotic shock	32
2.2.2.2	Membrane Tension measurements	39
2.2.2.3	Verifying the hypothesis of Local disruption of Microtubules and consequent Traffic jam	40
2.2.3	Local application of Nocodazole	43
2.2.4	Verifying the role of Acto-Myosin contractility	46

2.2.5	Fluorescence Imaging of Cytoskeleton	47
2.2.5.1	Control or untreated axons	48
2.2.5.2	Noco-beaded axons	50
2.3	Summary and conclusions	51
2.4	Axonal retraction induced by Latrunculin-A	55
2.4.1	Experiments and Results	56
2.4.2	Remarks	59
3	Shape dynamics in Laser-Transected Axons	65
3.1	Motivation	65
3.2	Previous work on axon transections	67
3.3	Laser-Tissue Interaction	68
3.4	Experimental Set-up	71
3.5	Materials and Methods	73
3.6	Results	74
3.6.1	Fast Retraction or <i>Snapping</i>	74
3.6.2	Effect of cytoskeleton perturbations on snapping	77
3.6.3	Buckling after laser cut	79
3.6.4	Beading after laser cut	79
3.6.5	Slow retraction after snapping:	81
3.6.6	Mechanical transection	86
3.7	Summary and Discussion	88
4	Membrane dynamics in axons probed using tether pulling technique	97
4.1	Theory of Membrane Nanotubes	98
4.1.1	Static behaviour	98
4.1.2	Dynamic behaviour	101
4.2	Previously established experimental findings	102
4.3	Experimental Methods of tether pulling	105
4.3.1	Micropipette aspiration method	106
4.3.2	Optical trap method	106
4.3.2.1	Optical Trap	107
4.3.2.2	Tether pulling using optically trapped beads	108
4.4	Results and Discussion	113
4.4.1	Static tether force measurements	113
4.4.2	Dynamic response to Step-displacements	115
4.4.3	Spontaneous dynamics	128
4.5	Conclusion	132
5	Summary and Outlook	139
	Appendices	147
A.1	Primary DRG neurons	149
A.2	Culture media	149

A.3 Drugs and other treatments buffers 150

Chapter 1

Introduction

The brain and rest of the nervous system are pivotal to the control of the body of an organism and communication among its various parts. A neuronal cell which has a very specialized form and function, is the basic unit of the nervous system. Neurons form networks which process and transmit information in the form of electrochemical signals to and from different parts of a body. These signals are the means of sensing, analysing and generating responses in an organism. Neurons extend long and thin processes called as Axons which reach out to other neurons or muscle or gland cells and form connections. In mammals like blue whales, axons can be about ten meter long with an almost uniform diameter of about a micrometer. The maintenance of shape and stability of such thin and long structures is important because its impairment can cause many neurological disorders which affect both the peripheral and central nervous system. In many neuro-degenerative conditions, such as brain injuries of different kinds [1], early stages of Alzheimer's disease [2], [3], [4], ischemia or brain stroke [5] etc., the axonal caliber gets modulated with multiple swellings or beading. In order to prevent such shape deformations of axons, it is important to understand not only the biochemical changes happening within the system, but also the physical mechanisms underlying the shape stability and dynamics of shape change in each of these cases. One way of investigating the mechanisms of this shape change is to closely inspect such a shape change by mimicking it in the laboratory by applying controlled perturbations of different kinds to axons, like those shown in fig. 1.1.

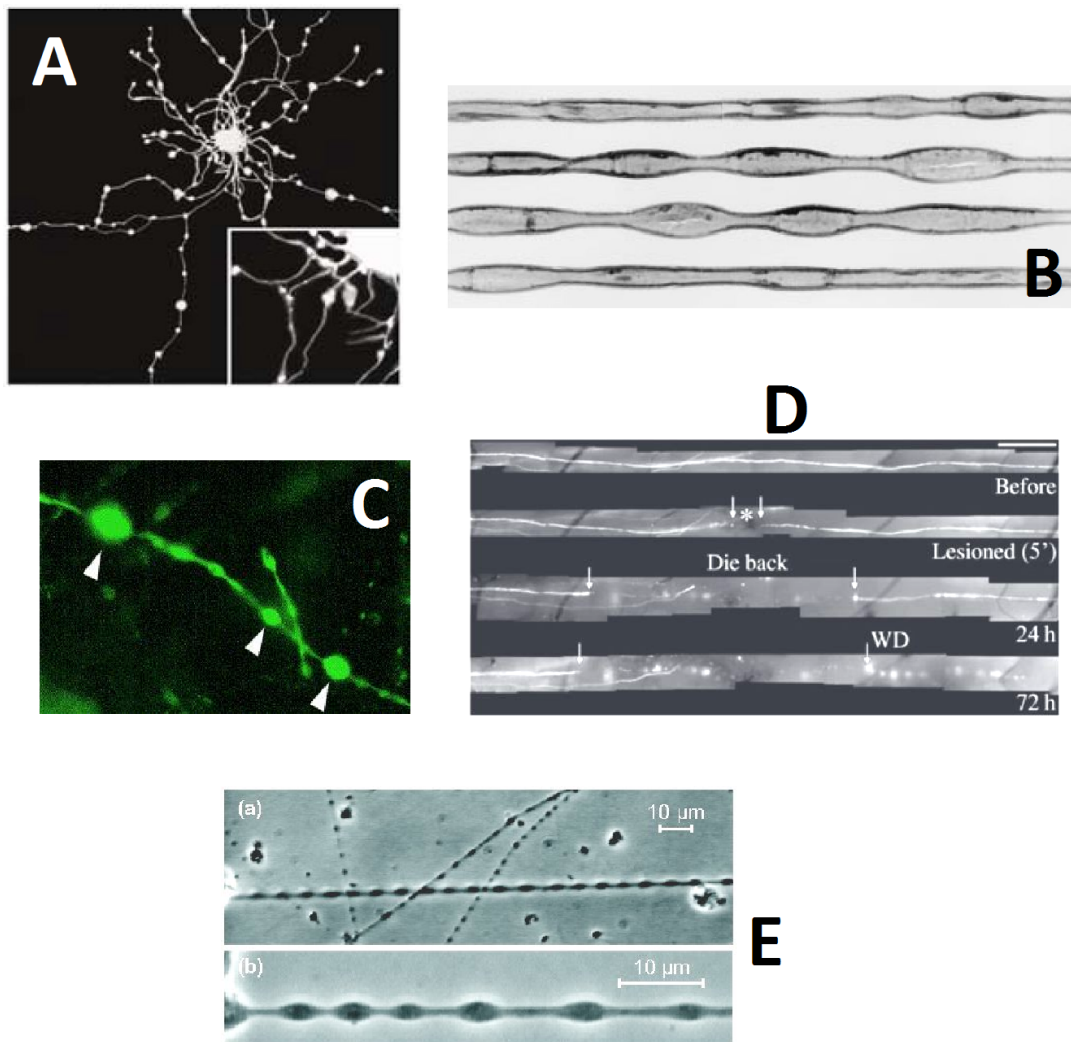


FIGURE 1.1: Axonal beading in different neuro-degenerative conditions. (A) Axons expressing (UbB)+1, a protein found in Alzheimers disease [4] (B) Axons in a stretched nerve [6] (C) Axons subjected to oxidative stress [7] (D) A mechanically transected axon in a live mouse spinal chord undergoing retraction and beading [8] (E) Axons subjected to hypo-osmotic shock [9].

This thesis investigates the process of axonal beading in great detail, with a particular emphasis on the dynamics of shape change. It is known that the shape of a biological cell is a function of the dynamics of cell membrane, cytoskeleton and their interplay. In order to understand the shape and stability of axons, it is important to be first familiar with the organization of neuronal cells and have a detailed view of the cytoskeletal structure of axons.

1.1 Structure of a neuronal cell

Neurons have a peculiar form as depicted in fig. 1.2. The cell body or the ‘soma’ contains the nucleus and extends short processes called as dendrites and typically one or two long processes called as axons.

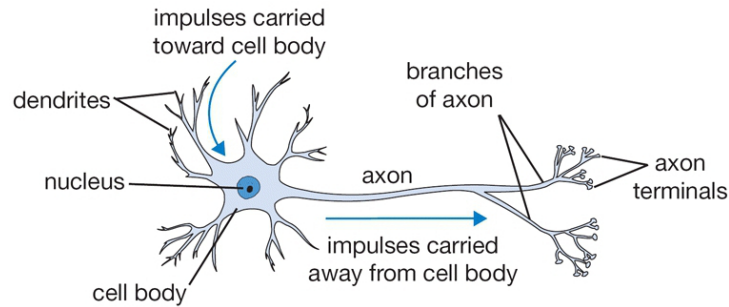


FIGURE 1.2: A typical neuronal cell comprises of the cell body or Soma where the nucleus is located, short processes called as dendrites and a long process called as an axon. The processes form contacts with other neuronal cells and transmit information in the form of electrochemical signals or impulses.

Dendrites and axons form special connections called as synapses with other neuronal cells. Dendrites receive electrochemical signals from other connected cells and transmit them towards the cell body whereas axons carry the signals away from the cell body to other connected cells. Typically, axons are much longer and with a more uniform diameter in comparison with dendrites. The squid giant axon, which is specialized to conduct signals very rapidly, is close to 1 mm in diameter. In the work presented in this thesis, we have used primary neuronal cells from chicken embryonic dorsal root ganglia. These cells were cultured according to the protocol given in [10] and described in detail in appendix A. After about 14 to 16 hours of growth, most of the individual axons in culture are seen to be several hundreds of μm long whereas the diameter is typically about 0.5 to 1 μm . Thus, axons have a fragile, long and thin membrane tube-like structure, which is stabilized by the cytoskeleton. Before forming a contact with the destination cell, an axon has a different structure at its distal end. This is called as a Growth Cone (GC) as shown in fig. 1.3 (b). This wide, fan-shaped structure with finger like protrusions does the job of steering and deciding the direction of growth of the axon, based on the extra-cellular cues. The internal structural details of a neuronal cell are explained in the following.

1.1.1 Cytoskeleton of a neuronal cell

Like most of the other eukaryotic cells, axonal cytoskeleton comprises of three main types of polymeric filaments, namely, microtubules (MTs), neuro-filaments (NFs) which are class IV intermediate filaments found in neurons [11] and f-actin. A rich variety of molecular motors and other associated proteins play an important role in the organization and dynamics of these filamentous structures. Fig. 1.3 (a)-(d) show the organization of these filaments within a neuronal cell.

There is a vast amount of literature available on the structural and dynamic properties of MTs and f-actin, both in vivo and in vitro. However, the NFs are not so well understood. In the following, we shall consider the properties of these three types of filaments in the context of axons.

Axons mostly comprise of co-axially arranged MTs which are surrounded by the NF matrix as shown in fig. 1.3 (b). F-actin is found in the cortical layer just adjacent to the plasma membrane of the axon [12] and it is also prominently concentrated in the growth cone (GC) structure. Actin filaments located in the GC are highly dynamic in comparison with those located along rest of the axon [13]. Axonal MTs are oriented in a polarized manner with their + ends directed towards the GC [14]. Microtubule associated proteins (MAPs) like Tau play a significant role in modulating stability of MTs in axons. It is shown that the most distal region of an axon i.e. the region just next to the GC, mainly contains labile MTs while the main shaft contains both labile and stable MTs [15]. Axonal MTs are in close proximity with the NFs [12]. Interactions between the NF side-arms are known to be responsible for deciding the axonal caliber. However, the exact nature of these interaction is not yet completely clear.

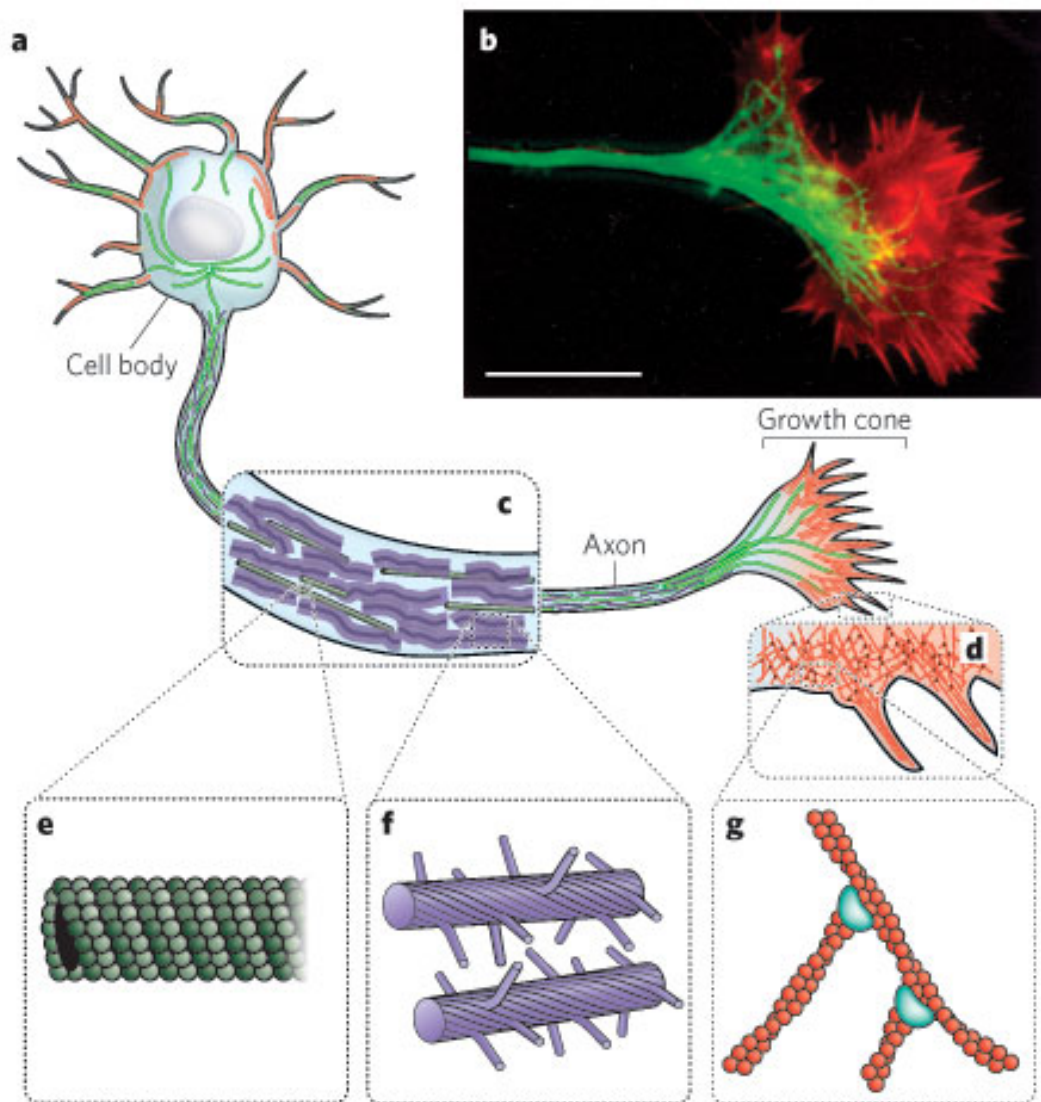


FIGURE 1.3: Organization of neuronal cytoskeleton. (a),(b) Neurons have a cytoskeleton that consists of three main polymers: microtubules or MTs (green), neuro-filaments or NFs (purple-blue) and actin filaments or f-actin (red). MTs emanate from the axon, and f-actin networks form sheet-like structures and filopodial protrusions at the leading edge. Scale bar, $20 \mu m$. (c) The axon is a long membrane-bounded extension, in which NFs (a class of intermediate filament in neurons) form a structural matrix that embeds MTs, which transport materials from the cell body to the axon terminals at the synapse. (d) The growth cone contains f-actin networks and parallel f-actin bundles in the filopodia. (E) Microtubules consist of 13 protofilaments of tubulin dimers arranged in a hollow tube. (f) NFs have flexible polymer arms that repel neighboring NFs and determine the radius of the axon. (g) Actin filaments are arranged into networks. These networks can have many architectures, including the branched structures depicted here, which are formed by the Arp2/3 complex (blue). The diameters of MTs, NFs, and f-actin are within a factor of three of each other; the diagrams in (e), (f) and (g) are drawn approximately to scale. However, the relative flexibilities of these polymers differ markedly, as indicated by their persistence lengths: from least to most flexible, MTs ($5,000 \mu m$), f-actin ($13.5 \mu m$) and NFs ($0.5 \mu m$). Image and caption credits: <http://www.nature.com/scitable/topicpage/microtubules-and-filaments-14052932> and [16]

1.1.2 Axonal Transport

Axonal MTs act as railroads for transport of many neuro-transmitters, organelles and cytoskeletal elements which are carried as cargoes by the + ended Kinesin motors and - ended Dynein motors walking on the MTs. A detailed review of this process can be found in [17] and [18]. The transport away from the cell body is called Anterograde and that towards the cell body is called Retrograde transport. Axonal transport can be classified in two well separated regimes of speeds which are fast transport at $\sim 100\text{ mm}$ per day and slow transport at $\sim 1\text{ mm}$ per day. The typical cargoes being fast transported are neurotransmitters, membrane proteins and lipids, mitochondria and lysosomal vesicles whereas the slow transported cargoes are mostly short cytoskeletal filaments. Both these regimes are important in providing the necessary structural and functional materials to discrete functional compartments along the length of an axon.

1.2 Microtubule disruption and axonal shape deformations

In the beginning of this chapter we saw that in many neuro-degenerative conditions, the axonal shape gets deformed from a uniform-radius tube to a geometry with multiple swellings separated by constricted segments. We call this morphology as ‘axonal beading’ and axons with such a morphology as beaded axons. In some of the neuro-degenerative conditions, it is seen that microtubules (MTs) and/or their associated proteins get modified or reorganized, which could be one of the possible reasons behind the degeneration and shape deformation of axons [2], [19]. In order to investigate the involved dynamics and underlying mechanism of the shape change process, one can mimic the situation by pharmacological disruption of axonal MTs. Nocodazole (Noco) is a MT-specific drug which is known to readily inhibit MT polymerization and disrupt the preformed MTs at longer exposure times [20]. It is also known for many years that action of Noco on neurites causes formation of multiple swellings (beading) or leads to neurite retraction [21] [22]. From the ultra-structural imaging of PC12 neurites (structures very similar

to axons in morphology) it was shown that the swellings formed after the action of Noco, comprised of membranous organelles (fig. 1.4)

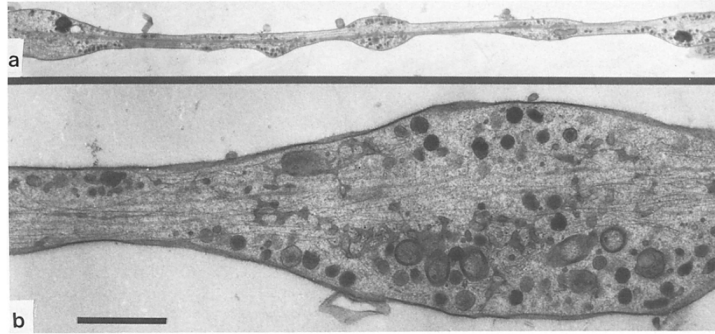


FIGURE 1.4: Electron micrographic serial reconstruction of Nocodazole sensitive neurites. Both the neurites were treated with $5 \mu\text{g/ml}$ Noco for one hour. Bar: (a) $2 \mu\text{m}$ (b) $0.2 \mu\text{m}$. Image courtesy: [21]

On the basis of the observed accumulation of organelles in the beaded regions, it was concluded by the authors that the accumulation of organelles itself is the reason behind neurite beading. This is very similar to the scenario of Traffic jams in axonal transport, prevailing in the early stages of Alzheimers' disease as proposed by the Goldstein lab [2]. The hypothesis of traffic jams leading to axonal beading after MT disruption by Noco or other drugs has been suggested by many research groups. In a study which compared axonal beading caused by mechanical injury with that caused by a treatment with another MT disrupting drug, Vinblastine, it was claimed that the MT disruption results in axonal transport impairment, leading to organelle accumulation and beading. It is worth noting that in all these studies, the axonal shape dynamics as a function of axonal transport was not studied. The ultra-structural imaging of beaded regions as that shown in fig. 1.4 was done in fixed axons *after* the beading had already formed and matured. Therefore, the question that whether the observed organelle accumulation is the cause of axonal beading or whether it is an effect of the overall volume reorganization along the length of an axon undergoing beading, still remains unanswered.

As will be discussed in the next chapter, in our investigation on Noco induced beading we try to address this question by doing live imaging of transport in axons undergoing the beading process.

1.3 Axonal pearling due to rise in membrane tension

Another scenario where axonal beading is observed, is based on a completely different mechanism which deals with physical properties of the system, like membrane tension and bulk elasticity. This is the case of axonal 'pearling' in response to a sudden rise in the membrane tension due to nerve stretching [6] or due to application of hypo-osmotic shock [9]. The mechanism is similar to the Rayleigh-Plateau instability of liquid jets where liquid columns (or cylinders) are *unstable to* pearled geometry owing to the finite surface tension at the liquid-air interface. In brief, a cylindrical jet of fluid with a finite surface tension can reduce its surface energy by going to a shape with a smaller surface area than the cylinder. If the radius of the original cylinder is R_0 then a sinusoidal perturbation with a wavelength $\lambda > 2\pi R_0$ has a smaller surface area (and surface energy) than the cylinder, thus making the jet unstable to such perturbations. The mode with the fastest growth rate shows up and the jet may break into droplets [23] as shown in fig. 1.5.

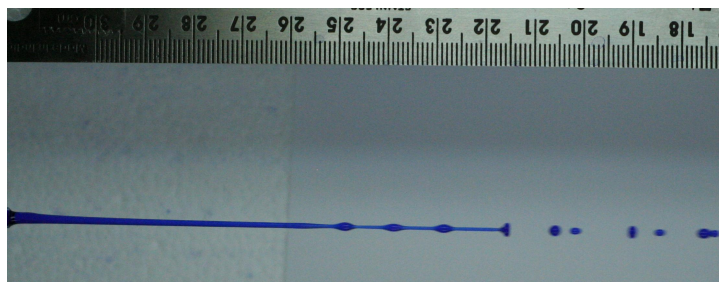


FIGURE 1.5: A liquid column becoming unstable to sinusoidal mode and breaking into droplets due to Rayleigh-Plateau instability. The scale in the upper part of the image shows readings in cm. Image was captured by Rohit Sharma using colored liquid falling down a glass pipette, in Biophysics lab, Raman Research Institute, Bangalore, India.

Axons, which can be approximated to have a cylindrical shape, also have a finite membrane tension but the case of axons differs from liquid jets due to a non-zero bending modulus of the plasma membrane and the bulk elasticity of the cytoskeleton gel which cost energy in order to change the shape. Thus, there is a threshold membrane tension value (σ_c), mostly contributed by the cytoskeleton elasticity, below which the cylindrical shape of the axon is stable [9]. However, in the conditions where the membrane tension exceeds this critical value, the axon may undergo pearling. Work by Pullarkat et al. showed a way of inducing a

reversible pearling instability of axons by application of hypo-osmotic shock and discussed the underlying physical mechanism in detail. Such a shock causes the axons to take in water from the surrounding medium in order to balance the osmolarity difference across the membrane. This results in swelling of the axon which results in stretching of the axonal membrane, thus causing a rapid rise in membrane tension. If the shock is strong enough, the axonal membrane tension exceeds σ_c and triggers the pearling instability as shown in fig. 1.6.

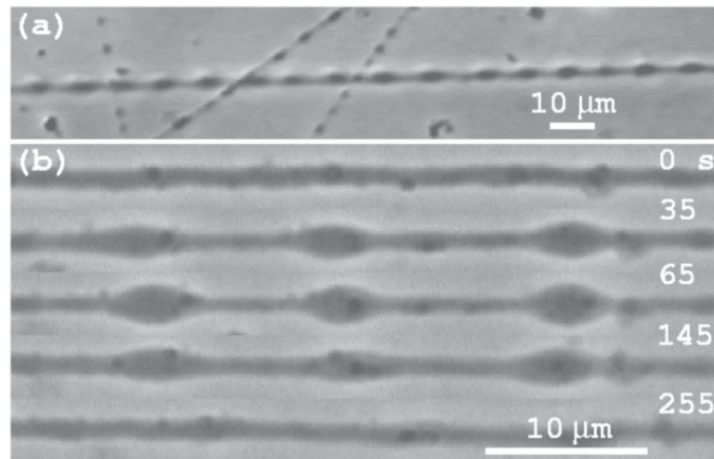


FIGURE 1.6: Osmotically induced shape instability in chicken embryo neurons. (b) Image sequence showing the growth and relaxation of the instability in a PC12 neurite. Image courtesy: [9]

Fig. 1.6 shows that the instability is reversible and the axon gains back its original cylindrical geometry. The authors hypothesize that the shape relaxation occurs due to axon's ability to regulate the volume by opening the membrane-bound ion channels. During the onset and the relaxation of the instability, the volume and the curved surface area of axon show a systematic evolution as shown in fig. 1.7. The Y-axis shows normalized values of the volume \bar{V} and area \bar{A} , with respect to their initial values before application of osmotic shock. The ratio $\sqrt{\bar{V}/\bar{A}}$ (dotted line) reflects any deviations from the cylindrical geometry. It can be seen that the instability sets in when the area rises by about 6%.

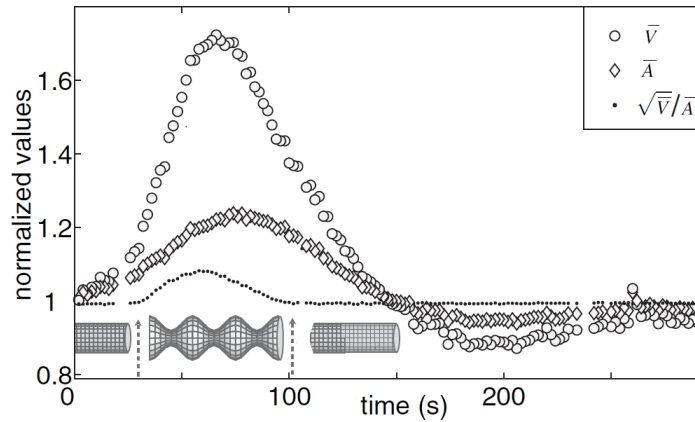


FIGURE 1.7: Evolution of the normalized volume \bar{V} and area \bar{A} of a neurite with $R_0 = 0.5 \mu\text{m}$ at $33 \pm 1^\circ\text{C}$. The ratio $\sqrt{\bar{V}}/\bar{A}$ (dotted line) reflects any deviations from the cylindrical geometry. Image courtesy: [9]

The mechanism of hypo-osmotic shock leading to axonal pearling may turn out to be relevant in the case of Nocodazole induced beading of axons for the following reason. The MT disrupting action of Noco may result effectively in converting the polymeric or filamentous mass into a much larger number of Tubulin subunits. This could be equivalent to increasing the particle number density inside the axon by a large amount with respect to that outside the axon, which is same as applying a hypo-osmotic shock. Therefore the osmotic shock induced pearling might provide a candidate for the mechanism underlying Noco induced beading of axons.

Thus, with the background of axon's internal structure and the previously proposed mechanisms of axonal beading, we can proceed to Chapter 2, which discusses the experiments and results of our work on the phenomenon of Nocodazole induced beading of axons. There, we also present some preliminary results on effect of f-actin disruption using a drug called Latrunculin-A. Collectively, these findings accentuate the role of cytoskeleton integrity in maintenance of shape and stability of axons.

In Chapter 3 we present effects of a very local disruption of cytoskeleton using the method of laser ablation on the shape dynamics of axons. The necessary introduction to the technique and the background work are presented in the beginning of that chapter.

Chapter 4 presents our findings on the axonal membrane dynamics, probed using the method of membrane nanotube (tether) pulling with the help of optical tweezers. Again, the introduction to the technique and the background work are presented in the beginning of that chapter.

Chapter 5 gives a cumulative summary of the results and conclusions of this thesis work.

Note: All time lapse video recordings (movies) which are an integral part of this thesis-work and are referred to at various places, can be found at www.rrri.res.in/thesis_Anagha_movies with username: thesis and password: An@rri.th). The movies are organized chapter-wise.

Bibliography

- [1] P. Shannon, C. R. Smith, J. Deck, L.C. Ang, M. Ho, and L. Becker. Axonal injury and the neuropathology of shaken baby syndrome. *Acta Neuropathol*, 95:625–631, 1998.
- [2] Gorazd B. Stokin, Concepcin Lillo, Toms L. Falzone, Richard G. Brusch, Edward Rockenstein, Stephanie L. Mount, Rema Raman, Peter Davies, Eliezer Masliah, David S. Williams, and Lawrence S. B. Goldstein. Axonopathy and transport deficits early in the pathogenesis of alzheimer’s disease. *Science*, 307(5713):1282–1288, 2005. doi: 10.1126/science.1105681. URL <http://www.sciencemag.org/content/307/5713/1282.abstract>.
- [3] Tetsuya Ohgami, Tetsuyuki Kitamoto, and Jun Tateishi. Alzheimer’s amyloid precursor protein accumulates within axonal swellings in human brain lesions. *Neuroscience Letters*, 136:75–78, 1992.
- [4] Z Tan, X Sun, F-S Hou, H-W Oh, L G W Hilgenberg, E M Hol, F W van Leeuwen, M A Smith, D K O’Dowd, and S S Schreiber. Mutant ubiquitin found in alzheimer’s disease causes neuritic beading of mitochondria in association with neuronal degeneration. *Cell Death and Differentiation*, 14: 1721–1732, 2007.
- [5] Matthew D. Budde and Joseph A. Frank. Neurite beading is sufficient to decrease the apparent diffusion coefficient after ischemic stroke. *Proceedings of the National Academy of Sciences*, 107(32):14472–14477, 2010. doi: 10.1073/pnas.1004841107. URL <http://www.pnas.org/content/107/32/14472.abstract>.

- [6] Sydney Ochs, Rahmna Pourmand, Kenan Si, and Richard N. Friedman. Stretch of mammalian nerve in vitro: Effect on compound action potentials. *Journal of the Peripheral Nervous System*, 5:227–235, 2000.
- [7] Ben Roediger and Patricia J Armati. Oxidative stress induces axonal beading in cultured human brain tissue. *Neurobiology of Disease*, 13(3):222 – 229, 2003. ISSN 0969-9961. doi: [http://dx.doi.org/10.1016/S0969-9961\(03\)00038-X](http://dx.doi.org/10.1016/S0969-9961(03)00038-X). URL <http://www.sciencedirect.com/science/article/pii/S096999610300038X>.
- [8] Martin Kerschensteiner, Martin E Schwab, Jeff W Lichtman, and Thomas Misgeld. In vivo imaging of axonal degeneration and regeneration in the injured spinal cord. *Nature Medicine*, 11:572–577, April 2005.
- [9] Pramod A. Pullarkat, Paul Dommersnes, Pablo Fernández, Jean-Fran çois Joanny, and Albrecht Ott. Osmotically driven shape transformations in axons. *Phys. Rev. Lett.*, 96:048104, Feb 2006. doi: 10.1103/PhysRevLett.96.048104. URL <http://link.aps.org/doi/10.1103/PhysRevLett.96.048104>.
- [10] G. Banker and K. Goslin. *Culturing Nerve Cells*. A Bradford book. MIT Press, 1998. ISBN 9780262024389. URL <http://books.google.de/books?id=yVAYQBt1gEIC>.
- [11] D.L. Eng and L.F. Eng. Intermediate filaments. In Larry R. Squire, editor, *Encyclopedia of Neuroscience*, pages 173 – 178. Academic Press, Oxford, 2009. ISBN 978-0-08-045046-9. doi: <http://dx.doi.org/10.1016/B978-008045046-9.01010-X>. URL <http://www.sciencedirect.com/science/article/pii/B978008045046901010X>.
- [12] N Hirokawa. Cross-linker system between neurofilaments, microtubules and membranous organelles in frog axons revealed by the quick-freeze, deep-etching method. *The Journal of Cell Biology*, 94(1):129–142, 1982. doi: 10.1083/jcb.94.1.129. URL <http://jcb.rupress.org/content/94/1/129.abstract>.
- [13] PaulC. Letourneau. Actin in axons: Stable scaffolds and dynamic filaments. In Edward Koenig, editor, *Cell Biology of the Axon*, volume 48 of *Results and*

- Problems in Cell Differentiation*, pages 265–290. Springer Berlin Heidelberg, 2009. ISBN 978-3-642-03018-5. doi: 10.1007/400_2009_15. URL http://dx.doi.org/10.1007/400_2009_15.
- [14] Steven. R. Heidemann, James M. Landers, and Marlyn A. Hamburg. Polarity orientation of axonal microtubules. *Journal of Cell biology*, 91:661–665, December 1991.
- [15] FJ Ahmad, TP Pienkowski, and PW Baas. Regional differences in microtubule dynamics in the axon. *The Journal of Neuroscience*, 13(2):856–866, 1993. URL <http://www.jneurosci.org/content/13/2/856.abstract>.
- [16] Daniel A. Fletcher and R. Dyrche Mullins. Cell mechanics and the cytoskeleton. *Nature*, 463:485–492, January 2010.
- [17] Gerardo A. Morni, Matthew R. Burns, David L. Stenoiien, and Scott T. Brady. *Basic neurochemistry*, chapter Axonal transport, pages 485–502. Burlington, MA: Elsevier Academic, 8 edition, 2011.
- [18] Anthony Brown. Axonal transport. In DonaldW. Pfaff, editor, *Neuroscience in the 21st Century*, pages 255–308. Springer New York, 2013. ISBN 978-1-4614-1996-9. doi: 10.1007/978-1-4614-1997-6_14. URL http://dx.doi.org/10.1007/978-1-4614-1997-6_14.
- [19] Daphney C Jean and Peter W Baas. It cuts two ways: microtubule loss during alzheimer disease. *The EMBO Journal*, 32(22):2900–2902, 2013. doi: 10.1038/emboj.2013.219. URL <http://emboj.embopress.org/content/32/22/2900>.
- [20] F Samson, J A Donoso, I Heller-Bettinger, D Watson, and R H Himes. Nocodazole action on tubulin assembly, axonal ultrastructure and fast axoplasmic transport. *Journal of Pharmacology and Experimental Therapeutics*, 208(3):411–417, 1979. URL <http://jpet.aspetjournals.org/content/208/3/411.abstract>.
- [21] J R Jacobs and J K Stevens. Experimental modification of pc12 neurite shape with the microtubule-depolymerizing drug nocodazole: a serial electron

- microscopic study of neurite shape control. *The Journal of Cell Biology*, 103(3):907–915, 1986. doi: 10.1083/jcb.103.3.907. URL <http://jcb.rupress.org/content/103/3/907.abstract>.
- [22] Frank Solomon. Neuroblastoma cells recapitulate their detailed neurite morphologies after reversible microtubule disassembly. *Cell*, 21:333–338, September 1980.
- [23] Jens Eggers and Emmanuel Villermaux. Physics of liquid jets. *Reports on Progress in Physics*, 71(3):036601, 2008. URL <http://stacks.iop.org/0034-4885/71/i=3/a=036601>.

Chapter 2

Shape transformations of Axons induced by Pharmacological Disruption of the Cytoskeleton

In this chapter, we present investigation on the mechanism underlying the shape transformation of axons from a tube like structure with a uniform radius to a beaded geometry (fig. 2.1), caused by an exposure to a microtubule (MT) disrupting drug Nocodazole (Noco). We observe in most of the cases that after exposure to Noco, an axon initially undergoes local accumulation of its volume at multiple sites which develop into swellings or beads, while the segments of axon in between the beads undergo thinning. At a much later stage, almost all volume of the axon either gets accumulated in the beads, or is retracted back in to the soma. The cases of retraction exhibit movement of beads along the axon and sometimes merging of multiple beads. The presented work looks at various aspects of the process of Noco-beading, like the effect of different concentrations and exposure time of Noco on the beading process, the dynamics of shape parameters of axons, changes in the intra-axonal organization, the state of axonal transport, role of acto-myosin contractility etc.

Through our investigation we found a so far unreported way of triggering axonal retraction, which is caused by a long time exposure to an f-actin disrupting drug

Latrunculin-A (Lat-A). Interestingly, in the initial stages of this retraction, one can see bead formation similar to that seen after Noco treatment.

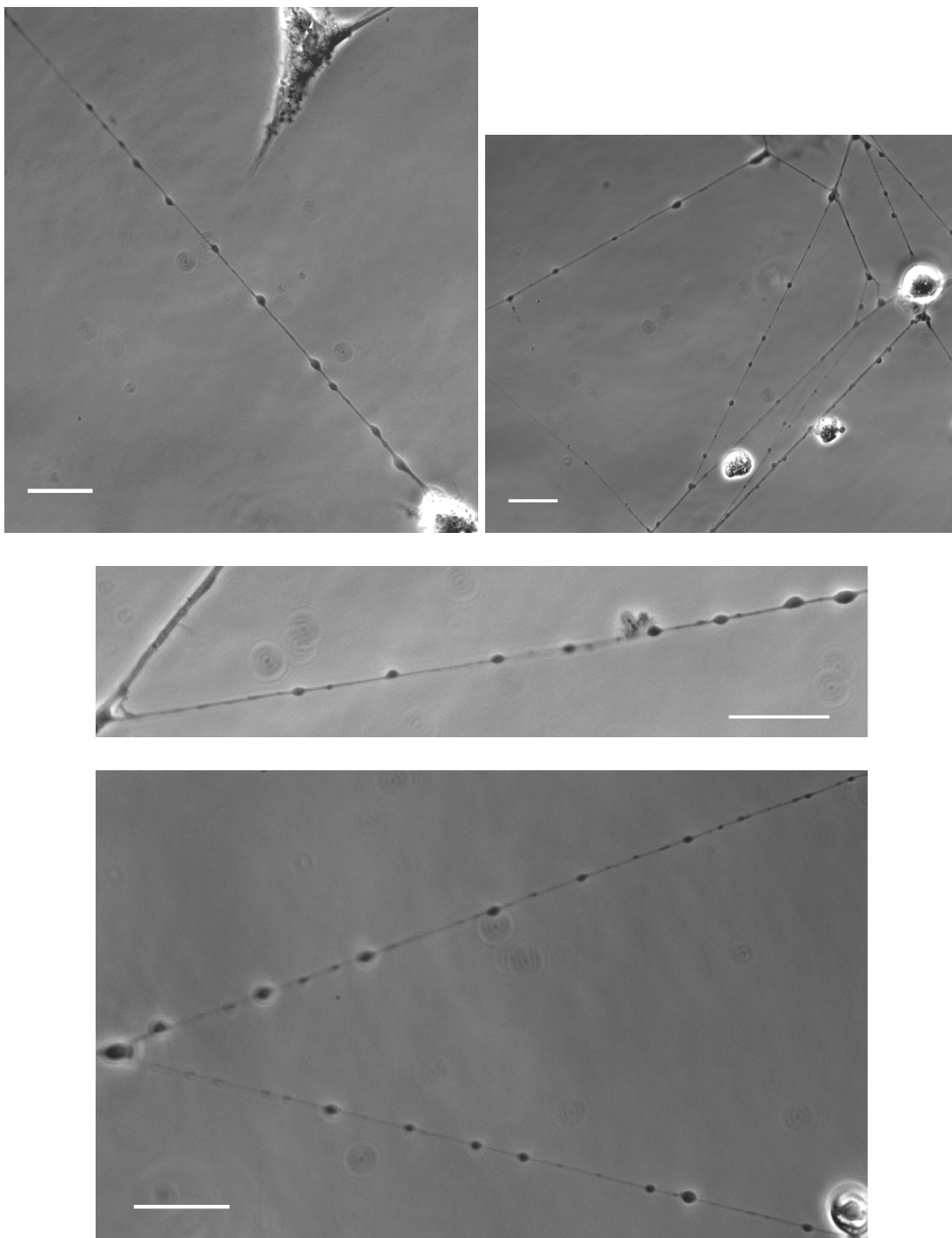


FIGURE 2.1: Phase contrast images of axons with beaded morphology due to Nocodazole treatment. All scale bars equal $20 \mu m$

This chapter describes our study on the shape transformations induced in a pharmacological way by the two drugs, Noco and Lat-A. It is organized as follows.

Firstly, the experimental methods used for the investigation are described; followed by the experiments and results section beginning with the characterization of Noco induced shape transformation of axons from a uniform tube-like to beaded geometry. Then systematic validation tests for the following mechanisms of axonal beading (previously proposed in different conditions as explained in detail the Introduction chapter) are presented.

- Shape instability due to rise in membrane tension
- Local disruption of microtubules (MTs) or impairment of MT based transport resulting in traffic jam

In the light of the second mechanism mentioned above, it was also tested whether beading can be induced by exposing only a small segment of a long axon to Noco. We set up a novel technique of using two micropipettes, one for infusion of the drug and other for the suction to generate a local flow profile in order to apply the drug at specific locations. Then, using specific drug treatments, we question the role of f-actin and myosin II in the process of Noco-beading. Next, using protein specific fluorescent labelling, we study the effect of Noco-beading on axonal cytoskeleton organization. These experiments help us in ruling out some of the earlier proposed mechanisms and narrow down on the possible mechanisms of beading. A few likely mechanisms are proposed which hypothesize that the beading is a result of relaxation of a pre-stress in the cytoskeleton or Noco-mediated disruption of MTs resulting in a significant reduction of the bulk compression modulus of the axonal cytoskeleton, making the axonal shape unstable. In the last part of the chapter we present our preliminary findings on axon retraction induced by Lat-A.

2.1 Methods

Throughout this thesis, the system under study is Dorsal Root Ganglia (DRG) neurons from chicken embryos. The protocol for the primary *in vitro* culturing of these cells is described in detail in appendix A.

2.1.1 Measurement of volume and curved surface area of axons

An interactive Matlab code (originally developed by Pramod A. Pullarkat) was used in order to detect the edge of an axon from phase contrast images (captured at 100X or 40X magnification) and measure the radius, curved surface area and volume. The code requires the axon to be straight and oriented horizontal (or parallel to X-axis of the image) and makes a basic assumption of axonal shape being cylindrical symmetric about their long axis. The following steps were involved in this method (more details can be found in [1]) :

(i) In the first frame of the image sequence, the user initializes the edge detection by drawing a rectangular box around most of the length of an axon and providing an initial guess for the minimum and maximum values of the axonal radius. Only the region within the box is considered then onwards as the code automatically traces the edge of the axon as per the steps below for all the time frames in a given time-lapse recording.

(ii) The code calculates the absolute value of gradient of the intensity (I) *i.e.* $\sqrt{\partial_x I^2 + \partial_y I^2}$ at each point. This is stored as a 2-dim array called as Norm, which is of the same size as the initially selected rectangular box.

(iii) The Norm is then scanned column-wise *i.e.* perpendicular to the axon's long axis in order to locate the maxima. In phase contrast images, edges of an axon show strong variation in the intensity. Thus the maxima in the intensity gradient give the row-positions of the two edges for that column.

(iv) Once row-locations of the edges are detected for a few starting columns, for the consequent columns, the code searches for the maxima within $\pm n$ (a user defined number) rows around the edge location corresponding to the previous column. Thus the edges are traced assuming a reasonably smooth axonal shape. The thickness or the radius is calculated at each point along the axon's length. From this, the differential curved surface area and differential volume are calculated along the length assuming cylindrical geometry. These quantities are then summed up and averaged per unit length.

2.1.2 Keeping an axon in focus using z-stack imaging

Typical time take for axonal beading after Noco treatment is about 10 to 15 min. This time is long enough for a live axon to drift out of focus which introduced error in the edge detection and therefore volume and area measurements. In order to avoid this error, we recorded a stack of z-slices (with an interval of $0.5\ \mu\text{m}$ or $1\ \mu\text{m}$) at each time point using the electronically controlled Z-movement of the microscope objective. This made sure that at every time point, the axon was found at the correct focus in at least one z-slice. The z-slice of correct focus for each time point was detected to be the one for which the contrast (= mean of the Norm array as calculated in subsection 1.1.1) is maximum given that the rectangular box of interest was drawn close to the axonal boundaries. The method was tested by cross-checking with visual detection of the z-slice at correct focus. It significantly reduced the error in the measurements.

2.1.3 Local application of a drug

We developed this method with an aim to expose only a small segment of an axon to a drug. This was achieved by using two glass micropipettes, one for infusion of the required drug (+ve pressure) and the other for suction (-ve pressure) to keep the flow of the drug limited to the desired zone. The pipettes were made from glass capillaries with diameter $0.5\ \text{mm}$, using a pipette pulling instrument (Flaming/Brown Micropipette Puller Model P-97, Sutter Instruments Co.). The tips of the pipettes were evenly cut to get a circular opening of the desired diameter using a Narishige Micro Forge MF-90. The end segments of the pipettes were made to bend at an angle in such a way that medium flow out of the infusion pipette and into the suction pipette was almost parallel to the surface of the sample-dish. The pressure applied to the pipettes was controlled using XenoWorks Digital Microinjector (Sutter Instruments Co.). Positions of the pipettes were well controlled using XenoWorks Micromanipulator (Sutter Instruments Co.), appended with a joystick for the XYZ movement of each of the two pipette holders as shown in fig. 2.2.

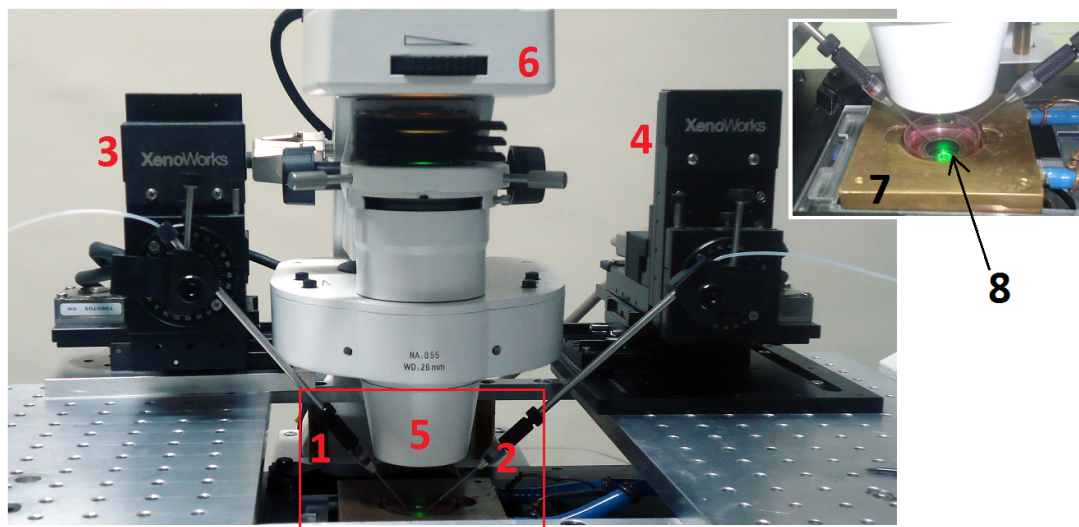


FIGURE 2.2: The set-up for local application of drug. The inset on right shows a better resolved picture of the rectangular part marked in red. Description of the numbered parts: 1. Injection pipette holder, 2. Suction pipette holder, 3. Micromanipulator for the infusion pipette, 4. Micromanipulator for the suction pipette, 5. Condenser and 6. Light source of the inverted microscope, 7. Brass incubator for keeping the cells at 37°C , 8. Sample i.e. petri dish with a glass bottom on which neurons are grown.

Diameter of the infusion pipette was kept between $4 - 8 \mu\text{m}$ and that for the suction pipette was kept at a larger value, between $12 - 18 \mu\text{m}$ in order to make sure that even the surrounding medium with some quantity of diffused drug gets continuously removed from the bulk medium in the dish so that the drug infusion remains really local. Thus we could produce a flow profile as shown in fig. 2.3 with this set-up. In order to image the profile, the infusion pipette on left was filled with the cell culture medium without methocel, supplemented with a fluorescent dye and fluorescent microbeads. The pipette on the right is the suction pipette. The flow was created on the surface of a sample dish filled with the medium without methocel. The fluorescent dye was used in order to mimic the range of diffusion of the drug and the microbeads were used to track the velocity profile of the local flow. In a real experiment, the locally infused medium consisted of the cell culture medium without methocel with Noco dissolved at a required final concentration. A very small concentration of fluorescent microbeads ($0.5 \mu\text{m}$) was mixed in this medium so that the continuity of the flow could be checked in the fluorescence light.

We found that with pressures set to their minimum possible values i.e. $+100 \text{ Pa}$ for infusion and -100 Pa for suction, the flow was confined to a width of $< 25 \mu\text{m}$

in a direction perpendicular to the flow. The selected axons for the experiment were at least 7 to 8 times longer than this length. It was possible to confine the flow to a shorter length by changing the magnitude of the pressures. However, any further increase in the pressure resulted in local deformations of the axon even in the absence of any drug, thus putting a limitation on improving the 'local'ness of the flow.

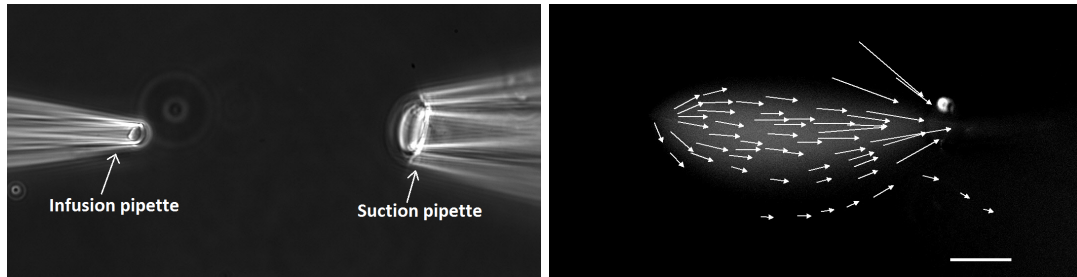


FIGURE 2.3: Arrangement of micropipettes (left, phase contrast image) and flow profile (right, image with RFP filter) for the local application of a drug. The pipettes are invisible in the image on right due to the fluorescence filters. The fluorescent image is captured by infusing cell culture medium with $1\mu\text{m}$ size beads (visualized using a GFP filter) plus rhodamine dye (visualized using a RFP filter) in a dish filled with the same medium without any fluorescent elements. Each arrows indicates trajectory of a fluorescent bead and the length of each arrow is directly proportional to the distance travelled by the corresponding bead in 400ms which was the set exposure time of the acquisition camera. The vertical spread of the flow as indicated by the background fluorescence of the dye, is tightly restricted to about $25\mu\text{m}$ at the centre of the flow. Very few beads escape the suction pipette. Bar: $20\mu\text{m}$

2.1.4 Fluorescence labelling

I. Fixed cells

Neuronal cells were first fixed then permeabilized using the following common protocol in all the subsequently mentioned procedures of specific labelling. All the solutions used were prepared in PHEM buffer (60 mM PIPES, 25 mM HEPES, 10 mM EGTA and 2 mM MgCl_2 , pH 6.9) as the solvent and also for rinsing the cells at various steps, unless mentioned otherwise. Fixative buffer: 3.2% paraformaldehyde (Electron Microscopy Sciences 15710), 0.05% glutaraldehyde (Electron Microscopy Sciences 16200)

Permeabilization buffer: 0.5% Triton X-100 (T8787 Sigma) in 1X PHEM buffer.

Protocol:

1. For fixation, cells were incubated in the fixative buffer for 10 min. at room

temperature.

2. After rinsing once, the cells were incubated in the permeabilization buffer for 30 min. at room temperature then washed thrice.

2.1.4.1 Tubulin

Tubulin was labelled using indirect immunofluorescence method as follows.

1. After fixation, and permeabilization, cells were blocked using 5% heat inactivated goat serum (ab CAM ab7481) for one hour at room temperature.
2. After rinsing four times, the cells were exposed to exposed to a primary antibody against α -Tubulin (DM1A monoclonal anti- α -tubulin, T6199 SIGMA) at 1:1000 for overnight at 4 °C.
3. After rinsing four times, the cells were exposed to the secondary antibody Alexa fluor 488 (Molecular Probes A-11001) at 1:10000 for one hour in the dark.
4. After washing four times the cells were imaged using Andor iXon 885 EMCCD camera at 100X magnification.

2.1.4.2 Neurofilaments

Neurofilaments were labelled using indirect immunofluorescence method as follows.

1. After fixation, and permeabilization, cells were blocked using 5% goat serum (HIGS) for one hour at room temperature.
2. After rinsing four times, the cells were exposed to exposed to a primary antibody against neurofilament (Developmental Studies Hybridoma Bank, USA 3A10) at 1:1000 for overnight at 4 °C.
3. After rinsing four times, the cells were exposed to the secondary antibody Alexa fluor 488 (Molecular Probes A-11001) at 1:10000 for one hour in the dark.
4. After rinsing four times the cells were imaged using Andor iXon 885 EMCCD camera at 100X magnification.

2.1.4.3 f-actin

F-actin was labelled using Phalloidin which specifically binds only to filamentous or polymerized actin. We used phalloidin conjugated with rhodamine (Fluka 77418). The protocol for labelling is as follows.

1. After the procedure for tubulin or NF labelling was completed, the cells were incubated with Rhodamine-Phalloidin at the final concentration of $0.025 \mu\text{g}$ per ml for 20 min. at room temperature.
2. After rinsing four times, the cells were ready to be imaged.

II. Live cells

2.1.4.4 Labelling with Calcein

Calcein (Sigma-Aldrich C1359, $\geq 4 \text{ mM}$ solution in DMSO) is a dye which labels the cytoplasm uniformly in live cells. Here, the purpose of Calcein labelling was to compare its fluorescence profile in axons with that of before mentioned cytoskeleton specific labelling. It was used at a final concentration of $20 \mu\text{M}$ in cell culture medium without methocel. Incubation with the dye at this concentration for more than 12 min. induces blebbing in axons. Therefore in the following protocol the cells were imaged within 9 min. after their first exposure to Calcein.

(A) CONTROL cells:

1. Growth medium is changed to full medium without methocel. Cells are incubated for an hour.
2. Loaded the cells on the microscope stage. Added $5 \mu\text{l}$ per 1 ml of the Calcein dye solution and incubated for 7 min. then gently washed once with medium without methocel then immediately imaged at 100X.

(B) NOCO treated cells:

1. Growth medium is changed to full medium without methocel. Cells are incubated for an hour.

2. Loaded the cells on the microscope stage. Added Noco at the final concentration of $16.7 \mu M$, incubated for 5 min.
3. Added $5 \mu l$ per $1 ml$ of the Calcein dye solution to the dish without changing the medium and incubated for 7 min. then gently washed once with medium without methocel then immediately imaged at 100X.

2.1.5 Imaging

All the experiments presented in this chapter were carried out on Axio Observer Z1 microscope with a motorized XYZ stage from Zeiss. The phase contrast images and time lapse videos were captured on Axiocam mRM with the help of AxioVision software by Zeiss. The fluorescent images were captured on a more sensitive Andor iXon 886 EMCCD camera with the help of Andor IQ software.

2.2 Results and Discussion

All the experiments presented below were performed at $36 \pm 1^\circ C$, using an on-stage (the microscope stage) brass casing through which warm water was continuously circulated. The temperature at the sample was calibrated using a platinum resistor.

2.2.1 Characterization of noco beading

Although the phenomenon of noco induced beading has been observed for decades, there has been no reporting of how percentage of the number of beaded axons changes with respect to concentration of the drug and the time of exposure to the drug. This information is relevant in understanding whether the shape change has a dependence on the reaction kinetics of Noco. We began our investigation with this point.

2.2.1.1 Percentage of beading with respect to concentration of Noco and exposure time

One hour prior to the experiment, the culture medium was changed to the pre-warmed medium without methocel, so that when the drug (Noco) was added, it's diffusion could be expected to be quick and uniform throughout the dish. From a population of axons of different calibers (fig. 2.5B)) and lengths in a culture, 'n' number of axons with length $> 50\mu m$ were randomly selected and their positions were recorded using the motorized X-Y control of the microscope stage. Images of these axons were captured before addition of the drug at a given concentration and after addition of the drug as a function of time. Data were collected from multiple dishes and pooled. The rare cases of pre-beaded axons and those which immediately retracted after the addition of the drug were discarded. The counting of the number of beaded axons was done manually. The result is shown in fig. 2.4(A).

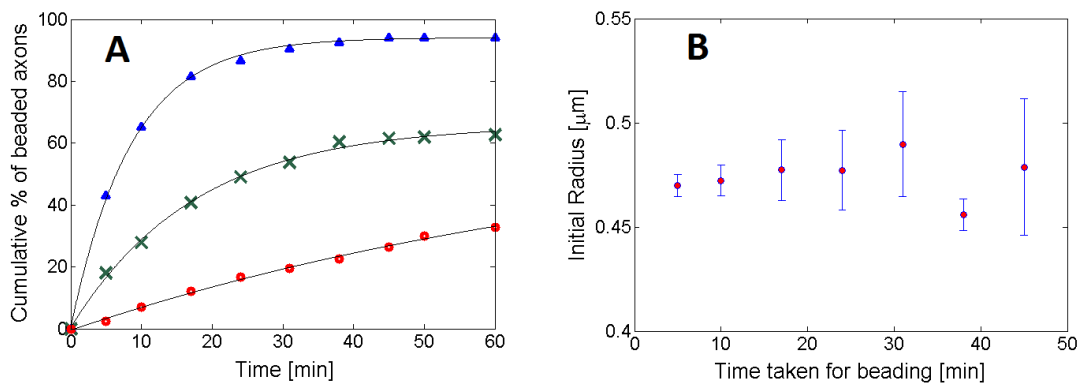


FIGURE 2.4: (A) Cumulative percentage of beaded axons with respect to time of exposure to 3 different concentrations of Noco: $0.33\ \mu M$, $3.33\ \mu M$ and $33.33\ \mu M$ shown in Red dots, Green 'x' and blue triangles with sample sizes 216, 255 and 135 axons respectively. At a much lower concentration of $0.03\ \mu M$ there was no beading seen within an hour after addition of the drug (data not shown). The corresponding exponential fits are shown by the black curves. (B) Mean radii of axons (total sample size = 107) versus the time taken for beading after exposure to $16.7\ \mu M$ Noco. The error bars show the standard error of the mean for each bin.

The plots show that the percentage of number of axons undergoing beading (p) rises rapidly initially, then saturates at a value dependent upon the Noco concentration. An exponential fit $\frac{p}{p_{max}} = 1 - \exp(-\frac{t}{\tau})$ where p_{max} is the saturation percentage and t is the time lapsed after addition of Noco, gives a time scale τ for each concentration as shown in table 2.1. τ is the time required for about 63%

of the total number of axons to undergo beading. It can be seen that τ decreases with increasing Noco concentration. At a very low concentration of $0.03 \mu M$ there was no beading seen within an hour after addition of the drug (data not shown).

Noco concentration [μM]	τ [min]
0.33	83.41
3.33	17.58
33.3	8.54

TABLE 2.1: Characteristic time of beading for different Noco concentrations

It can be seen that for $33 \mu M$ concentration, the percentage of beading axons saturates to more than 90 % within 15 minutes after addition of the drug. We have used a concentration of the same order i.e. $16.7 \mu M$ for all further experiments, so that the final concentration of DMSO (solute for preparing stock solution of Noco) does not exceed 0.1 % v/v. Note that DMSO alone does not affect the axon morphology even at 1 % v/v.

Because fig. 2.4(A) shows that axons take a wide range of time from a few to several minutes for the beading shape change, it was natural to ask what dictates this behavior. If it were simply the amount of MTs depolymerized in an axon at a given point of time, then the thicker axons with presumably more number of MTs should take a longer time to show beading. To verify this argument, we plotted binned values of the initial radii of 107 axons (before exposure to Noco) as a function of the time taken for beading (fig. 2.4(B)). Radius was measured using a Matlab code as described in the Methods section. Each error bar equals the standard error in radii measurements in a given bin corresponding to a given time of beading. The beading time can be seen to be independent of the axon caliber. This is contrary to the observations of osmotic shock induced pearling instability in axons where thinner axons are easier to destabilize [2].

2.2.1.2 Spatial Distribution of beads

Unlike osmotic shock induced pearling, the Noco-beading does not appear to have a well defined periodicity of beads. The distribution of the separation or distance between consecutive beads was measured in order to find whether there exists a characteristic length associated with the Noco-beading. Neuronal cells in the cell culture medium without methocel were exposed to $16.7 \mu M$ Noco for about 15 min. Snapshots of beaded axons were taken. Positions of the beads in each image were marked manually through an interactive Matlab code and the values of distances between consecutive beads were pooled. The distribution of the separation values (fig. 2.5) looks broad with mean $18.6 \mu m$ and standard deviation $7.4 \mu m$ for $n = 491$ data points.

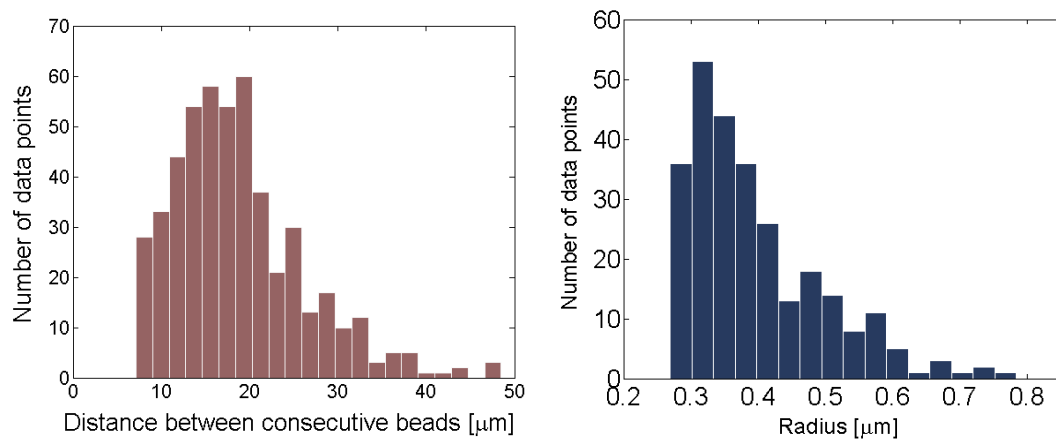


FIGURE 2.5: (A) Distribution of distance between consecutive beads (sample size = 490) for Noco-beaded axons after about 15 min. exposure to the drug at $16.7 \mu M$ (B) Distribution of radii of a population of untreated (or control) axons with sample size = 272, imaged at 100X. Axons with radii smaller than the optical resolution ($\sim 0.26 \mu m$) are excluded.

The broadness of the distribution could be arising from the following factors:

(a) In the presented distribution, the inter-bead separation is averaged over several axons with a broad distribution of diameters (fig. 2.5B)

(b) The fact that the even while they form, Noco-beads are not static as opposed to the pearling due to osmotic shock. Video recordings (next section) show that the beads may move along an axon during and after formation, and sometimes also merge to form bigger beads. The merging might be one of the reasons for the

lower cut off on the bead-separation in fig. 2.5. This observation will be discussed in detail later.

2.2.1.3 Effect of ATP depletion on Noco-beading

In the investigation of mechanism of the beading process it is important to find out which components of the system are involved and what roles they play. As a first step, one may inquire if the process is active or passive by studying the effect of Noco in an ATP depleted environment. In this order, axonal cultures were rinsed with the ATP chelating buffer (see Appendix A) using a flow chamber with a gentle flow of $70 \mu\text{l}$ per min., followed by incubation in the same buffer for about 20 min. at 37°C by which time the intra-axonal transport gets almost paused, indicating that the energy sources in the axons are depleted. Then Noco was added to the cells at $16.7 \mu\text{M}$. The percentage of beaded axons as a function of time of Noco exposure in control v/s ATP depleted conditions is shown in fig. 2.6.

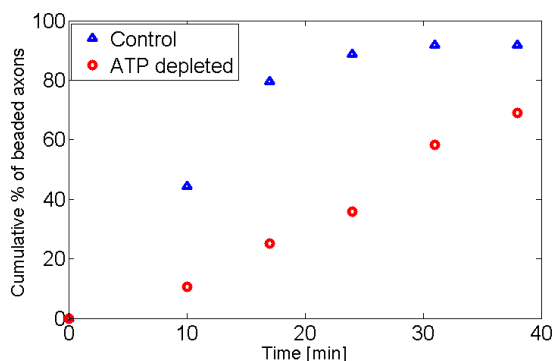


FIGURE 2.6: Cumulative percentage of beaded axons with respect to time duration of exposure to Nocodazole at $16.7 \mu\text{M}$ in control (blue triangles) and ATP depleted (red dots) condition

Fig. 2.6 clearly shows that the rate of axonal beading in ATP depleted condition is clearly lower than that in control condition. A longer incubation time of 50 min. or more in the ATP depletion buffer, prior to the Noco treatment, results in complete inhibition of beading. These observations may imply that Noco beading is an active process. However, there is a note of caution! It has been shown that MT disassembly is regulated by amount of cellular ATP [3] [4]. MT depolymerization by drugs such as colcemid, vinblastine and Noco was found to get inhibited when

the cellular ATP was depleted. In order to verify this, we used primary fibroblast cells from the peripheral tissue of the chicken DRGs which were immunolabelled for tubulin. In spread fibroblast cells, individual MT filaments can be distinctly seen as shown in fig. 2.7. A treatment with $16.7 \mu M$ Noco for 17 min. at $37 \pm 1^\circ C$ disrupts most of the MTs as shown in fig. 2.8, leaving behind mostly tubulin mass. However, when the cells were first depleted of ATP and then subjected to Noco treatment at the same concentration and incubation time as the control cells, a remarkable amount of MTs which remained unaffected by Noco treatment as shown in fig. 2.9. All the images are false-colored in green.

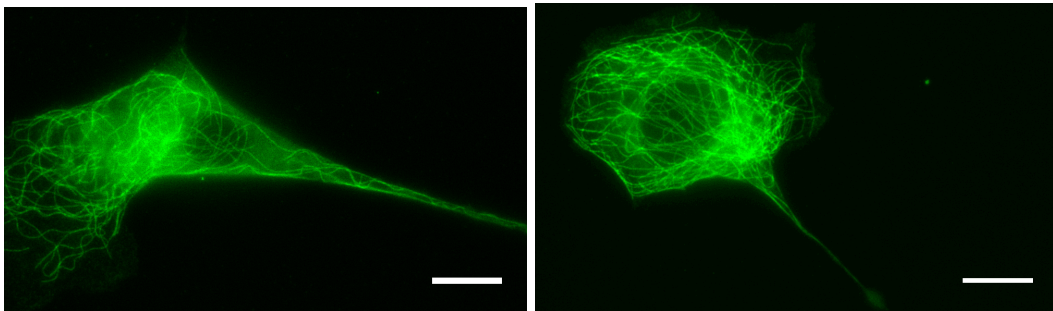


FIGURE 2.7: Immunolabelled tubulin in chicken embryonic fibroblast cells. Each bar: $10 \mu m$

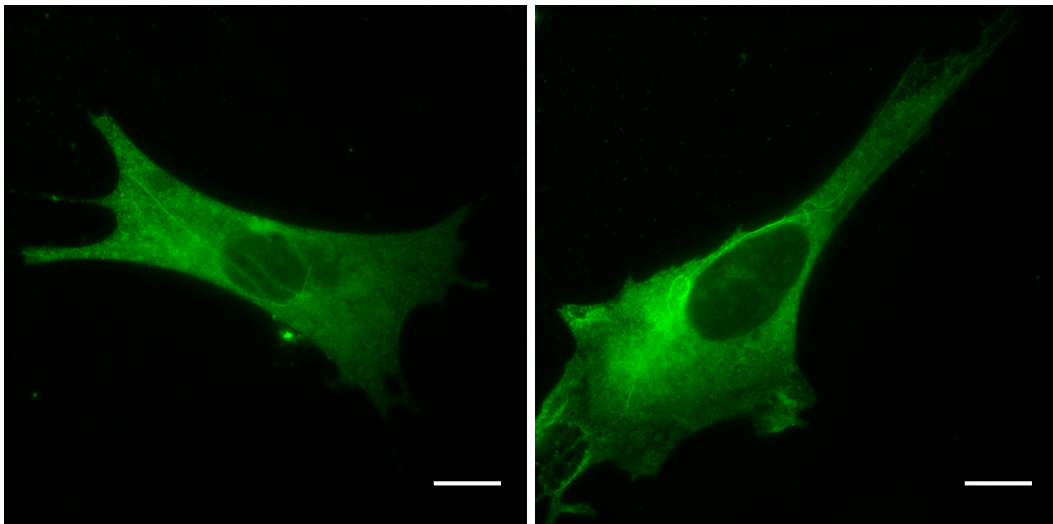


FIGURE 2.8: Immunolabelled tubulin in chicken embryonic fibroblast cells treated with $16.7 \mu M$ Noco for 17 min. Each bar: $10 \mu m$

Therefore, the diminished rate of Noco-beading in ATP depleted condition could be because most of the MTs in axons remain intact in spite of the Noco treatment. Thus, this experiment can not determine whether Noco-beading is an active process.

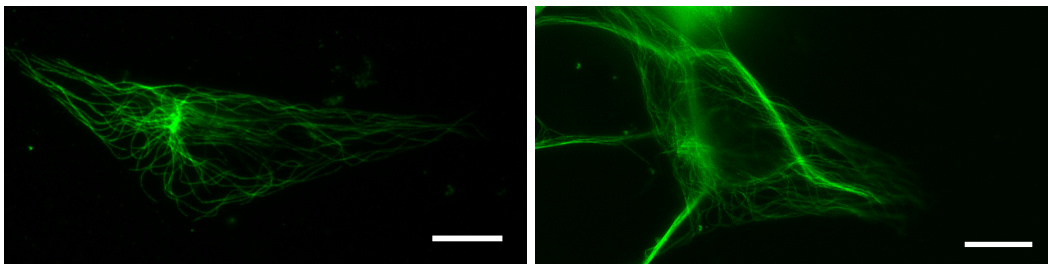


FIGURE 2.9: Immunolabelled tubulin in chicken embryonic fibroblast cells which were first depleted of ATP and then treated with $16.7 \mu M$ Noco for 17 min. Each bar: $10 \mu m$

2.2.2 Verifying the known mechanisms of axonal beading

We saw in the previous chapter that axonal beading is seen in many conditions *in vivo* and *in vitro*. However, the mechanisms of this shape change is known in only a few cases and they can be classified in the following two categories:

- I. Pearling instability triggered by sudden rise in the axonal membrane tension like in the scenarios of nerve stretching [5] and hypo-osmotic shock [2].
- II. Local loss or discontinuities in the axonal MT tracks or impairment of MT based transport resulting in traffic jam of synaptic vesicles and other organelles like in the case of axonal stretch injury [6] and in mouse models of Alzheimer's disease [7].

In the following, we discuss the experiments and results concerning the validity of these two mechanisms in the context of Noco induced axonal beading.

2.2.2.1 Pearling instability due to Hypo-osmotic shock

As described in the Introduction chapter, application of a hypo-osmotic shock results in a sudden influx of water through the axonal membrane, causing the axon to swell. The swelling results in rise in the membrane tension, which when exceeds a critical value, triggers the pearling instability. In the case of Noco treatment, the resultant disruption of axonal MTs can be viewed as a replacement of the filaments by a large number of tubulin sub-units all along the length of the axon. Thus, rise in the concentration of tubulin sub-units can cause an osmotic pressure difference across the axonal membrane, leading to swelling and pearling. Therefore the mechanism of Noco-beading could be similar to that of osmotic shock induced

pearling of axons. We tested this hypothesis by the means of comparing with the characteristic behaviour of the latter mechanism as discussed below.

I. Periodicity of pearling/beading

Osmotic shock induced pearling typically shows up with the fastest growing mode with a well defined wavelength (λ_m) as described in Chapter 1 (fig. 1.6). In the case of Noco-beading, the distance between consecutive beads (d) is not a constant (fig. 2.1). Hence, a wavelength can not be defined in this case. It can be also seen from these figures that d is typically much larger than λ_m . We wanted to compare λ_m and d for the same axon. The result is presented in fig. 2.10. Here, the axons were first subjected to a hypo-osmotic shock by changing the growth medium to the cell culture medium without methocel, diluted by adding water at 10% v/v. This resulted in the pearling instability as shown in fig. 2.10(A1, B1, C1) which relaxed in a few minutes. The axons were incubated for an hour for complete recovery and then subjected to 16.7 μM Noco for 15 to 20 min. The pictures on the right in fig. 2.10 show the Noco-beaded counterparts of the same axons as on the left. Note that the periodicity of pearling in the images on left in fig. 2.10 is not as good as that seen in the pictures of pearled axons in Chapter 1 (fig. 1.6). This is probably because a much milder osmotic shock was applied in the cases shown in fig. 2.10(A1, B1, C1), in order to keep the axons minimally perturbed before proceeding for the Noco treatment. Even though d can be seen to be larger than λ_m in these cases, the shape transformations on left and right do not look very different from each other. Therefore further detailed comparisons were needed.

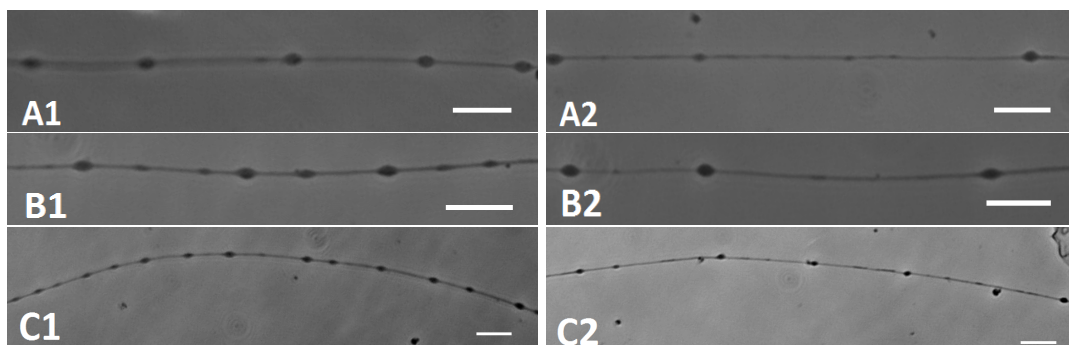


FIGURE 2.10: Comparison of osmotic shock pearling and Noco beading of axons. All images on the left show axons pearled due to hypo-osmotic shock. All images on the right show the same respective axons beaded due to Nocodazole treatment. Scale bars:

10 μm

II. Relationship between the initial radius (R_0) and wavelength of the fastest growing mode (λ_{max})

Osmotic shock induced pearling has a periodicity λ_{max} which linearly depends upon R_0 [2]. The following plot shows the Noco-beading data for initial radius R_0 i.e. radius of an axon before exposure to Noco and the average distance between consecutive beads λ after exposure to Noco, for $n = 50$ axons. λ is calculated by averaging consecutive distances between multiple beads formed on each axon and each data point corresponds to a different axon. It can be seen that in the case of Noco-beading there is no correlation between R_0 and λ .

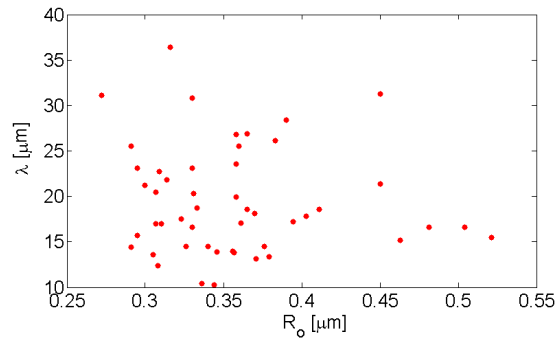


FIGURE 2.11: Initial radius R_0 i.e. radius of an axon before exposure to Noco and the average distance between consecutive beads λ after exposure to Noco. Each data point corresponds to a different axon.

III. Evolution of axonal volume and curved surface area

The following plots (fig. 2.12 and fig. 2.13) show the evolution of volume and curved surface area when an axon was first subjected to osmotic shock and when the same axon was exposed to Noco. The whole experiment was carried out in a flow chamber with the medium flow rate $70 \mu\text{l}$ per min with the temperature maintained at $37 \pm 1^\circ\text{C}$ using a warm water circulator. Osmotic shock was applied by replacing the growth medium by the cell culture medium without methocel, diluted with 20% v/v double distilled water. This resulted in the pearling instability of the axon as shown in fig. 2.12. The phase contrast time lapse images of the axons were analyzed using the Matlab code described in the Methods section. Axonal volume per unit length (V) and curved surface area per unit length (A) were normalized using their respective initial values.

The normalized volume \bar{V} and normalized area \bar{A} evolve just as described in [2] with respect to the application of osmotic shock. The instant at which the dilution flow was turned on is taken as $t = 0s$. The shape ratio ($\sqrt{\bar{V}}/\bar{A}$) is an indicator of any deviation from the uniform cylindrical geometry of an axon. Its value equals 1 for a uniform cylinder and rises above 1 for the beaded shape for which the area is smaller than area of a uniform cylinder of the same volume as explained in the Introduction chapter. Thus we can see that the pearling instability sets in at $t \approx 60s$ and vanishes at $t \approx 160s$. The gap in the data from $t = 170s$ to $t = 210s$ is due to the presence of a cell-debris carried with the flow over the axon, preventing the correct tracing of the axon.

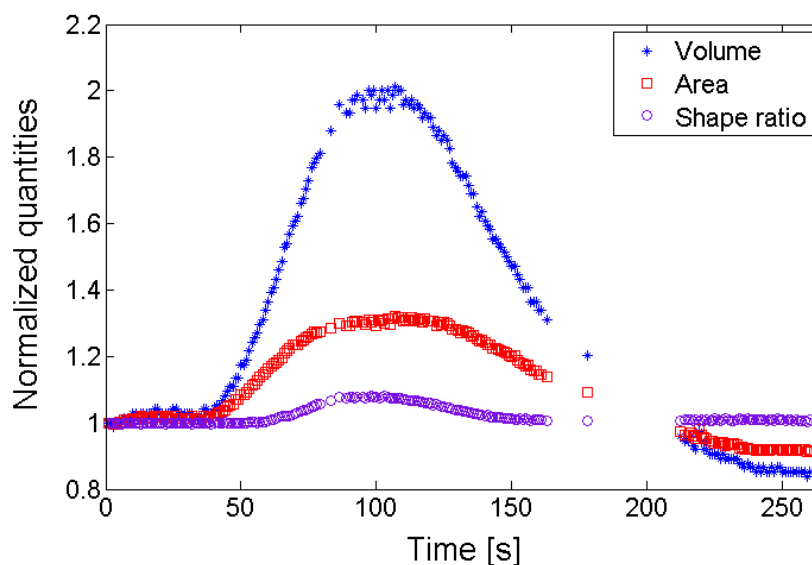


FIGURE 2.12: The plot shows evolution of normalized volume (blue asterisks), normalized area (red squares) and the shape ratio $\sqrt{\bar{V}}/\bar{A}$ (purple circles) with respect to the time after flow of the diluted medium was switched on. The axon images in the lower panel correspond to the indicated time (in seconds) lapsed after the dilution flow was turned on.

After the shape relaxation, the axon was incubated for one hour for recovery. Then the existing medium in the flow chamber was gradually replaced by the medium plus Noco ($16.7 \mu M$) by a flow at $70 \mu l$ per min. Again the normalized volume, curved surface area and the shape ratio were plotted as functions of time beginning from 3 min. after the flow was turned on till the beading had just begun (fig. 2.13).

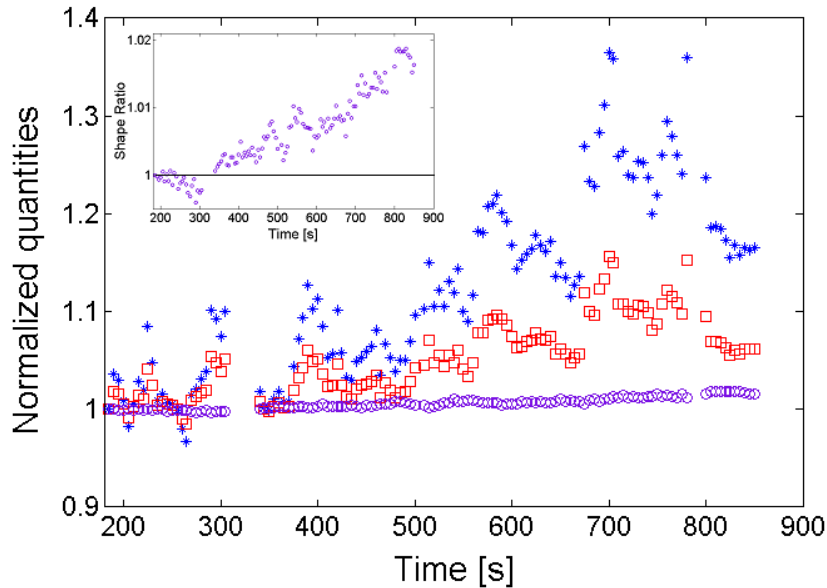


FIGURE 2.13: The plot shows evolution of normalized volume (blue asterisks), normalized area (red squares) and the shape ratio \sqrt{V}/\bar{A} (purple circles) with respect to the time after flow of the Noco medium was switched on. **INSET:** evolution of the shape ratio which varies on a smaller scale compared to the volume and area but steadily rises above 1 (marked with a solid black line) with time, indicating the change in the geometry of the axon. The images of the axon in the lower panel correspond to the time in seconds indicated on the image. The white arrows show the locations of the mild beading at the onset.

From the above plots it can be seen the changes in volume, surface area and shape ratio of an axon in the case of osmotic shock pearling and Noco-beading take place by very different amounts and rates. The area and volume just *before* the onset of osmotic pearling are respectively about 16% and 36% larger than their initial values and rise up to 30% and 100% at their respective peaks in the presented example. Whereas, in the case of Noco-beading, the area and volume begin to rise not a priori but *simultaneously* with the shape deformation. Even as the shape ratio increases with time, indicating a growing amplitude of beading, the rise in the area and volume is much slower and by a much smaller amount as compared to the case of osmotic shock induced pearling.

The time taken for Noco-beading to set-in (over a few to several minutes), is long enough for a live axon to undergo changes in its position. Especially the movement along the axis of the microscope makes an axon to go in and out of focus, introducing errors in the measured values of area and volume. This problem was tackled by imaging multiple z-slices at every time-point so that an axon is in

focus in at least one of the many z-slices at any given time point. This slows down the rate of acquisition but increases the accuracy of measurements. The accuracy is determined by acquiring z-stack images of an axon fixed with aldehyde treatment for a time comparable to the experimental time, then measuring the relevant geometric quantities using a Matlab code for z-stacks as mentioned in the Methods section. The following plots (fig. 2.14) show volume and shape evolutions of axons with better accuracy.

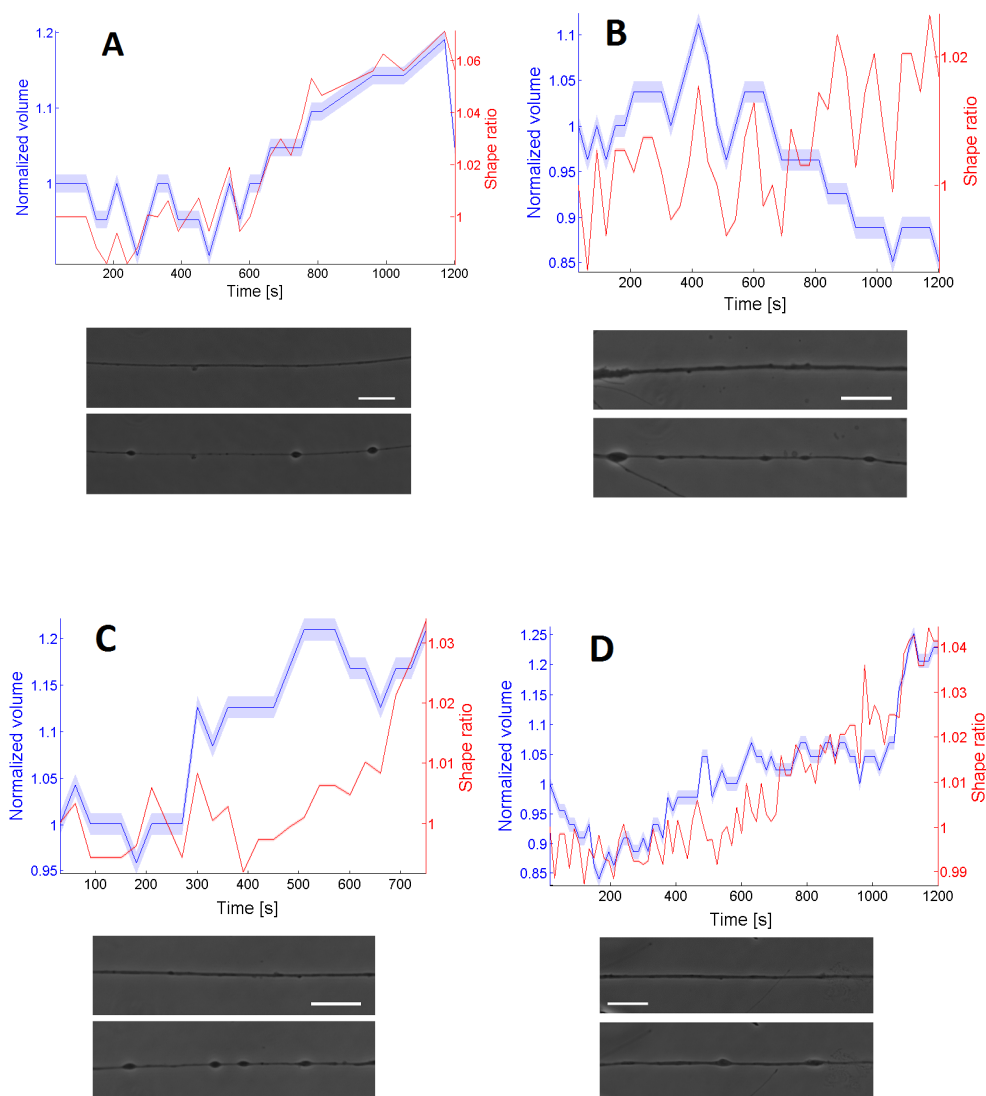


FIGURE 2.14: Evolution of normalized volume (blue) and shape ratio (red) for four axons undergoing Noco-beading. The shaded region around every line in the plots represents the error in the measurement. The phase contrast images show the corresponding axon before and after Noco-beading. Each bar: $10 \mu m$

As indicated by the shape ratio values rising above 1, the axon in each of the above cases underwent beading and the volume also increased, although by only few percents, except in case (B). However, in all the above plots, just before the onset of beading (i.e. before the shape ratio starts rising above 1) either there is no rise the volume or the rise is insignificant and takes place at a much slower rate compared to the typical rate of rise in volume before the osmotic shock pearling instability (fig. 2.12). Thus, in the case of Noco-beading, there is no significant axonal swelling *prior* to the shape transformation in comparison with that in the case of osmotic shock pearling. It is also important to note from fig. 2.12 that even though the volume rapidly rises during the onset of the osmotic shock induced pearling instability, the subsequent relaxation of the volume within a couple of minutes implies that there exist(s) mechanism(s) by which axons regulate their volume [2]. This relaxation time is much shorter compared to the time taken for the beginning of shape change in the case of Noco-beading. Therefore, we can conclude that the cause of Noco-beading can not be axonal swelling.

IV. Reversibility of the shape transformation

Osmotic shock induced pearling is a reversible shape change and the evolution of shape ratio in fig. 2.12 shows that an axon gets back to its uniform radius geometry by regulating the volume and area in the presence of the diluted surroundings. Noco induced beading, on the contrary, is not only irreversible in the presence of the drug in the medium, but also observed not to allow the axons to get back to their original geometry even after washing the drug away. The axons continue to get further distorted or get retracted after washing the drug away just after the onset of beading. This may not imply that MTs in axons fail to re-polymerize after Noco is washed away, but one can conclude that the reorganization of intra-axonal material during the process of Noco-beading may not be reversible.

V. Noco-beading begins from the growth cone

Osmotic shock induced pearling instability develops simultaneously and uniformly across the entire length of the axon. Noco is a membrane permeable drug and therefore it may be expected that it disrupts MTs across the entire length of an axon simultaneously and gives rise to beading. However, in the case of axons which have distinct or *free* Growth Cones (GCs) unconnected to the other neuronal cells

in the culture, we observed that exposure to Noco initiates retraction of the GC (as shown in Fig. 2.15), giving rise to a flow of the material being retracted, which culminates into beading of the distal part.

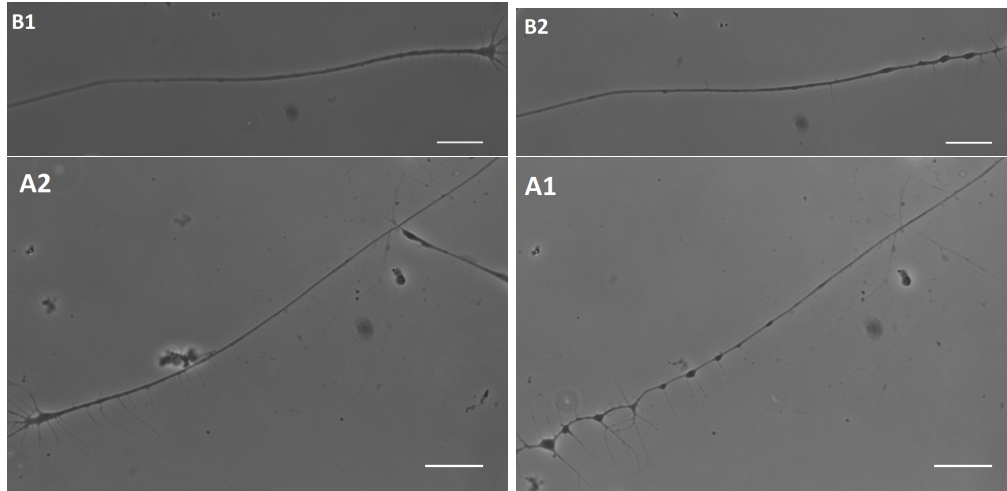


FIGURE 2.15: Noco-beading begins from the distal or growth cone end of axons. A1 and B1 show axons before Noco treatment. A2, B2 show the same respective axons at an early stage of Noco-beading. Each bar: $20\ \mu m$

The reason behind this peculiar behaviour may be explained on the basis of region dependent stability of MTs along an axon. The most distal region of an axon mainly contains labile MTs while the main shaft contains both labile and stable MTs [8]. Therefore, MTs ending in the axonal GC may get disrupted by Noco much earlier than those located in the shaft, thus causing the shape change beginning with the distal part. The gradual proceeding of the beading shape transformation towards the proximal part supports the visual impression of a retrograde flow of the intra-axonal material.

2.2.2.2 Membrane Tension measurements

As discussed in the subsection on osmotic shock induced pearling in Chapter 1, the cylindrical shape is unstable to membrane tension values exceeding the critical membrane tension given by

$$\sigma_c = \frac{6K\mu R_c}{K + \frac{4}{3}\mu}$$

where K is the bulk compression and μ is the shear modulus of the cytoskeleton gel and R_c is the radius of axon just before the onset of the instability. Considering

the typical values of $K = 20 \text{ kPa}$ [2], $\mu = 1 \text{ kPa}$ [9] and $R_c \sim 0.5 \mu\text{m}$ one gets $\sigma_c = 3 \times 10^{-3} \text{ Nm}^{-1}$. This value is very high compared to the typical membrane tension value for untreated axons $\approx 5.5 \times 10^{-6} \text{ Nm}^{-1}$ and Noco-beaded axons $\approx 7.2 \times 10^{-6} \text{ Nm}^{-1}$ as measured from the tether pulling experiments described in Chapter 4. However, MT-depolymerization after Noco treatment may bring down the values of K and μ , resulting in a much lower critical membrane tension. For example, if K reduces by 1000-fold to $\approx 20 \text{ Pa}$ and μ to $\approx 1 \text{ Pa}$ then $\sigma_c \approx 3 \times 10^{-6} \text{ Nm}^{-1}$. Thus, if the elastic moduli of the cytoskeleton get drastically reduced after Noco treatment, the axon may undergo a shape transformation due to the rest membrane tension.

All the results discussed above show that shape change in the case Noco beading does not have its origin in a possible change in the osmotic conditions inside and outside the axons.

2.2.2.3 Verifying the hypothesis of Local disruption of Microtubules and consequent Traffic jam

As explained in the Introduction chapter, there have been investigations on axonal beading caused by impairment of MT based transport [7] or local loss of MTs [6], resulting in the accumulations of vesicles and mitochondria. A similar hypothesis for beading induced by Vinblastine (another MT-depolymerizing drug) was proposed, where on the basis of fluorescence immunolabelling it was claimed that the beading occurs because the intact MTs are absent at the sites of beading as opposed to those being present in the segments between the beads [10]. It was proposed that such defects in the MT tracks gives rise to accumulation of transport vesicles and cargoes in the regions where the intact MTs are absent which results in the bulged or beaded geometry. It is important to note that in most of these works, the imaged axons were fixed at *matured stages of beading*. Therefore the observed accumulation of objects inside the beaded regions does not imply that the beading itself was caused by the accumulation. The dynamics during the onset of beading remains unexplored. Our observations of the live dynamics at the onset of Noco-beading are described in the following:

- **Intra-axonal transport is not stalled prior to and during the process of Noco-beading**

In most of the previous studies, the hypothesis of impairment of intra-axonal transport or traffic jam as the principal cause of axonal beading was proposed based on electron micrographs of the beaded regions in fixed axons. However, the dynamics of the shape change was not captured in live cells. Our observation of Noco-beaded axons at high magnifications (100X or more) shows that the intra-axonal transport continues to take place even after bead formation. **Movies *Transport-1 to 4*** are presented as experimental evidences to prove this claim. Please note that all movies which are an integral part of this thesis work and referred to at various places can be found at www.rri.res.in/thesis_Anagha_movies (username: thesis and password: An@rri.th), organized chapter-wise.

Movie *Transport-1*: One can see the state of intra-axonal transport while Noco-beading takes place. The transport is unhindered at the onset of beading and slows down only towards the end of the movie as the beads get enlarged and the segments between the beads become very thin. This shows that Noco-beading is not triggered by impairment of transport. The time after addition of Noco is shown in the upper left corner in minute:second.

Movie *Transport-2*: This movie shows particles having size comparable with the axonal radius, passing unobstructed for a few tens of μm through the Noco-beaded axon. A relative time duration of the movie is shown in the upper left corner in seconds.

Movie *Transport-3*: One can see many small and large particles being transported through Noco beads. One can also see the fluctuations in the positions of the Noco-beads along the axon and continued bi-directional transport of particles through the beaded regions. This rules out the possibility of an internal flow being the reason for the observed motion of the particles.

Movie *Transport-4*: This high magnification movie clearly shows the trajectory of a particle as it passes through a large Noco-bead. The curved nature

of the trajectory along the shape of the bead suggests that after Noco treatment, the remaining MT tracks lose their usual co-axial orientation especially at the sites of bead formation.

The modes of intra-axonal transport other than MT based transport, like myosin Va [11] can not be responsible for the movement of particles over such long lengths as few tens of μm . Thus we suspect that there remain a few stable MTs unaffected by the Noco treatment, on which the long distance transport is continued.

Note: In the presented phase contrast movies, it is very difficult to plot kymographs of the moving particles. But the particle movement is very clearly visible to eye. We also made several attempts at fluorescently labelling the vesicles for a better visualization of the movement, which turned out to be unsuccessful due to a poor efficiency of the labelling or a fast bleaching rate compared to the required time of observation or due to inability of the labelled vesicles to show the usually fast transport in axons as compared to the non-labelled vesicles.

- **Noco beads can move along the axon and also merge**

If the beads were formed due to traffic jams of vesicles and cargoes at the sites of local disruption of MTs, they would have been static. However we often see that the beads move transiently as shown in fig. 2.16. It is important to note that once a bead moves, there is no fresh bead-formation at its previous location; *implying that there may not be any structural anomaly associated with the sites of bead formation.*

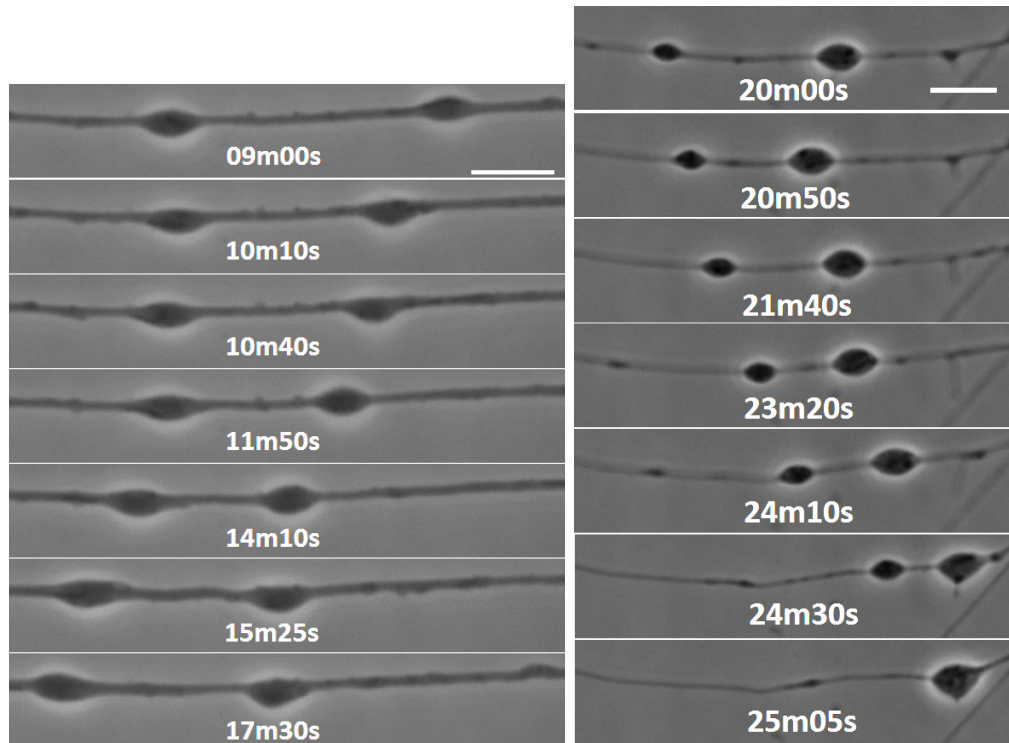


FIGURE 2.16: Clips from time lapse videos of Noco-bead movements. Each clip shows time in minutes (m) and seconds (s) after exposure to $16.7 \mu M$ Noco. Note that there is no fresh bead-formation at the previous location of a moving bead. Bead merger can be seen in the panel on right. Each bar: $5 \mu m$

More examples of movement of Noco-beads along axons and bead merging events can be seen in the movies *Bead-merge-1* and *Bead-merge-2*.

These observations indicate that there is no jamming of intra-axonal transport prior to the Noco-induced beading of axons. The next experiment was attempted in order to bring about local discontinuity in the MT organization in axons by exposing only a small segment of an axon to Noco. Although the disruption of MTs was not imaged at the location of the drug exposure we have indirectly tested that the drug does act in the expected way as explained in the following:

2.2.3 Local application of Nocodazole

Axons of length greater than $150 \mu m$ were chosen and subjected to an exposure of Noco restricted to about $20 - 25 \mu m$ long segment at a time using the method of local application as described in the Methods section. About 30 min. prior to the experiment, the growth medium was changed to full medium without methocel.

For drug infusion, full medium without methocel, supplemented with micron size fluorescent beads and Noco at $33 \mu M$ was used. The sample dish had to be kept open during the experiment to make way for the infusion and suction pipettes. The cells were incubated at $36 \pm 1^\circ C$ (checked using a Platinum resistor) throughout the experiment using a casing connected to a hot water circulator. To minimize the evaporation of the medium, a very thin layer of mineral oil was deposited on the medium-air interface. Local flow generated between the two pipettes was applied at the middle shaft and the growth cones (GCs) of axons as shown in fig. 2.17.

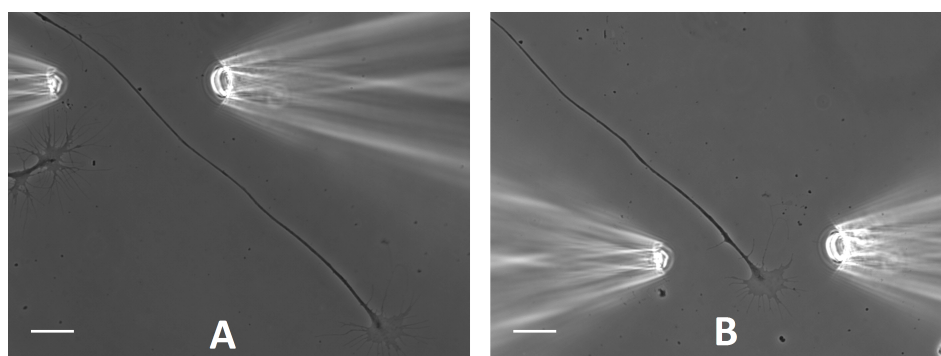


FIGURE 2.17: Local application of Noco at (A) Middle segment of an axon and (B) Growth cone of the same axon, using an infusion pipette on left and a suction pipette on right. Bar: $20 \mu m$

The following movies are representative of the general observations. In all the movies, the infusion pipette is placed on the Left and the suction pipette is placed on the Right side of the frame. The dark frames correspond to fluorescence mode of imaging where one can see fluorescent beads flowing out of the infusion pipette and getting pulled into the suction pipette, indicating that the local flow is working as expected.

Movie **Local-1-control-shaft** and **Local-2-control-GC**: These movies show that the local application of flow of Control medium (full medium without methocel, without Noco, with fluorescent beads) does not deform the shape of axonal shaft and GC respectively. The numbers on top-left show time in minute:second. In the high magnification GC movie, tips of the two pipettes can be seen on the left and right edges of the frame.

Movie **Local-3-noco**: In this movie, Noco was locally applied first to the proximal shaft of an axon for about 17 minutes then to the GC of the same axon. The proximal shaft remains unaffected by the drug application whereas the GC begins to retract within first 4 minutes. The numbers on top-right show time in minute:second.

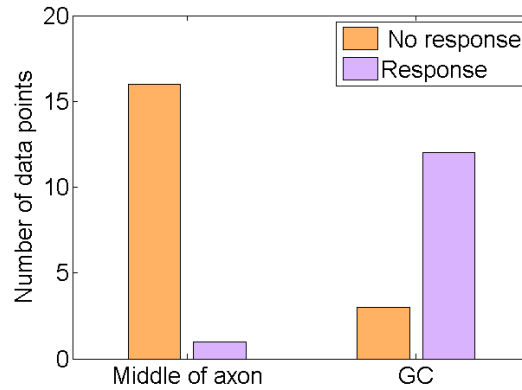


FIGURE 2.18: Response in terms of retraction or beading to local application of Nocodazole, depending upon the location of the drug application. Distal shaft next to the growth cone is seen to be much more vulnerable than the proximal shaft.

Observations: Local application of flow of control medium (without Noco) does not cause any shape change of axons, irrespective of whether it is applied at the middle shaft or at the GC. Application of Noco to a small segment of the axonal shaft, away from the GC, does not induce beading or any other shape change. If the drug is locally applied to the GC, there is a response in the form of retraction within a couple of minutes, which may lead to bead formation. As shown in fig. 2.17, in 1 out of 17 trials of local application of Noco for at least 10 minutes each, a response in terms of change of shape was seen. Whereas 12 out of 15 GCs, responded with either retraction or bead formation within a few minutes of the local Noco application.

These observations imply that beading cannot be caused locally on axonal shafts. The reason behind this, just like the reason behind Noco-beading beginning from the GC end of axons, could lie in the fact that the most distal region (just next to GC) of an axon mainly contains labile MTs while the main shaft contains both labile and stable MTs [8]. Therefore, local application of Noco at the middle shaft may cause depolymerization of relatively much lower fraction of MTs than that at the GC. Another reason behind the observed behaviour may lie in the length

distribution of MTs in the axons. It is known that this distribution depends upon the source (organism) and the type of neuron [12], [13]. If most of the individual MT filaments are much longer than the drug exposure span of the local application ($\sim 25 \mu m$) then this technique can bring about the disruption of a very small fraction of the MTs, which is insufficient to cause beading.

The next experiments investigate the role of cytoskeleton elements other than MTs in Noco-beading.

2.2.4 Verifying the role of Acto-Myosin contractility

f-actin and myosin motors together can generate contractile stresses in cells. MT disassembly induced by various drugs like Noco, colcemid, vinblastine boosts up acto-myosin contractility [14]. One may imagine the sites of Noco-beading along an axon to be the locations where there is a built up of concentration of contractile elements due to a force imbalance triggered by the MT disassembly. This hypothesis of actomyosin contractility giving rise to the beading after MT depolymerization can be tested at an elementary level by inhibiting the acto-myosin contractility in axons before exposing them to Noco. Acto-myosin contractility can be disrupted either by depolymerizing f-actin using Latrunculin-A (Lat-A) or by inhibiting the action of Myosin-II motors using Blebbistatin. We tried both the treatments.

1. Axons were first treated with $0.94 \mu M$ Latrunculin-A (Lat-A) in culture medium without methocel, for 20 min. at $37^\circ C$. Then they were treated with Noco at $16.7 \mu M$ with Lat-A still present in the medium. The percentage of beaded axons as a function of time duration of Noco exposure in control (i.e. no drug added prior to $16.7 \mu M$ Noco treatment) v/s Lat-A pretreated conditions is shown in fig. 2.19.

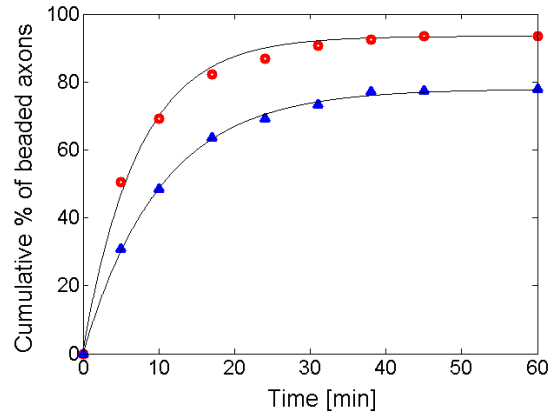


FIGURE 2.19: Cumulative percentage of beaded axons with respect to time duration of exposure to Nocodazole at $16.7 \mu M$ in cells directly treated with Noco alone (blue triangles) and those pre-treated with Lat-A then Noco (red dots).

The plot shows that depolymerization of f-actin enhances the rate and the percentage of Noco-beading. The fits are similar to those discussed earlier in fig. 2.4A, giving the characteristic time of beading τ for the Lat-A pretreated cells to be 7.32 min. while that for the control cells to be 10.26 min. This result not only disproves the hypothesis that Noco-beading is a result of acto-myosin contractility but shows that the process of Noco-beading gets accelerated with disassembly of f-actin.

2. Similarly it was observed that pre-treatment with Blebbistatin at about $20 \mu M$ for 20 min. does not inhibit Noco-beading. This result further rules out the requirement of acto-myosin contractility in the process of Noco-beading.

2.2.5 Fluorescence Imaging of Cytoskeleton

As beading is a shape deformation of the whole axon, it is essential to know how does it affect the spatial organization of different components of the axonal cytoskeleton. With this purpose, the technique of fluorescent labelling was used to study the distribution of tubulin, neurofilaments (NFs) and f-actin in Noco-beaded axons in comparison with that in untreated (control) axons. In the labelling procedure (Appendix B) the axons were first fixed using aldehyde treatment, then permeabilized, then incubated with the required protein-specific antibody (in the case of Tubulin and NF) or a protein-specific dye (in the case of f-actin). The

cytoskeleton specific labelling was also compared with cytoplasmic labelling of live axons (both control and Noco beaded) using Calcein. The results are as follows.

2.2.5.1 Control or untreated axons

Fig. 2.20 and fig. 2.21 show tubulin and f-actin co-labelling of two axons and fig. 2.22 shows images of NF immunolabelling and Calcein staining in control axons. Each image is accompanied with two intensity profiles. The first profile shows the intensity values integrated along the thickness of the axon at every point along its length. The second profile gives the intensity along a line drawn at the midsection of the axon and therefore is sensitive to the more local variation in the intensity. In order to compare the distribution of the cytoskeletal elements along the length of an axon, the intensity values are normalized with respect to the maximum value of intensity in each image.

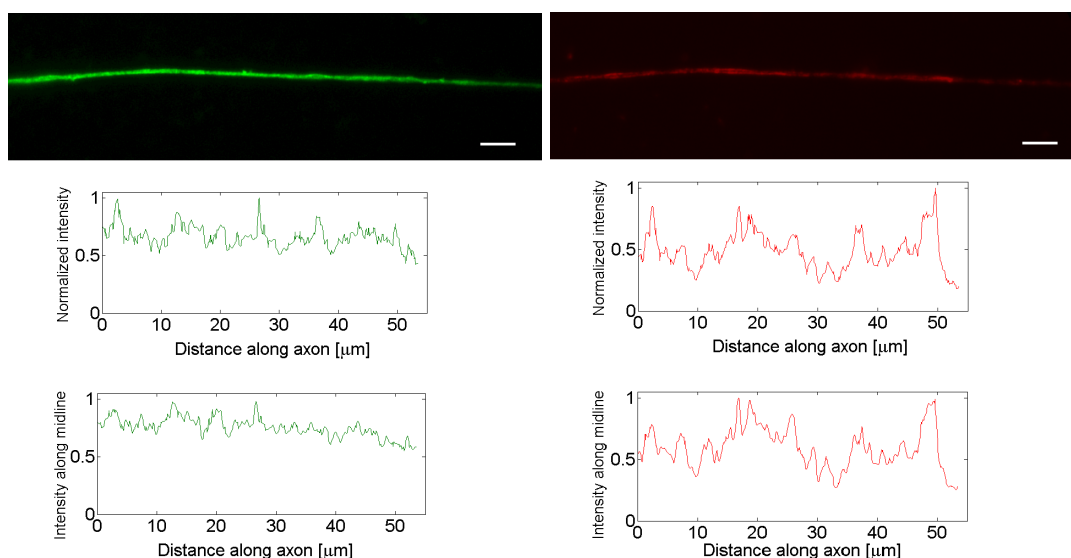


FIGURE 2.20: A control axon stained for α -tubulin (Left, green) and f-actin (Right, red). The upper plots show integrated intensity across the thickness of the axon, at every point along its length. The lower plots show intensity along the midsection of axon. The intensity values are normalized with respect to the maximum intensity value in each case. Scale bars : $5 \mu m$

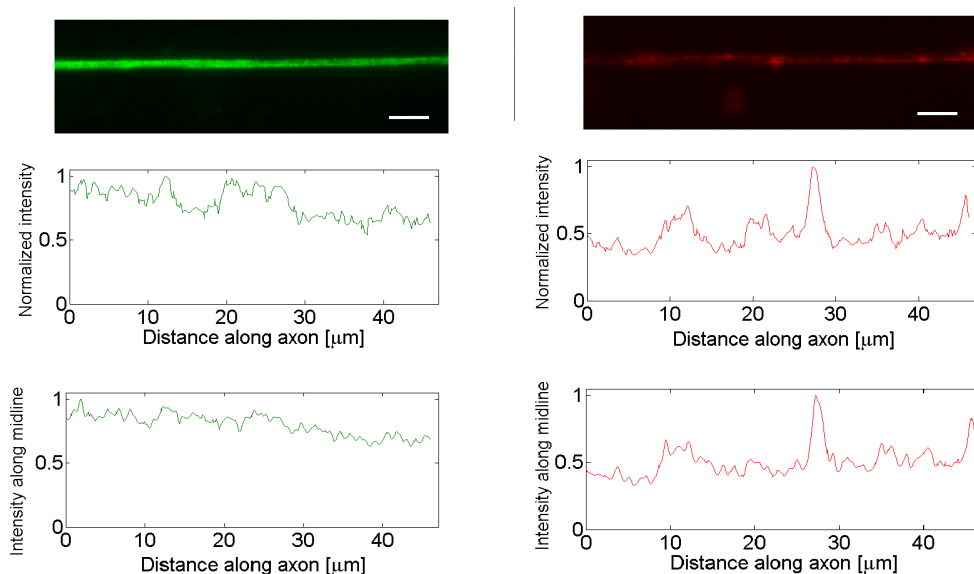


FIGURE 2.21: A control axon stained for α -tubulin (Left, green) and f-actin (Right, red). The upper plots show integrated intensity across the thickness of the axon, at every point along its length. The lower plots show intensity along a line at the midsection of the axon. The intensity values are normalized with respect to the maximum intensity value in each case. Scale bars : $5 \mu\text{m}$

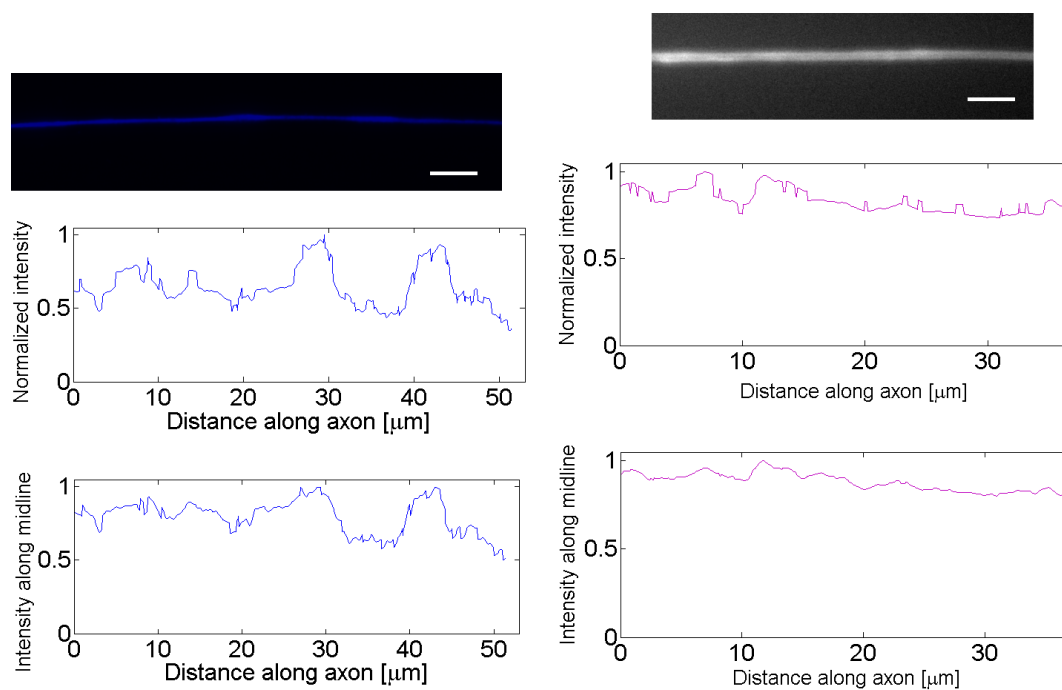


FIGURE 2.22: A control axon stained for neurofilaments (Left, blue) and Calcein (Right, grayscale). The upper plots show integrated intensity across the thickness of the axon, at every point along its length. The lower plots show intensity along a line at the midsection of the axon. The intensity values are normalized with respect to the maximum intensity value in each case. Scale bars : $5 \mu\text{m}$

It can be seen that tubulin and NF distributions are spatially more uniform along the axons compared to f-actin distribution but much lesser smooth compared to the Calcein profiles. The smoothness of the tubulin and NF line profiles indicate continuous presence of MT and NF filaments throughout the length of axons as opposed to the inhomogeneous f-actin distribution.

2.2.5.2 Noco-beaded axons

Fig. 2.23 and fig. 2.24 respectively show tubulin and f-actin co-labelling and fig. 2.25 and fig. 2.26 respectively show images of NF and Calcein staining for Noco-beaded axons. Each image is accompanied with two intensity profiles as described previously.

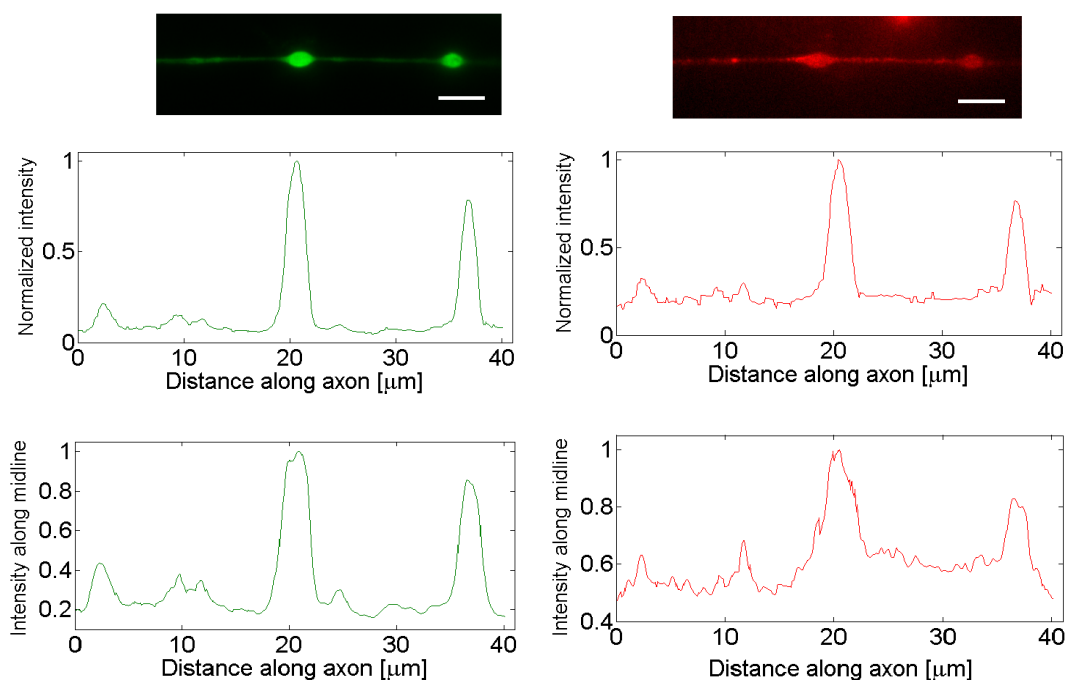


FIGURE 2.23: A Noco-beaded axon stained for α -tubulin (Left, green) and f-actin (Right, red). The upper plots show integrated intensity across the thickness of the axon, at every point along its length. The lower plots show intensity along a line at the midsection of the axon. The intensity values are normalized with respect to the maximum intensity value in each case. Scale bars : $5 \mu m$

All Noco-beaded axons stained for tubulin or NF or Calcein show prominent peaks in the intensity at the sites of beading against a very low base-value of intensity coming from the thin segments connecting the beads. This behaviour is seen

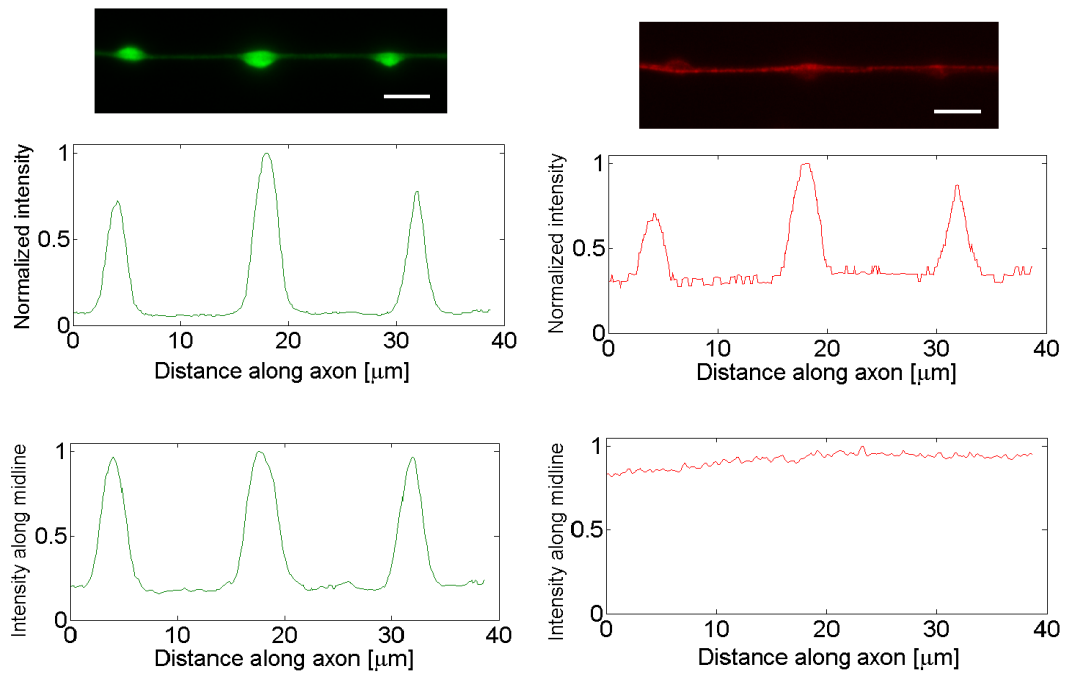


FIGURE 2.24: A Noco-beaded axon stained for α -tubulin (Left, green) and f-actin (Right, red). The upper plots show integrated intensity across the thickness of the axon, at every point along its length. The lower plots show intensity along a line at the midsection of the axon. The intensity values are normalized with respect to the maximum intensity value in each case. Scale bars : $5 \mu m$

both in the integrated and the line profiles. However, the same may not hold true with f-actin distribution as seen in fig. 2.24 (Right) where the line profile is almost uniform irrespective of the beaded geometry. This is again suggestive of an inhomogeneous distribution of f-actin in axons. Also note that although NFs seem to accumulate at the beading sites, the corresponding intensity peaks in the line profiles looks rough unlike those for tubulin and Calcein staining. This might be so due to the filamentous nature of NFs remains unaffected after Noco treatment but it obviously affects tubulin mass, converting it from the mostly polymerized to the mostly tubulin-subunit state.

2.3 Summary and conclusions

Axonal beading and retraction have been commonly observed as a feature of many neuro-degenerative conditions *in vivo*. In many of the cases, a disturbed cytoskeletal organization may be the cause. We have investigated these shape deformations by

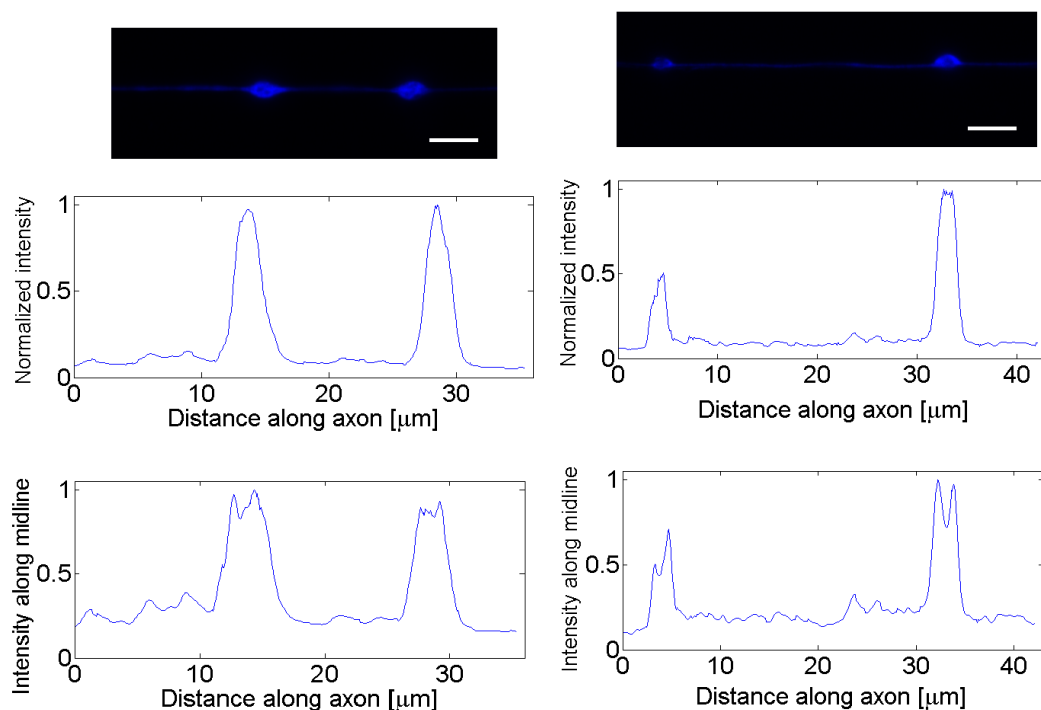


FIGURE 2.25: Two Nocodazole-beaded axons (left and right) stained for neurofilaments. The upper plots show integrated intensity across the thickness of the axon, at every point along its length. The lower plots show intensity along a line at the midsection of the axon. The intensity values are normalized with respect to the maximum intensity value in each case. Scale bars : $5 \mu m$

pharmacologically perturbing the cytoskeleton of axons. In the following, first the results of our investigation on Nocodazole induced beading of axons are summarized. Although this effect has been known for many years, the physical mechanism and the dynamics of the shape transformation have not been studied in detail.

1. The time scale of axonal beading depends upon the concentration and time of exposure to Noco. The time taken for an axon to undergo beading is independent of the thickness (or radius) of the axon. The distance between consecutive beads is broadly distributed for a population of axons and it is independent of the axon's initial radius.
2. Comparison with osmotic shock induced pearling of axons: Earlier work on axonal pearling induced by applying hypo-osmotic shock shows highly periodic swellings with the wavelength scaling linearly with the initial radius of axons. Noco beading does not show any clear periodicity or correlation with the initial radius. However, we show that for mild osmotic shocks, the pearling shapes may

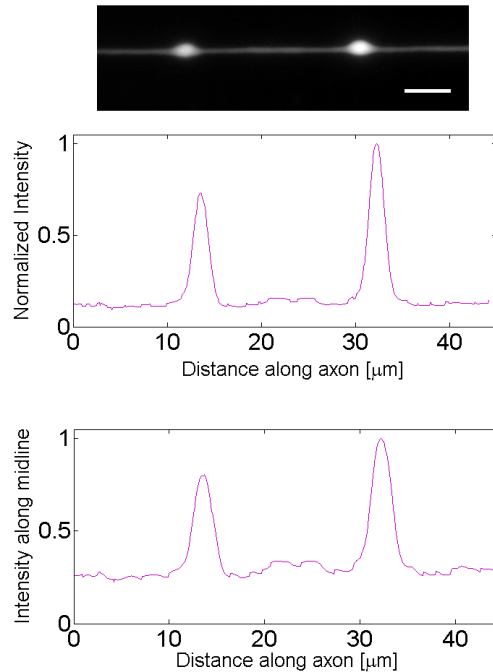


FIGURE 2.26: A Noco-beaded axon stained with Calcein. The upper plot shows integrated intensity across the thickness of the axon, at every point along its length. The lower plot shows intensity along a line at the midsection of the axon. The intensity values are normalized with respect to the maximum intensity value in each case. Scale bars : $5 \mu m$

not be periodic. This could be because at small increments in membrane tension due to a mild osmotic shock, spatial heterogeneities in axon become significant. In osmotic pearling, the volume increases before beading sets in, indicating axonal swelling whereas there is no significant axonal swelling observed prior to Noco-beading. In the case of osmotic pearling, an axon recovers the cylindrical shape by going back to its initial volume whereas Noco-beading is irreversible. Osmotic pearling develops simultaneously along the length of an axon whereas Noco beading starts from the growth cone (GC). This may be because mostly labile MTs are concentrated in that region compared to the proximal shaft where both stable and labile MTs are found. These comparisons show that Noco beading is unlikely to be caused by a drastic increase in membrane tension due to swelling, like in the case of osmotic shock induced pearling of axons.

However, there is a possibility that Noco-beading is a shape instability occurring due to axon's rest membrane tension if the Noco induced MT depolymerization results in a drastic reduction of the compression modulus of the cytoskeleton gel. The reduced modulus brings down the value of the critical membrane tension

required for the cylindrical geometry to become unstable to beaded shape, thus the small membrane tension of axons (detailed measurements in Chapter 4) may be sufficient to cause beading.

3. The mechanism of traffic jam of the intra-axonal transport as the cause of beading was proposed due to the presence of organelles in beads, as seen in electron micrographs of the beaded axons [7] and because of breaks in MT seen in experiments mimicking traumatic stretch injury. [6]. However, our observations of live axons show that the internal transport continued in axons which are about to bead or already beaded. The beads can also translocate without fresh beading occurring at the earlier location, contradicting the traffic jam hypothesis. It may be seen in some cases that after the bead-formation begins, the transport at the beading sites gets affected; but the beading sites do not show any a priori anomaly in the transport.

4. Local drug application experiments show that exposure of a small segment of the axonal shaft to Noco cannot induce beading at that spot. This could be so because of the location dependent organization of labile and stable MTs in axons. Another reason could be the length distribution of MTs in axons. If the average length of axonal MTs is larger than the span of drug exposure through local application, then again beading may not develop. Thus it is essential to expose the whole axon to Noco in order to make it acquire the beaded geometry, suggesting that beading requires a global disruption of MT structure.

5. The experiment to verify active role of molecular motors mediated contractility in general, by the method of ATP depletion remains inconclusive. This is because Noco can not bring about MT disruption in ATP depleted conditions. In the next chapter (Chapter 3) we present a very different way of inducing axonal beading where the ATP depletion test was carried out to probe involvement of the active processes in this shape transformation.

6. We show that f-actin and myosin II are not the essential factors to bring about Noco-beading. Moreover, the disruption of f-actin accelerates the beading process.

7. Fluorescent labelling of the cytoskeletal filaments reveals interesting structural features with respect to Noco-beading. It shows that the beads are accumulation

sites of tubulin and neurofilaments. It is intuitively plausible that as Noco treatment changes the state of the tubulin contents of axons from mostly filamentous to mostly subunit form and therefore as an axon undergoes beading, the tubulin mass along with the cytosol, is expected to get accumulated in the beaded regions. However, prominent accumulation of NFs in the beaded region opens a possibility of an unexplored mechanism of beading because NFs should retain their filamentous form as Noco is not known to have disruptive effects on NFs. One possible candidate for the mechanism may be originating from relaxation of a pre-stress stored in the MT-NF cytoskeleton. The relaxation could get triggered due to Noco mediated disruption of MTs. The existence of the pre-stress and its relaxation leading to beading are examined in the next chapter (Chapter 3).

Thus, Noco-beading could be effecting from a shape instability triggered by a possible reduction in the bulk compression modulus of axonal cytoskeleton in the presence of a small but finite membrane tension OR it could be due to a built up of active contractile stress on the cytoskeleton or passive relaxation of a pre-stress stored in the cytoskeleton. Either of these may lead to a local condensation of the cytoskeletal elements, nucleating in the bead formation. In order to probe the existence of active stress build up or pre-stress in the cytoskeleton, we subjected the axons to a local discontinuity in the cytoskeleton, induced in a completely different way, using the technique of laser ablation as discussed in the next chapter. There we see similar shape transformations like beading and retraction *of the cytoskeleton alone in the presence of an intact membrane tube*. Findings of the laser ablation experiments demand revisiting the above hypotheses in the last chapter (Chapter 5).

2.4 Axonal retraction induced by Latrunculin-A

Here we present preliminary work on the retraction of axons induced by long time exposure to Latrunculin-A (Lat-A), a drug that disrupts f-actin in cells. This effect of Lat-A on axons has not been reported so far. In fact, the drug has been known to inhibit retraction of axons because it brings about disruption of f-actin [15]. However, we see that axons grown on uncoated glass surface and especially

those having free growth cones (GCs) i.e. GCs which haven't formed connections with other cells or axons in the culture, tend to get retracted when exposed to about $1\ \mu\text{M}$ for several minutes as shown in fig. 2.27.

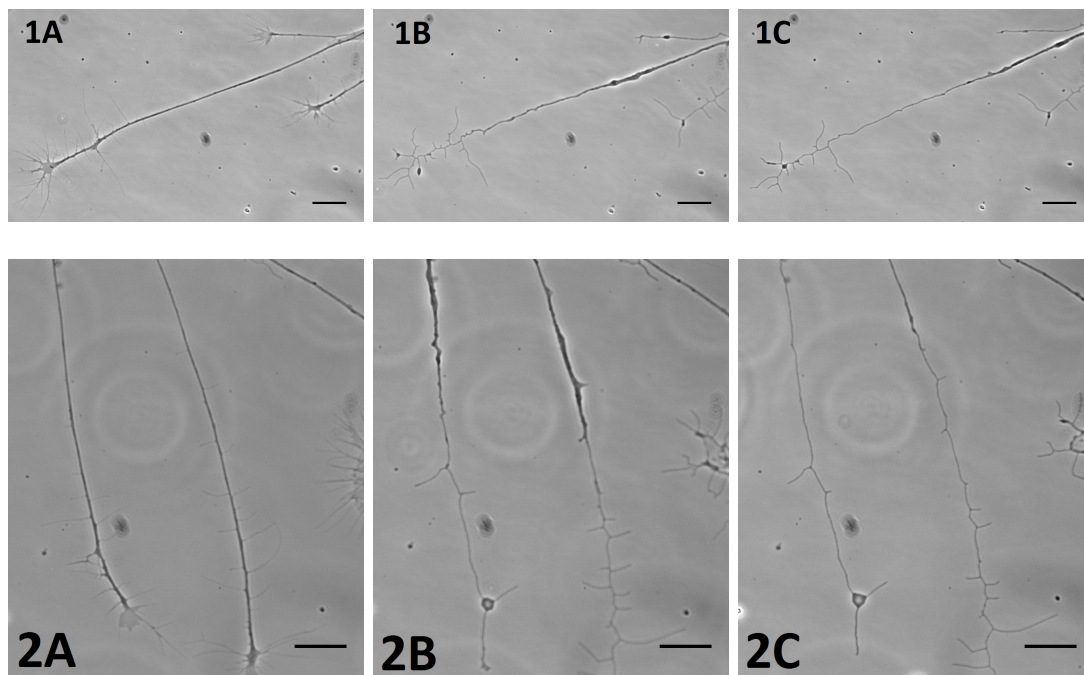


FIGURE 2.27: Axons (A) before, (B) 50 minutes after and (C) 90 minutes after exposure to $1\ \mu\text{M}$ Lat-A. Scale bars : $20\ \mu\text{m}$

2.4.1 Experiments and Results

Retraction induced by Lat-A always begins from the GC end of the axons. It first destroys the finger-like structure of the GCs, then begins with squeezing out the material from the shaft next to the GC and transferring it into the proximal side. Thus the proximal region becomes thicker, leaving behind a thin trailing membrane tube on the distal side. The proximal shaft may show buckling. In most of the cases, the retraction takes place with a distinct retraction front which has a bulged or beaded shape. This behaviour can be seen in the representative movie *Lat-A-retraction* where two axons with free GCs, one in upper right corner and other in the left part of the frame undergo retraction. The time in minute:second after exposure to Lat-A is indicated in the top-left corner. The buckling behavior of a Lat-A treated, retracting axon can be seen in fig. 2.28. The time after addition of Lat-A is indicated in the upper left corner in minute:second.

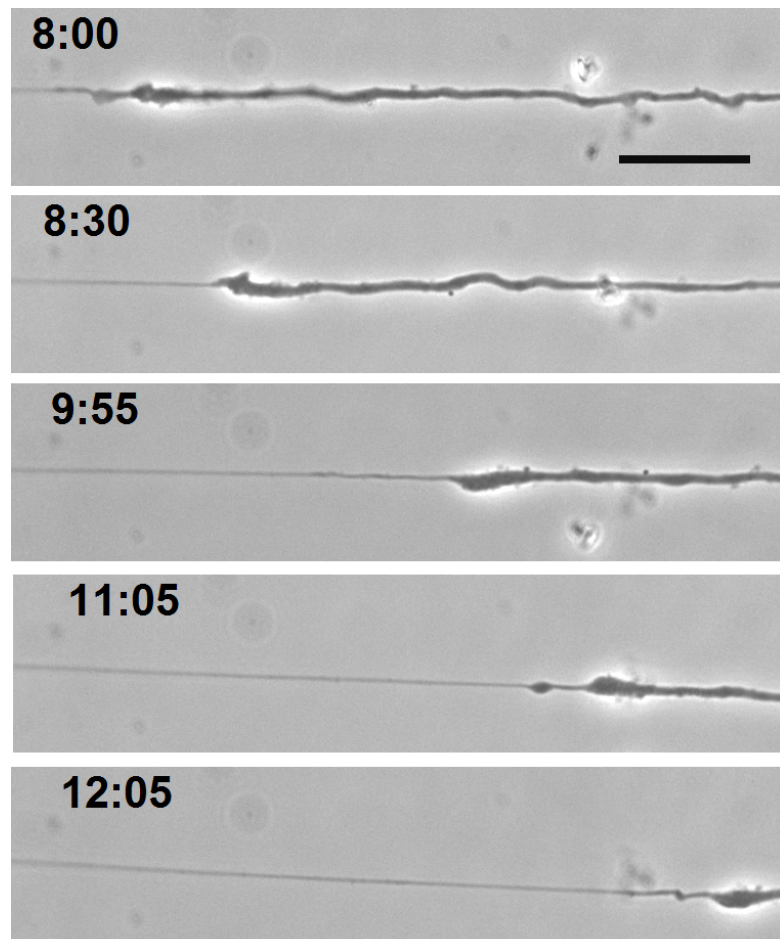


FIGURE 2.28: Retraction of an axon after Lat-A treatment. Buckling can be seen in the first and second panel. Scale bar: $20\ \mu\text{m}$

All the experiments listed below were done at $36 \pm 1^\circ\text{C}$, using an on-stage (the microscope stage) brass casing through which warm water was continuously circulated. The temperature at the sample was calibrated using a platinum resistor.

Out of 75 axons with free GCs, 53 showed retraction within 90 min. of exposure to $1\ \mu\text{M}$ Lat-A. We see that pre-treatment with Blebbistatin at $20\ \mu\text{M}$ for 20 min. at 37°C does not inhibit the retraction induced by Lat-A.

The retraction is sometimes accompanied by a few bead formations as shown in fig. 2.29. These beads often merge with the retraction front and therefore disappear unlike the case of Noco-beading where the beaded shape prevails for a long time.

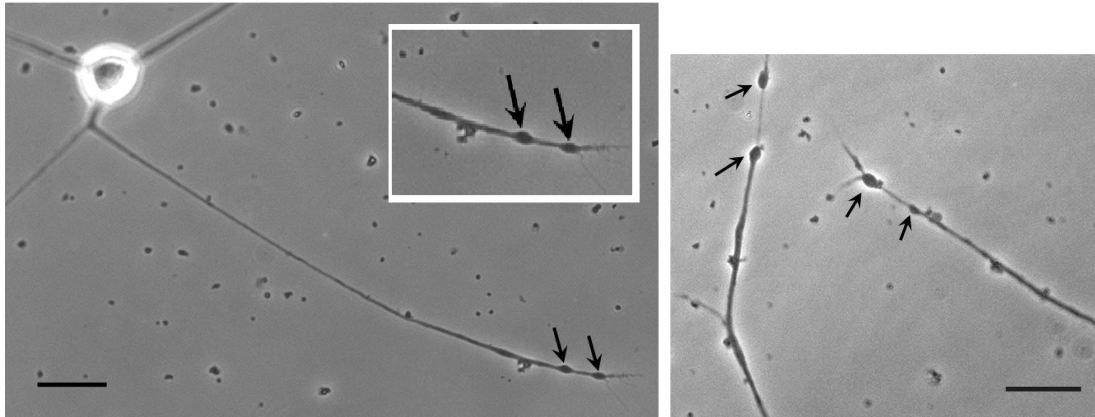


FIGURE 2.29: Retracting axons with bead formations (shown by black arrows) after Lat-A treatment. The inset on left shows a magnified view of the bead formations. Scale bars : $20\ \mu\text{m}$

Fluorescent labelling

In order to understand the effect of the Lat-A induced retraction on the cytoskeletal arrangement, we fluorescently labelled the cytoskeletal elements in partially retracted axons using the procedure described in the Methods section. Fig. 2.30 shows axons labelled for tubulin and f-actin whereas fig. 2.31 shows axons labelled for f-actin and neuro-filaments.

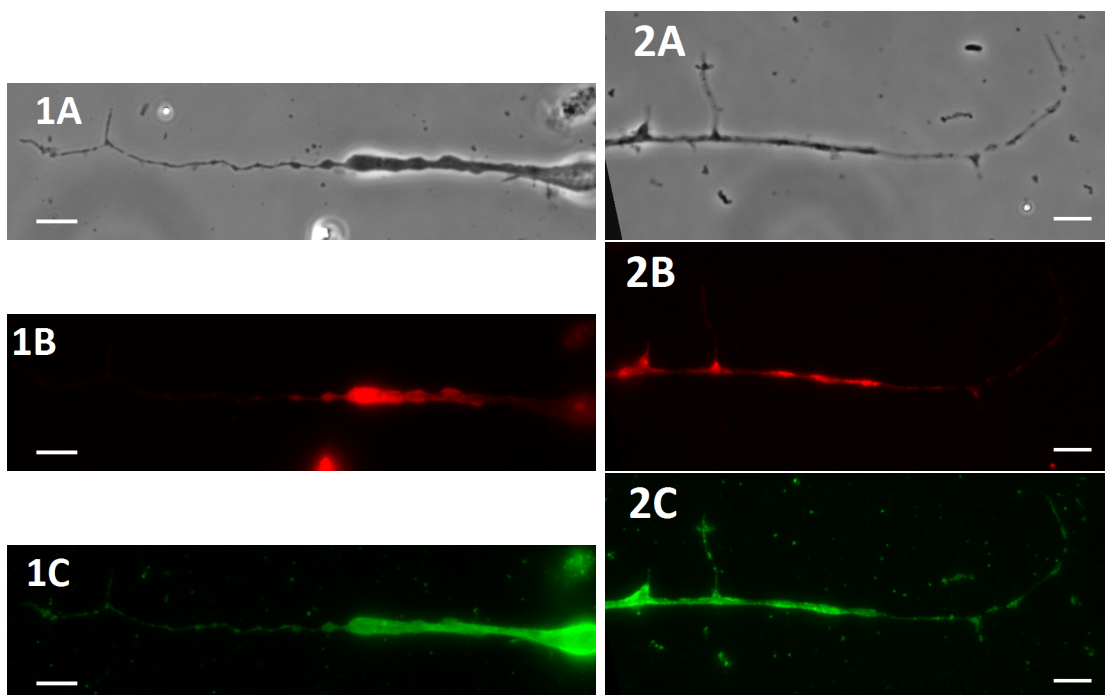


FIGURE 2.30: Partially retracted axons after Lat-A treatment, fixed and permeabilized. (A) Phase contrast image (B) fluorescently labelled f-actin (C) and fluorescently labelled tubulin. Scale bars : $5\ \mu\text{m}$

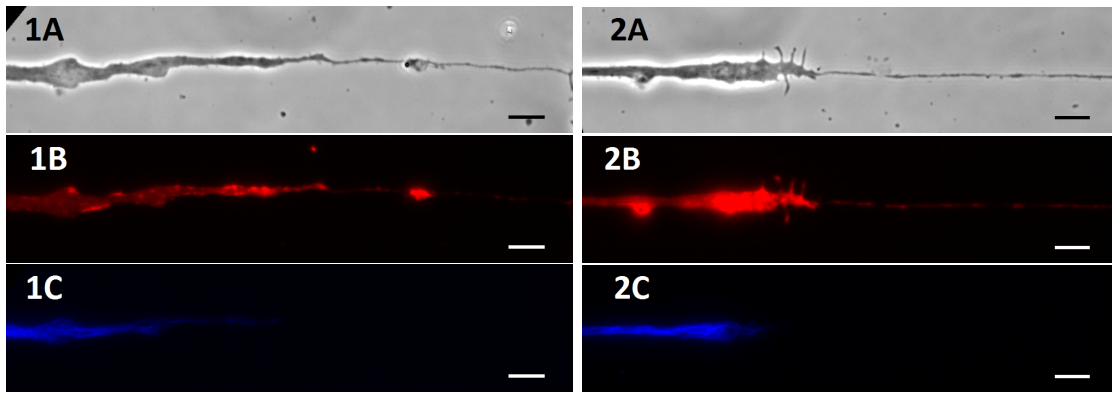


FIGURE 2.31: Partially retracted axons after Lat-A treatment, fixed and permeabilized. (A) Phase contrast image (B) fluorescently labelled f-actin (C) and fluorescently labelled neurofilaments. Scale bars : $5 \mu m$

These figures show that

- (i) A considerable amount of f-actin remains intact in the axonal shaft even after several minutes of lat-A treatment.
- (ii) Traces of f-actin and tubulin can be seen in the thin trailing tube left behind after retraction while neurofilaments get completely swept into the thicker region, without any traces left in the trailing part.

Retraction speed

In the cases where there is a clear retraction front, one can track its position and plot the retracted distance measured from the initial position versus time after addition of Lat-A to the cell culture medium as shown in fig. 2.32A. Each color represents a different retracting axon. It can be seen that axons begin to retract at a wide range of Lat-A exposure times. The jump at about 80 min. in the plot with green circles is due to a sudden fast retraction event.

The same plots with a shifted time are shown in fig. 2.32B for making the comparison of retraction speeds easier.

2.4.2 Remarks

As phalloidin (the labelling component of the dye) binds only f-actin, the actin fluorescence images indicate that Lat-A treatment does not depolymerize most

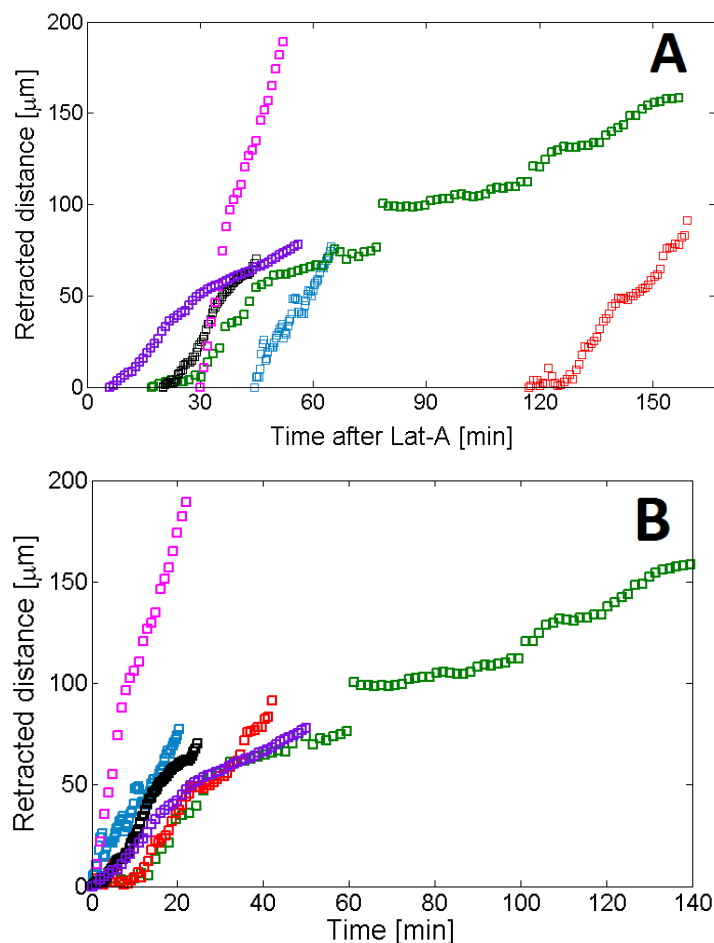


FIGURE 2.32: Retraction of axons after Lat-A treatment plotted as a function of (A) time elapsed after Lat-A addition (B) relative time with respect to the time at which retraction began

of the f-actin contents of proximal part of axons. Thus, the observed retraction is probably triggered only due to f-actin disruption in the distal part and in the GC. This claim is further supported by the initial location and the direction of retraction. It is known that f-actin structure is most dynamic in the GC and hence the GC region is the first to get affected by Lat-A. However, the fact that such a differential disruption of the cytoskeleton can lead to retraction of the whole axon is suggestive of a state of force balance between the elements of axon's cytoskeletal organization and their boundary conditions. The next chapter discusses the scenario where these boundary conditions are locally changed using laser ablation. In Chapter 5 we revisit these arguments and hypotheses, aided with a better understanding of axonal shape transformations under different conditions.

Bibliography

- [1] Pablo A. Fernandez. *Mechanics of living cells: nonlinear viscosity of single fibroblasts and shape instabilities in axons*. PhD thesis, Bayreuth University, Germany, Buenos Aires, Argentina, November 2006.
- [2] Pramod A. Pullarkat, Paul Dommersnes, Pablo Fernández, Jean-Fran çois Joanny, and Albrecht Ott. Osmotically driven shape transformations in axons. *Phys. Rev. Lett.*, 96:048104, Feb 2006. doi: 10.1103/PhysRevLett.96.048104. URL <http://link.aps.org/doi/10.1103/PhysRevLett.96.048104>.
- [3] Frank Solomon and Margaret Magendantz. Cytochalasin separates microtubule disassembly from loss of asymmetric morphology. *J Cell Biol.*, 89(1): 157–161, Apr 1981.
- [4] A D Bershadsky and Gelfand V I. Atp-dependent regulation of cytoplasmic microtubule disassembly. *Proc Natl Acad Sci U S A.*, 78(6):3610–3613, Jun 1981.
- [5] Sydney Ochs, Rahmna Pourmand, Kenan Si, and Richard N. Friedman. Stretch of mammalian nerve in vitro: Effect on compound action potentials. *Journal of the Peripheral Nervous System*, 5, 2000.
- [6] Min D. Tang-Schomer, Victoria E. Johnson, Peter W. Baas, William Stewart, and Douglas H. Smith. Partial interruption of axonal transport due to microtubule breakage accounts for the formation of periodic varicosities after traumatic axonal injury. *Experimental Neurology*, 233 (1):364 – 372, 2012. ISSN 0014-4886. doi: <http://dx.doi.org/10.1016/>

- j.expneurol.2011.10.030. URL <http://www.sciencedirect.com/science/article/pii/S001448861100402X>. Special Issue: Stress and neurological disease.
- [7] Gorazd B. Stokin, Concepcin Lillo, Toms L. Falzone, Richard G. Brusch, Edward Rockenstein, Stephanie L. Mount, Rema Raman, Peter Davies, Eliezer Masliah, David S. Williams, and Lawrence S. B. Goldstein. Axonopathy and transport deficits early in the pathogenesis of alzheimer's disease. *Science*, 307(5713):1282–1288, 2005. doi: 10.1126/science.1105681. URL <http://www.sciencemag.org/content/307/5713/1282.abstract>.
- [8] FJ Ahmad, TP Pienkowski, and PW Baas. Regional differences in microtubule dynamics in the axon. *The Journal of Neuroscience*, 13(2):856–866, 1993. URL <http://www.jneurosci.org/content/13/2/856.abstract>.
- [9] Ben Fabry, Geoffrey N. Maksym, James P. Butler, Michael Glogauer, Daniel Navajas, and Jeffrey J. Fredberg. Scaling the microrheology of living cells. *Phys. Rev. Lett.*, 87:148102, Sep 2001. doi: 10.1103/PhysRevLett.87.148102. URL <http://link.aps.org/doi/10.1103/PhysRevLett.87.148102>.
- [10] Devrim Kilinc, Gianluca Gallo, and Kenneth A. Barbee. Mechanically-induced membrane poration causes axonal beading and localized cytoskeletal damage. *Experimental Neurology*, 212(2):422 – 430, 2008. ISSN 0014-4886. doi: <http://dx.doi.org/10.1016/j.expneurol.2008.04.025>. URL <http://www.sciencedirect.com/science/article/pii/S001448860800174X>.
- [11] P. C. Bridgman. Myosin va movements in normal and dilute-lethal axons provide support for a dual filament motor complex. *JCB*, 146(5):1045–1060, Sept 1999.
- [12] Dennis Bray and Mary Bartlett ZBunge. Serial analysis of microtubules in cultured rat sensory axons. *Journal of Neurocytology*, 10:589–605, January 1981.
- [13] Wenquian Yu and Peter W. Baas. Changes in microtubule number and length during axon differentiation. *The Journal of Neuroscience*, 14:2818–2829, month 1994.

-
- [14] Barbara A. Danowski. Fibroblast contractility and actin organization are stimulated by microtubule inhibitors. *J Cell Sci*, 93:255–266, June 1989.
- [15] Fridoon J Ahmad, Jessica Hughey, Torsten Wittmann, Anthony Hyman, Marion Greaser, and Peter W. Baas. Motor proteins regulate force interactions between microtubules and microfilaments in the axon. *Nat Cell Biol*, 2:276–280, May 2000.

Chapter 3

Shape dynamics in Laser-Transected Axons

3.1 Motivation

From the results presented so far, it is clear that the nocodazole-beading is not a shape instability arising from a rapidly increasing membrane tension like that in the case of osmotic shock induced pearling of axons. We have also shown that depolymerization of f-actin using Latrunculin-A (Lat-A) or inhibition of myosin-II using Blebbistatin does not inhibit the beading process. In fact, de-polymerization of actin enhances the percentage of beading in nocodazole (Noco) treated axons. Thus, acto-myosin contractility is also ruled out as a possible cause of the beading. Live imaging of axons reveals that the internal transport continues to take place even after bead-formation, thus ruling out traffic jam as the cause of beading.

It is important to note that beading is not a deformation of the membrane alone. Fluorescent immunolabelling of beaded axons shows that not only tubulin but also neurofilaments (NFs) get accumulated in the beaded region. Given that an increase in membrane tension and acto-myosin contractility are not responsible here to bring about such an irreversible rearrangement of the NFs, it is natural to suspect that the cause might be a pre-stress stored in the MT and NF cytoskeleton itself. It is known that NFs are closely associated with the MTs in axons [1]. Depolymerization of the latter by the action of Noco may release stresses in the

former, thus causing the observed reorganization.

In order to validate this hypothesis, it is essential to know whether the relaxation of a pre-stress in the axonal cytoskeleton could give rise to shape transformation like beading or retraction. Work by S. Kumar *et al.* [2] has shown that when an actin stress fibre in a spread endothelial cell is cut using a 100 femtosecond (fs) laser, the fibre retracts like a visco-elastic object on both sides of the cut (fig. 3.1). This implies that cytoskeleton filaments in a cell are under a pre-stress and may tend to relax this stress by retraction when there is some discontinuity introduced in the structure.

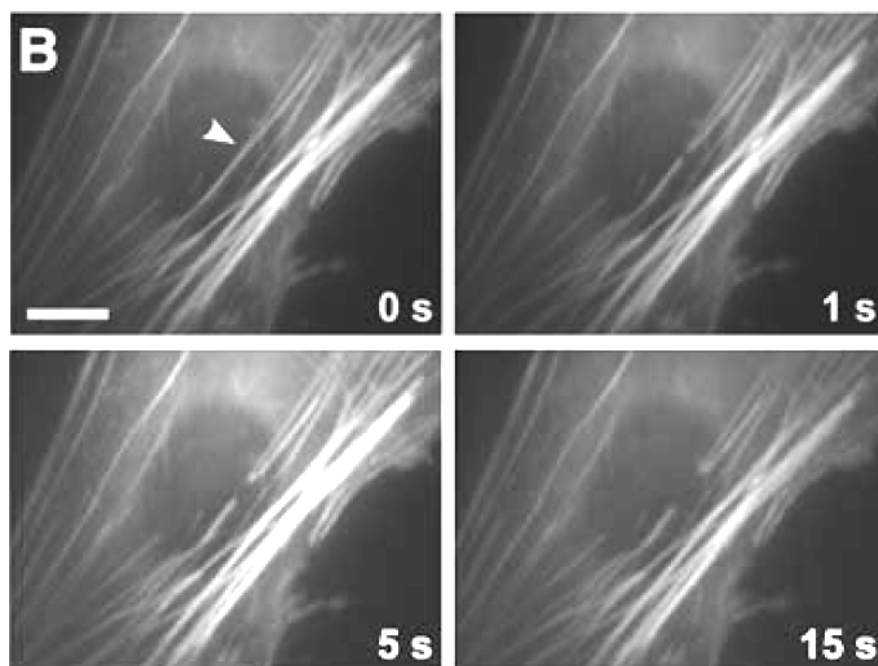


FIGURE 3.1: Laser irradiation of a stress fiber bundle (Arrowhead, laser position. Bar:= $10\mu\text{m}$) resulting in retraction of the bundle. Taken from [2]

In the same light, we studied response of axons to laser cutting, under different biochemical conditions. It was seen that when an axon is cut, it snaps (i.e. retracts very fast) on both sides of the cut. This behaviour was expected as it is well known that in normal conditions, axons are under rest tension [3], [4] and the cut provides a way of relaxing this tension. In addition, there were responses like beading, buckling and winding of the cut shaft which are not well studied so far. Interestingly, we saw that sometimes the laser cuts a axon only partially, leaving the membrane tube intact but creating a discontinuity in the cytoskeleton, leading to a long range retraction of the cytoskeleton alone. These findings contribute to a

better understanding of the nature of the cytoskeletal structure and force balancing in axons and their role in maintaining the shape and stability of axons.

3.2 Previous work on axon transections

Neurons are the basic units of the nervous system, designed to carry electrical and chemical signals over long distances in an organism. Their inter-connections as well as connections with other tissues/cells are very important to the sensory and response abilities. It is known that neurons in the Central Nervous System (CNS) cannot proliferate. Thus neuronal integrity and ability to regenerate axons after an injury have been the topics of great interest. For many decades axonal transection or axotomy experiments have been carried out where axons are mechanically cut using a sharp tip and observed over periods of hours to days in order to study axonal regeneration and target finding [5]. It was shown that depending upon the type and age of a neuron, either the cell dies or survives and may regenerate after the axotomy. Along with the biochemical and signalling studies there has been an interesting work on axonal shape change after axotomy [6]. Here, a possible connection between reorganization of the axonal cytoskeleton, in particular Neurofilaments and the resultant morphological changes in the transected axon was probed. More recently, a relationship between re-organization of microtubule polarities and possibility of growth cone formation from the freshly cut tips of a transected axon was demonstrated [7]. In the last decade, the well established technique of laser ablation was employed for transecting axons in a much cleaner and more precise way [8]. It was shown by Yanik et al. that axons *inside* live *C. elegans* can be transected using femto-second pulse lasers, with negligible mechanical perturbation to the surrounding tissue and these axons can functionally regenerate within 24 hours [9]. They reported retraction of both of the cut ends of an axon immediately after a transection. The technique was then onwards extensively used by many research groups to perform axotomy, mainly to study regeneration of axons both in vivo [10] [11] and in vitro [12], [13]. Recently there has been considerable effort in order to measure the tension released during laser axotomy by attaching an optically trapped bead to the axon to be

transected where it is reported that the tension release consists of a fast phase which lasts for a few seconds and a slow phase which may last up to few minutes [14]. In all these studies, the interesting shape dynamics of transected axons got a secondary or no attention. Through a private communication with Dr. Sandhya Kaushika (Dept. of Biological Sciences, TIFR, Mumbai) we learnt that axons in live *C. elegans* sometimes show beaded geometry after laser transection. This observation was highly significant for this thesis work because one expects that a transection should lead to releasing the pre-stress or tension in the axon and yet it gives rise to a beaded geometry. This is contrary to the scenario of rapid rise in the membrane tension causing axonal pearling the cases of osmotic shock [15] and stretch injury [16]. Thus, we conducted experiments in order to investigate the shape dynamics of laser transected axons, the components involved in these shape changes and the underlying mechanisms. Additionally, we could also study the interesting cases where the axonal membrane remains intact after ablation or gets resealed and adhered to the substrate, leaving a discontinuity in the cytoskeleton alone.

Before discussing the experiments and results it is important to understand the consequences of exposing biological tissue to high power lasers in different regimes of the power density and exposure times.

3.3 Laser-Tissue Interaction

The interaction of a laser with the sample-tissue depending upon the power density (power per unit area) deposited by the laser on the tissue and the exposure time (or pulse duration) can be categorized as follows [8] (fig. 3.2) :

- Photochemical interaction
- Thermal interaction
- Photoablation
- Plasma-induced ablation

- Photodisruption

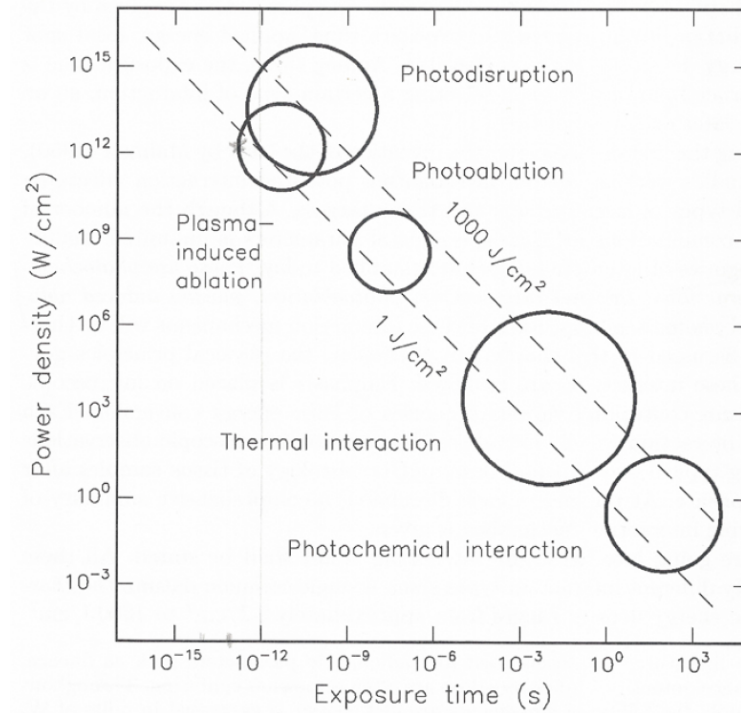


FIGURE 3.2: Map of laser-tissue interactions. The circles give only a rough estimation of the associated laser parameters. Taken from [8].

Photochemical interaction

We know from the famous example of photosynthesis that light can induce chemical effects and reactions within macromolecules and tissues. The photochemical interactions take place at very low power densities, about 1 W cm^{-2} and at long exposure times from seconds to continuous wave. This type of interaction does not give rise to any macroscopic changes in the tissue.

Thermal interaction

The laser can cause local heating in the tissue at wide ranges of the power density (10 to 10^6 W cm^{-2}) and pulse duration ($1 \mu\text{s}$ to 1 min.). The heating may lead to various effects like coagulation, vaporization, melting or thermal decomposition of the tissue.

Photoablation

Between power densities of 10^7 to $10^{10} \text{ W cm}^{-2}$ and pulse durations of 10 to 100 ns

the laser can cause direct breaking of molecular bonds (ablation) by high energy UV photons. It can be applied to cleanly remove a part of a tissue while performing surgeries. The interaction may also lead to audible effects and visible fluorescence.

Plasma induced ablation

High power densities (10^{11} to 10^{13} Wcm^{-2}) at short pulse durations (about 100 *fs* to 500 *ps*) lead to plasma formation by ionization in the tissue. In the case of femto-second or pico-second (ps) lasers, the plasma formation takes place by multi-photon ionization. A nano-second laser can also lead to plasma formation at high enough power densities through the process of thermionic emission. The plasma has orders of magnitude higher absorption coefficient than the tissue. Thus the plasma behaves like a trap for the succeeding laser photons, constituting a *plasma shield* for the rest of the tissue. This effect restricts the plasma formation to a limited volume in the tissue. The plasma induced ablation results in clean cuts with very small thermal or mechanical damage.

Photodisruption

At even higher power densities the plasma formation is accompanied with strong secondary effects which are mechanical in nature like shock wave generation and cavitation bubble expansion. This is because the mechanical effects scale linearly with the absorbed energy. Unlike the plasma induced ablation, the photodisruption causes a rupture in the tissue by mechanical forces which propagate through larger volume in the tissue, thus compromising on the compactness of the damage zone. In the case of nano-second lasers the threshold power density for plasma formation is higher compared to pico-second or femto-second lasers. Therefore, plasma induced ablation with nano-second lasers is often accompanied with shock wave formation.

For our experiments we have used a nano-second laser instead of the more precise femto-second lasers. It has been shown by Rao et al. [11] that nano-second lasers which are cheaper and simpler to operate can be used instead of femto-second lasers for *in vivo* (inside *C. elegans*) axotomy without significantly increasing the

collateral damage. In the present work, we have used ns laser on primary neuronal culture surrounded by a medium with water-like viscosity. In order to prove that the effects we observed are real responses of the axons to the cut and aren't arising from photo-disruptive effects of the laser, we performed two tests:

- Nano-second laser axotomy of axons which are fixed using aldehyde treatment and cold ethanol incubation
- Mechanical transection of live axons

As described in detail in the Results section, the first test proves that the damage created by the nano-second laser is much smaller and short-lived compared to the response of the live neurons to the axotomy. Whereas the latter test led to similar effects as those produced by laser transection of live axons, validating the results of our experiments.

3.4 Experimental Set-up

Laser ablation: A detailed schematic diagram of the set up is shown in fig. 3.3. Laser beam from a Nd:YAG laser (Spitlight 600, Innolas, Munich, Germany) with wavelength $355nm$ (UV) and pulse width $6ns$ is first sent through two plano-convex lenses which act as a beam (diameter) expander, so that the beam fills up the back aperture of the microscope objective lens in order to focus it on a very small region effecting to a high power density required for the ablation. The beam is directed into the back port of an inverted microscope (Olympus iX71) using steering mirrors and reflected by a dichroic mirror (Chroma 532/355 zet532nbdc) into the objective's back aperture. The objective lens serves two purposes, of magnifying the sample (axons) and focusing the laser on the sample in order to perform the cut. We used 100x (oil immersion, N. A. 1.3), 40x (N. A. 0.7) or 20x (N. A. 0.45) UV compatible Olympus objectives according to the magnification requirement. The motorized sample-stage was controllably moved using a joystick to place the sample (a plastic petri dish with a glass coverslip bottom on which axons were grown) in the path of the laser. The laser-transected axons could be

imaged only after a gap of 1 or 2 s after the laser ablation because the focus had to be re-adjusted. Imaging was done using a CCD camera (Optikon PCO.). An infra-red lamp was used in order to keep the neuronal sample at 35 ± 2 °C. The temperature near the cells was calibrated using a tiny Platinum resistor (Pt100).

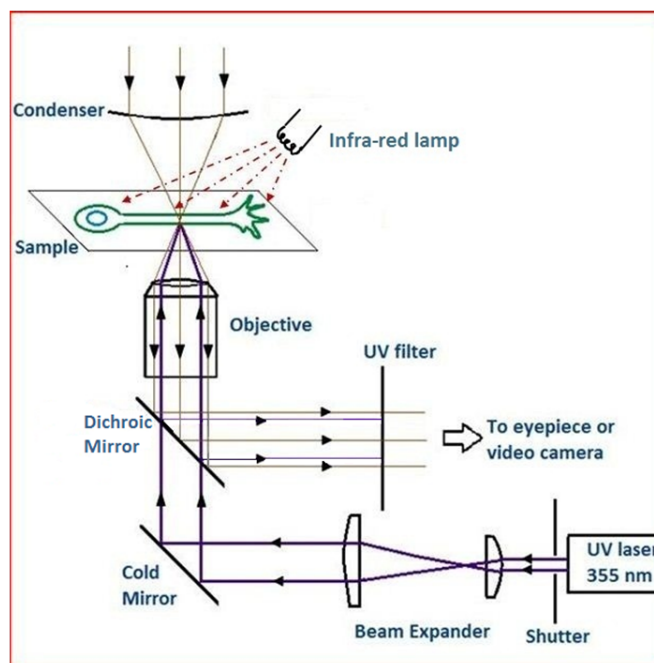


FIGURE 3.3: Schematic diagram of the laser ablation set-up. The sample is maintained at 35 ± 2 °C using an infra red lamp.

Laser power calibration

The laser power collected at the back aperture of the objective was measured using a power meter that could be placed in the objective turret. The value of the average power was 0.05 mW. The power density deposited at the sample due to a single laser pulse through the 100X (N.A. 1.3) objective with transmittance 55 % at 355 nm comes to be 9.6×10^{11} Wcm⁻². The accuracy of the ablation was tested by focussing the laser on a sedimented monolayer of 1 μm size beads, immersed in water, sandwiched between two glass slides. It was observed that a single bead which was surrounded by other beads with their boundaries touching the bead in focus, could be ablated without disturbing the neighbouring beads.

Mechanical transection: Glass micropipettes were pulled from 0.5 mm diameter glass capillary tubes using a Flaming/Brown Micropipette Puller (Model P-97, Sutter Instruments Co.). Pipettes with jagged end, which could make a single fine

scratch on the surface of a plastic petri (seen under a microscope) were chosen for the transection. The sample (a petri dish with a glass bottom on which the neurons were cultured) was placed firm on the motorized stage of a microscope (Zeiss Z1). The sample was maintained at 36 ± 1 °C during the experiment using a custom made brass incubator attached to a hot water circulator (Julabo F27). The pipette was attached to an XYZ micro-manipulator system (XenoWorks Micromanipulator, Sutter Instruments Co.) which is operated using a joystick. Once the fine tip of the pipette was optimally positioned, it was kept fixed, touching the upper surface of the glass cover-slip. A selected axon was moved using the X-Y motorized stage across the position of the micropipette through the position controlling software (AxioVision). This movement resulted in the desired cut.

3.5 Materials and Methods

Cell culture: Axons from chicken embryonic primary neurons were grown as described in Appendix A. Axons with uniform caliber along the length were chosen for the laser cutting experiments. About 30 minutes prior to the all experiments, the viscous growth medium i.e. medium with methocel was replaced with pre-warmed medium having normal water-like viscosity i.e. medium without methocel.

Biochemical treatments:

- Nocodazole: The cells were incubated for 15 minutes prior to the experiment in the medium with $16.67 \mu M$ Nocodazole (Noco) in order to disrupt the microtubule structure. The medium was not changed after this till the end of the experiment.
- Latrunculin-A: The cells were incubated for 30 minutes prior to the experiment in the medium with $1 \mu M$ Latrunculin-A (Lat-A) in order to disrupt the f-actin structure. The medium was not changed after this till the end of the experiment.

- ATP depletion: The cells were incubated for over 45 minutes prior to the experiment in the ATP depletion buffer. The buffer was not changed after this till the end of the experiment.
- Aldehyde mediated fixation: The procedure is as described in the Methods section of Chapter 2.

3.6 Results

3.6.1 Fast Retraction or *Snapping*

As an immediate effect of the laser transection of a axon, the two cut ends snap away from the point of cut as shown in fig. 3.4. We term the initial fast retraction as ‘snapping’. It is sometimes followed by a much slower retraction as will be explained later. The white spot in the second and third panels of the figure is the fracture-mark caused by the laser on the glass surface. This mark acts as the reference point for identifying the point of laser cut.

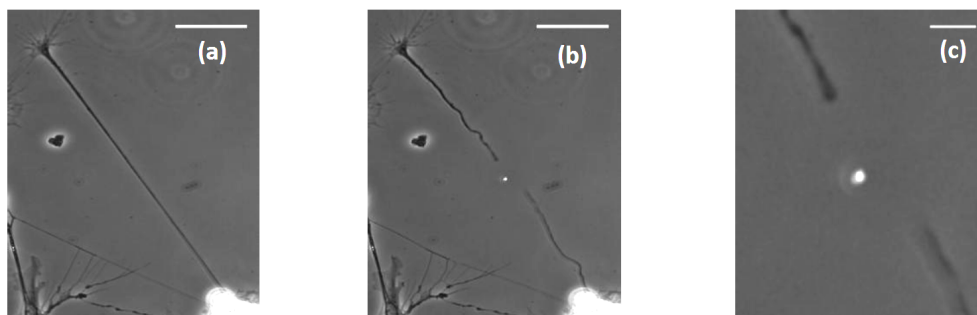


FIGURE 3.4: A control axon (a) before and (b) after a laser cut. Bar: $40\ \mu\text{m}$
(c) shows zoomed in version of (b). Bar: $8\ \mu\text{m}$

In order to verify that the observed snapping is a response of a live axon to the transection and not an undesired effect of the high power UV laser, the same experiment was performed on two sets of axons which were fixed in two different ways viz. aldehyde treatment and cold ethanol ($-20\ ^\circ\text{C}$) incubation. In both cases snapping was inhibited without any exception. Fig. 3.5 shows an example of laser cutting performed on a aldehyde fixed axon where inhibition of snapping can be clearly seen. Out of total 35 fixed axons none showed snapping, probably because

the fixative cross-binds all the protein molecules and thus permanently locks all the tension bearing elements into a configuration just prior to fixing, making that configuration the new ground state. Or the lack of snapping might be simply due to over-strengthening of the axon-substrate adhesions during the process of fixation. But the latter possibility is ruled out by the following test. When a fixed axon is cut at two different locations, the segment between the two cuts can be seen to be lacking any attachment to the substrate. It can be easily displaced by a gentle flow of the surrounding fluid medium as shown in fig. 3.6.

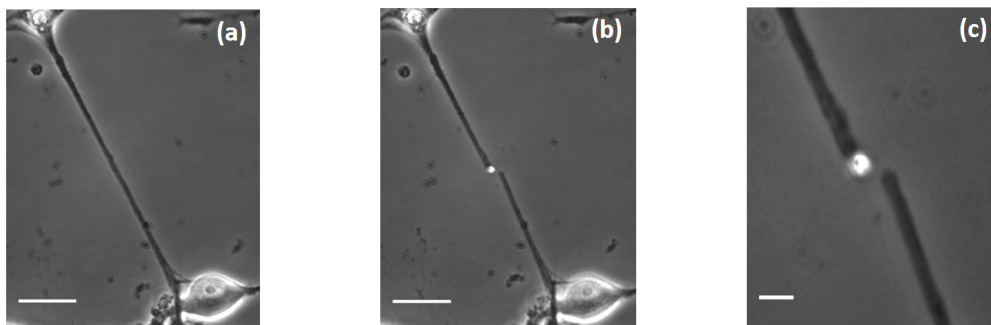


FIGURE 3.5: A fixed axon (a) before and (b) after a laser cut. Bar: $40\ \mu\text{m}$
(c) shows magnified version of (b). Bar: $8\ \mu\text{m}$

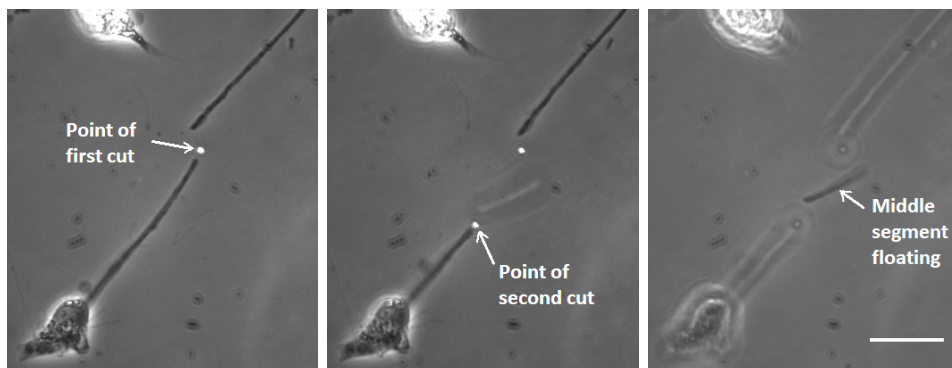


FIGURE 3.6: A fixed axon cut at two places in succession. The segment between the two cuts freely floats in the bulk medium proving that the lack of snapping behaviour is not due to fixative mediated strengthened attachments to the substrate. Bar: $40\ \mu\text{m}$

Snapping length is defined as the distance between either of the two cut tips and the point of laser cut, measured within 3s after the cut. Thus, for every transected axon we measure two values of snapping length. Because of the time lag and buckling of the axonal shaft accompanying the snapping, this length is an overestimation of the actual retracted length. However, the time lag could not be reduced because an axon had to be manually re-focussed after ablation and the

buckling could distort the shaft along Z-direction (out of the plane of focus) which was difficult to measure. We do not see any difference between snapping lengths measured on the distal and proximal sides of axons. For a population of control axons the distribution of snapping lengths is shown in fig. 3.7.

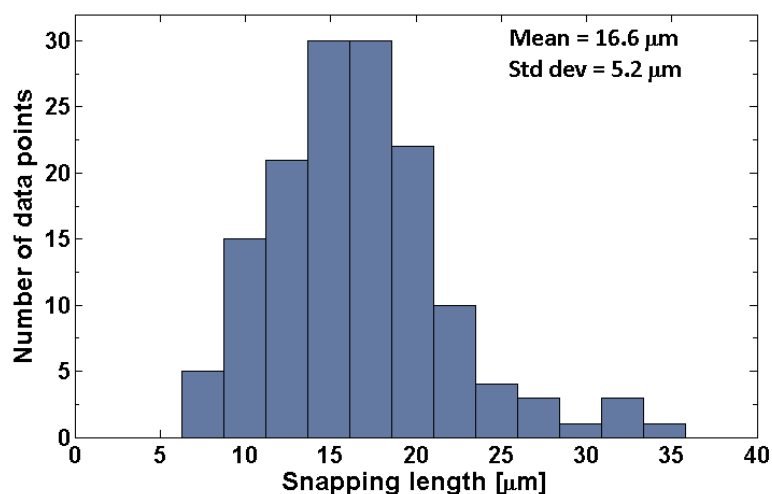


FIGURE 3.7: Snapping length distribution for Control cells. 72 cut axons, 144 data points

Double cut: In the experiments described so far, the far ends of a axon (away from the point of laser cut) are anchored (either at the soma or at the growth cone). Therefore, the snapping behaviour could be expected to change when the boundary conditions are changed. This can be verified by cutting a axon at two places. If the first cut completely releases the rest tension in the axon, the second cut should not show snapping. However, we observe that axons do snap after the second cut by similar lengths as after first cut. Fig.3.8 shows an example of double cuts performed on a control axon.

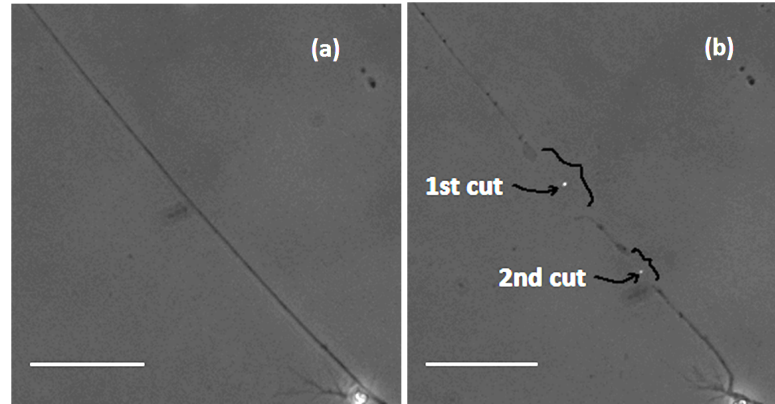


FIGURE 3.8: (a) A control axon before and (b) after a double cut. The black curly brackets show the extent of snapping for each cut. Bar: $40\ \mu\text{m}$

3.6.2 Effect of cytoskeleton perturbations on snapping

In order to determine which intra cellular components give rise to the snapping behavior and whether these components are active or passive, we measured snapping lengths after laser cut performed on axons subjected to,

- (i) Noco treatment, in order to disrupt the microtubules
- (ii) Lat-A treatment, in order to disrupt the f-actin
- (iii) ATP depletion using 2-Deoxy-D-glucose and sodium azide

The mean values of snapping length for each of the above treatments with sample size ‘n’ are shown in Fig. 3.9 and listed in table 3.1.

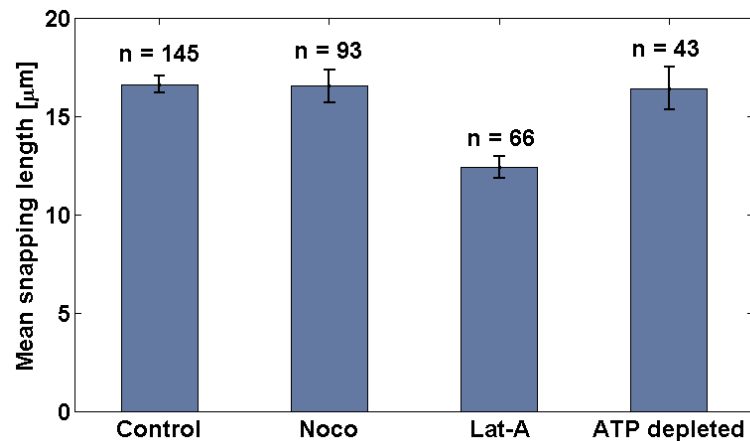


FIGURE 3.9: Comparison of mean snapping lengths of control, Noco-treated, Lat-A treated and ATP depleted axons. The error bars are the standard errors of the mean. ‘n’ is the number of data points for each data set.

The p-values at 5% significance level obtained from Students' t-test with a null hypothesis that the two distributions of snapping lengths for control and the treated axons are independent are presented in table 3.1. Thus, only disruption of f-actin significantly changes the distribution of snapping length of axons, reducing its mean value by about 25% with respect to the control set. It should be once again noted that in the case of axons fixed using cold ethanol or aldehyde treatment no snapping was observed in any of the cutting experiment (sample size = 35 axons).

Treatment	Mean Snapping length [μm]	p-value
Noco	16.52	0.9307
Lat-A	12.39	$1.4020 \times e^{-08}$
ATP depletion	16.41	0.8677

TABLE 3.1: p-values obtained from Student's t-test at 5% significance level for distributions of snapping length of axons with the mentioned drug treatments against that of control axons.

Cytoskeletal breakage within an intact membrane tube: In some cases the laser cuts an axon only partially, i.e. it creates a discontinuity in the cytoskeleton but the plasma membrane tube remains intact. In such cases the cytoskeleton alone may Retract from both sides of the cut, leaving a membrane tube in the middle which has a uniform diameter and is almost devoid of the cytoskeleton as shown in fig. 3.10 and the movie *Partial_cut-intact-membrane-tube* (Please note that all movies which are an integral part of this thesis work and referred to at various places can be found at www.rri.res.in/thesis_Anagha_movies with username: thesis and password: An@rri_th, organized chapter-wise). The tube between the two retracting ends is much thinner compared to the initial diameter of the axon and therefore it is almost invisible. However, the fact that the rest of the axon remains straight after the laser ablation indicates the presence of a tube connecting the two cut ends. The numbers in the upper left corner show real time in minute:second.

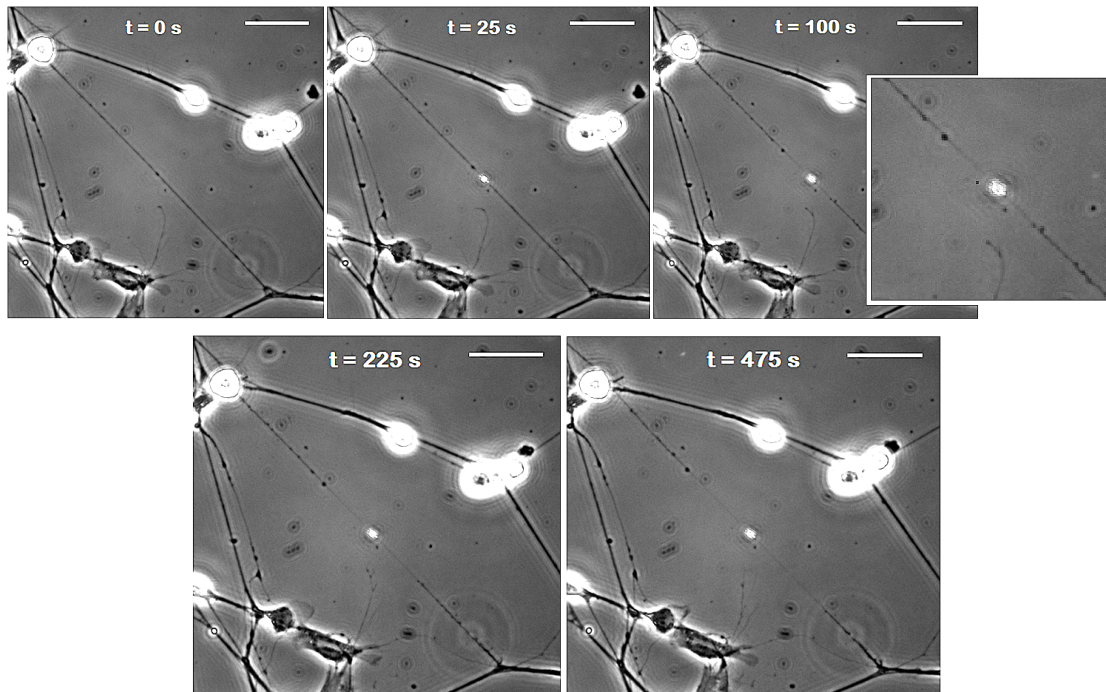


FIGURE 3.10: A time series showing a partial laser cut which creates a discontinuity in the cytoskeleton but leaves the membrane intact. Later, the cytoskeleton starts retracting within a thin membrane tube barely visible in between the two retracting fronts (see the inset). Bar: $40\ \mu\text{m}$

3.6.3 Buckling after laser cut

About 50% of the axons show local or long-range buckling after cut. It is prominently seen in the axons which are not well adhered to the substrate. Fig. 3.11 shows an example of this.

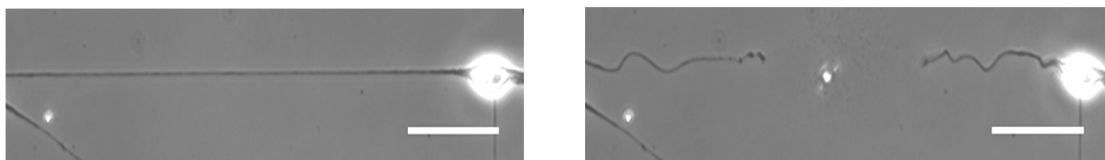


FIGURE 3.11: A control axon before (left) and 15 seconds after (right) a laser cut. Bar : $40\ \mu\text{m}$

3.6.4 Beading after laser cut

Neurites with uniform radius across the length were selected for performing all the laser cut experiments. About 50% of them showed modulation of the shaft radius after laser cut. The modulations may build up to form multiple swellings

along the axon (called as *beading*) as shown in fig. 3.12, fig. 3.13) where beading can be seen on both proximal and distal segments of cut axons and the movie *Beading-after-laser-cut* where the distal shaft of the cut axon develops beading after the laser ablation and snapping. The numbers in the upper right corner of the window show real time in minute:second.

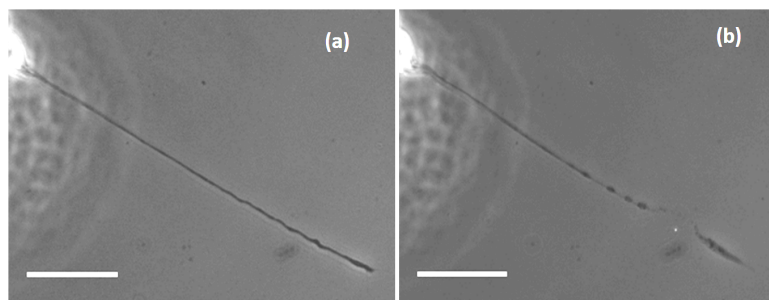


FIGURE 3.12: A control axon before (a) and after (b) laser cut. Bar: $40\ \mu\text{m}$

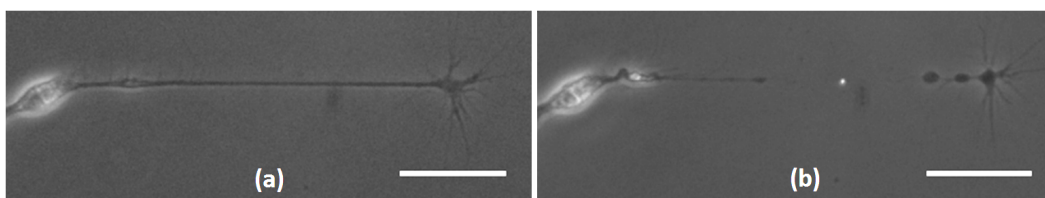


FIGURE 3.13: A control axon before (a) and after (b) laser cut. Bar: $40\ \mu\text{m}$

In some cases bead formation takes place all along the axon (region in field of view) within a couple of seconds after the cut (Fig. 3.14).

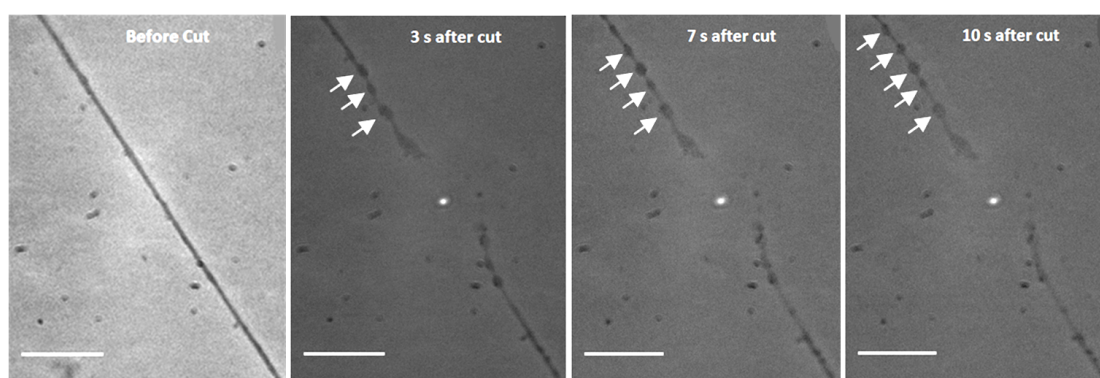


FIGURE 3.14: Time series of fast beading after laser cut. Beading (shown by white arrows) spreads away from the point of cut (small white mark on the surface). Bar: $10\ \mu\text{m}$

In some other cases bead formation begins at the cut tip then progresses towards part of the axon away from the tip as shown in fig. 3.15. More than 70% of the

axons show non-uniform intensity along the length after the cut suggesting that the material gets reorganized inside the axon after the cut.

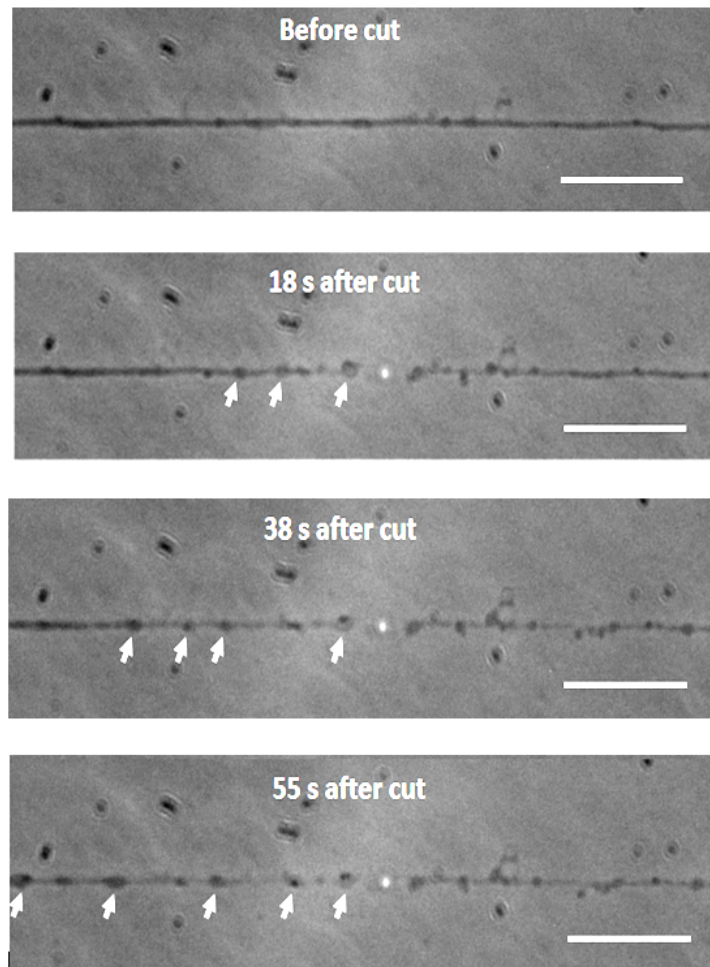


FIGURE 3.15: Time series of slow beading after laser cut. Beading, shown by white arrows, spreads away from the point of cut (a small white mark in the centre). Bar: $10\ \mu\text{m}$

Beading is also seen in the cases of partial cut where membrane remains intact but the cytoskeleton snaps and retracts. Beading after the laser cut is seen in axons pre-treated with Noco, Lat-A and ATP-depletion buffer as well.

3.6.5 Slow retraction after snapping:

Following the initial snapping, there are different behaviours of the cut shafts with respect to evolution of distance between the cut tip and the point of laser cut (fig. 3.16). Usually, axonal retraction after laser ablation is also accompanied by

changes in the radius of the axon, which may or may not develop in beading, but in this subsection we focus only on the retraction responses. We categorize them as follows:

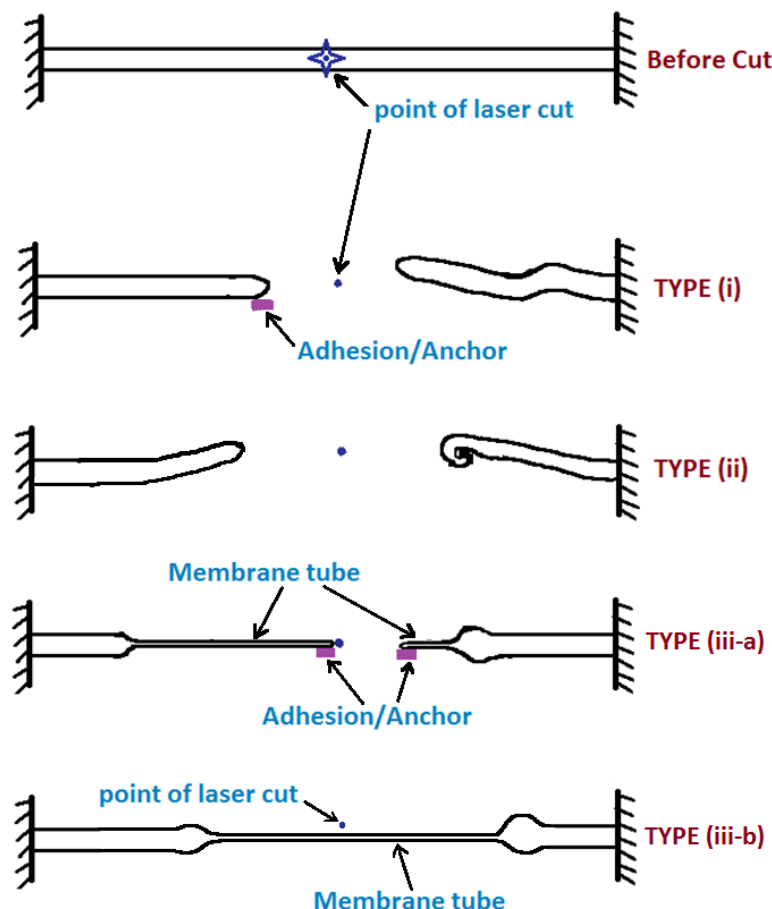


FIGURE 3.16: Different types of responses of axons *with respect to retraction* after laser ablation. Type (i): No further change *after the snapping*; the cut tip could be free (left) or adhered (right) to the substrate. Type (ii): The cut tip is free. It may swing away from the point of cut (left) or start winding up in the direction away from the point of cut (right). Both can result in a growing distance between the cut tip and the point of laser cut. Type (iii-a): The cut tip remains partially anchored to the surface only by the means of the membrane but the cytoskeleton retracts leaving behind a very thin membrane tube (left) or the initially free tip later forms an anchor on the substrate, then the cytoskeleton starts retracting leaving behind a very thin membrane tube (right). The cut shafts remains in the plane of the substrate. Type(iii-b): The axon is slightly above the substrate. The laser focussed on the substrate fails to cut the axon but the impact causes a discontinuity in the cytoskeleton, leaving the membrane tube intact. The cytoskeleton retracts through the membrane tube.

Type (i)

The tip of the cut axon remains stable without any further change. In some cases the tip might be free or anchored to the substrate (can be checked by perturbing

the surrounding fluid by creating a gentle flow; if the tip moves it is free, if it doesn't move then it is anchored).

Type (ii)

The cut tip is free. It may swing away from the point of cut or start winding up in the direction away from the point of cut. Both can result in a growing distance between the cut tip and the point of laser cut. Fig. 3.17 shows an example of the winding tip.

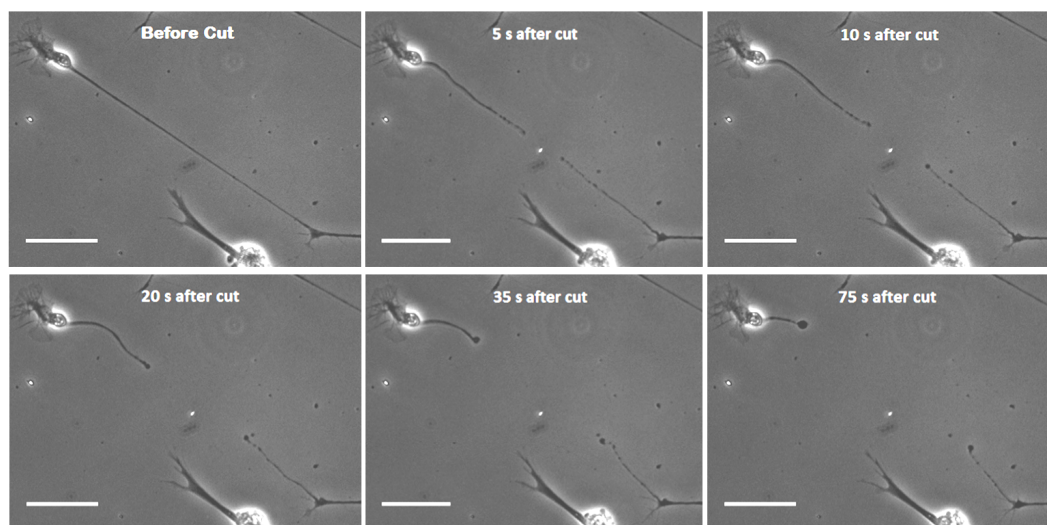


FIGURE 3.17: Type (ii) response after laser cut. The cut tips are free and start winding up at the tip. Later the winding stalls probably due to formation of anchors on the substrate. Bar: $40\ \mu\text{m}$

Type (iii)

The cut tip remains partially anchored to the surface only by the means of the membrane but the cytoskeleton retracts leaving behind a very thin membrane tube OR a cut-tip which was initially free, forms an anchor on the substrate, then the cytoskeleton starts retracting leaving behind a very thin membrane tube (fig. 3.16, Type (iii-a)). Here, the cut shaft remains in the plane of the substrate and there is a clear retraction front whose position can be traced with respect to time. The movie *Retraction-within-membrane-tube* shows an example where after snapping, the cut tip on the left side forms an anchor on the surface and the cytoskeleton starts retracting through the membrane tube. The numbers in the upper left corner indicate the real time in minute:second. The retraction plots shown in fig. 3.18 correspond to this category. As described before, a similar

retraction behaviour is seen when an axon is partially cut or when the laser just misses the axon leaving the membrane tube intact but making a discontinuity in the cytoskeleton (fig. 3.16, Type (iii-b)).

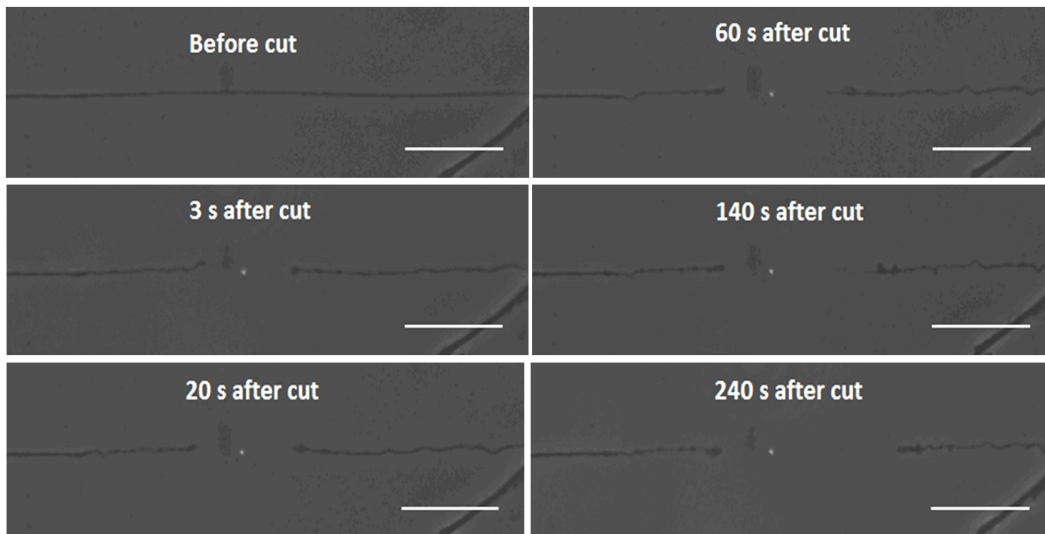


FIGURE 3.18: Type (iii) response of the cut shaft on the right side. There is an almost invisible, thin membrane tube between the point of the laser cut and the retraction front and the cytoskeleton seems to retract through this tube. The shaft on the left does not show retraction. Bar: $40\ \mu\text{m}$

The following plots (fig. 3.19) show a plot of the retracted distance *after the snapping* of a cut tip against time *after the snapping* for the type (iii). Each colour represents a different axon.

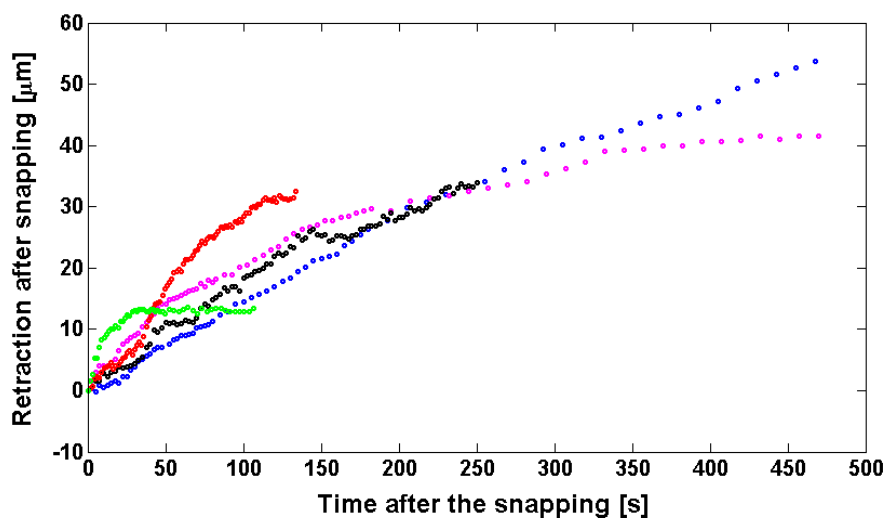


FIGURE 3.19: Retraction through an intact membrane tube. Each colour represents a different axon.

Slow Retraction of treated axons: The above three types of responses to laser cut are observed in samples pretreated with (i) noco and (ii) ATP depletion buffer as well. Fig. 3.20 and fig. 3.21 show the slow retraction through intact membrane tube (response type (iii)) corresponding to the noco treated axons and ATP depleted axons respectively, along with retraction of control axons plotted for comparison. As will be explained in the last chapter, treatment with Lat-A itself causes either retraction or loss of focal adhesions in most of the axons. Therefore it was difficult to collect data for retraction after laser cut with an intact or anchored membrane tube in Lat-A treated axons.

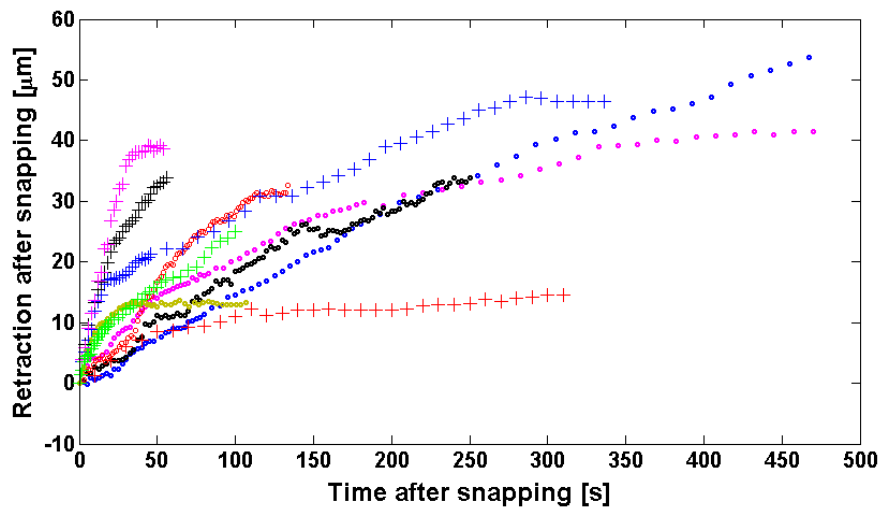


FIGURE 3.20: Retraction through an intact membrane tube. ‘o’ indicate control axons and ‘+’ indicate noco treated axons

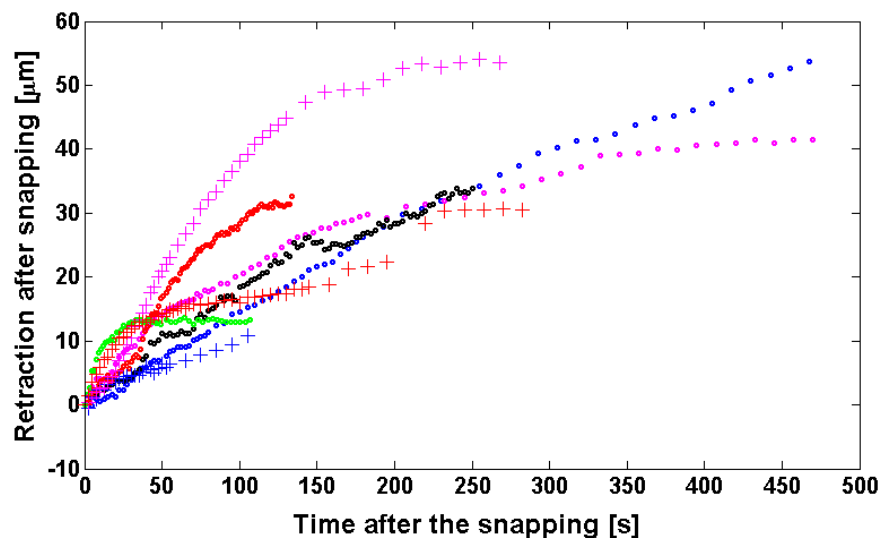


FIGURE 3.21: Retraction through an intact membrane tube. ‘o’ indicate control axons and ‘+’ indicate axons treated with ATP depletion buffer

3.6.6 Mechanical transection

These experiments were carried out in order to verify that the observed responses of axons to nano-second laser transection were not due to destructive effects of the laser. As described in the Materials and Methods section, a micropipette with a sharp jagged tip was used for the transection. However, as the axons in culture are in a very close proximity with the underlying glass coverslip, the action of micropipette resulted in pressing the axon against the glass surface before the transection happened. In most of the cases, this resulted in the membrane of the tips of the cut axon getting anchored on the surface, and thus we couldn't observe snapping of the axons. However the cytoskeleton retracted through the anchored membrane tube in many cases, very similar to the type (iii) response observed after laser transection. Fig. 3.22 shows one example of a mechanically transected axon where the cut shaft on the right side retreats and buckles and the cut shaft on the left side initially retracts through an intact membrane tube then develops beading. Fig. 3.23 shows the retraction plots of mechanically transected axons along with plots of the laser transected axons for comparison.

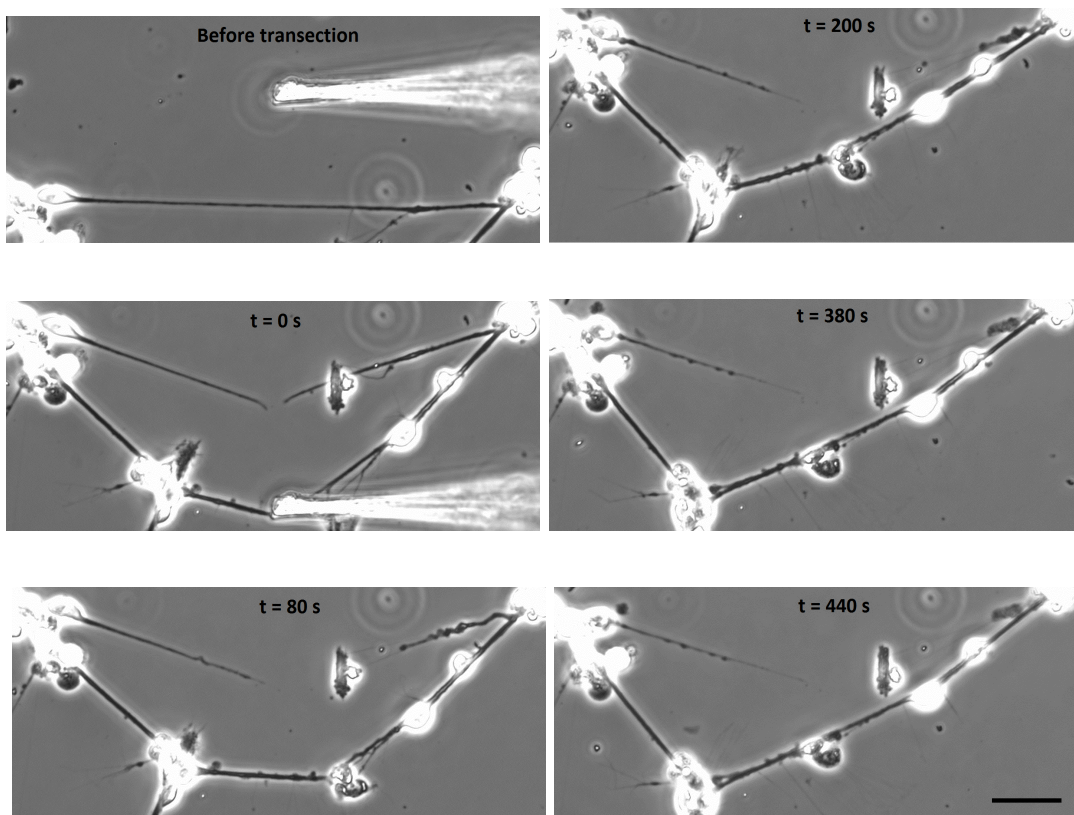


FIGURE 3.22: An axon before, just after ($t = 0$ s) and the mentioned duration after a mechanical transection using a glass micropipette (visible in the first panel, on right) with a jagged tip. The pipette is kept fixed with its sharp end touching the surface of a glass coverslip on which the axon is sitting. The coverslip with the axon is moved across the pipette tip so that the transection takes place ($t = 0$ s). The left side of the transected axon starts slowly retracting through an intact and anchored membrane tube and later develops beading ($t = 380$ s). The right side buckles and retreats in a complex way. Bar: $40 \mu\text{m}$

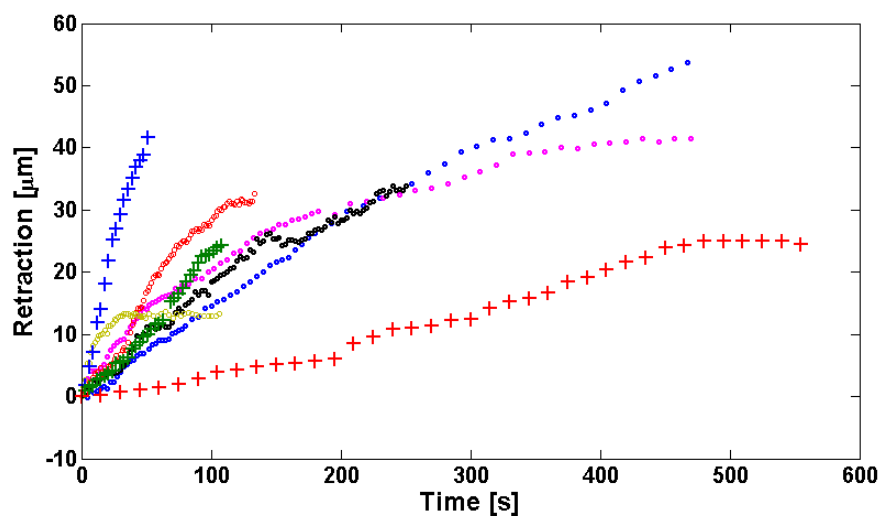


FIGURE 3.23: Retraction through an intact membrane tube. ‘o’ indicate laser-transected axons and ‘+’ indicate mechanically transected axons

3.7 Summary and Discussion

I. Snapping:

The very consistent snapping behavior of live axons after laser cut shows that the axons are under rest tension or pre-stress initially. Note that the measured snapping length (distance between each cut end of an axon and the point of laser cut) is not merely an elastic retraction response of the axons because it is also contributed by buckling of the shaft. In addition, as shown by the snapping even after the second cut, the rest tension or the pre-stress might be distributed locally along the axon. Therefore, a single cut does not fully relax the tension. Local relaxation of the tension at the point of laser cut may rupture the neighboring adhesion sites between the axon and the glass substrate as depicted in the fig. 3.24, depending upon the strength of the adhesion. The adhesion sites are indicated by small purple blocks with varying thickness which is proportional to the adhesion strength. After a laser cut, the weaker adhesion sites may rupture with more probability than the stronger ones and the snapping may depend upon the spatial distribution of the adhesion of varying strengths. As an example, the figure shows that the point of laser cut is in a closer vicinity of a strong adhesion site (thicker block) on the left side than that on the right side. Therefore the snapping length is smaller on the left side. Snapping length gives a measure of the fast response of axons to a laser cut, averaged over all these effects.

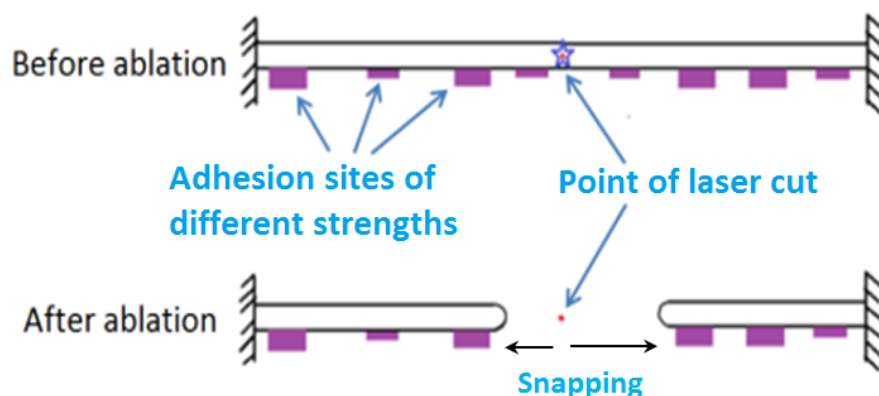


FIGURE 3.24: Possible effect of a distribution of adhesion sites (shown by purple boxes) of varying strengths along an axon on the snapping length. Thickness of a box corresponds to the adhesion strength of the site.

We have verified that axons which were fixed using two different methods namely aldehydes treatment (Methods section of Chapter 2) and cold ethanol treatment, do not show snapping. This is not due to strengthening of adhesion with the substrate as a result of the fixation process. On the contrary, a double cut (cut at two spatially separated locations) on the fixed axons results in the segment between the two cuts getting completely detached or free to get drifted around with the local currents in the surrounding medium. The fixation process is known to cross bind all the proteins inside a cell which may relax the rest tension or pre-stress in the axon. This implies that the snapping of live axons must be due to the tension or stress relaxation and not due to a destructive effect of the laser itself.

The snapping length remains unaltered by ATP depletion or Noco treatment whereas it gets reduced after Lat-A treatment. This rules out the possibility of active processes and MTs being the elements in which the rest tension or the pre-stress could be stored, leaving the possibility of f-actin and NFs. We could not investigate the role of NFs as there is no known available drug that cleanly disrupts NF structure without affecting the other elements.

II. Beading after cut: About 50% of the axons show radius modulations after the laser cut. In some cases the modulations build up to form clear beading over different time scales. Beading can take place on proximal as well as distal segments of cut axons. Since cytoskeletal stress and membrane tension should relax after an axon is cut, the observed beading must be driven by a mechanism which is fundamentally different from that where beading/pearling instability is set in due to a sudden rise in the membrane tension, like in the case of stretch induced [16] or osmotic shock driven pearling of axons [15]. Moreover, beading is also seen in the case of a partial cut where the membrane is intact but the cytoskeleton shows a discontinuity. Thus membrane tension is unlikely to play a role in the beading. Beading is also observed in ATP depleted axons as well as in Lat-A treated axons (depolymerized f-actin) and noco treated axons (de-polymerized MTs). Thus the beading process might be a passive response of the remaining cytoskeleton i.e. the neurofilaments, to the changed boundary conditions after a cut.

III. Retraction of cytoskeleton through membrane tube: The observation of slow retraction of cytoskeleton through a membrane tube, over long lengths (tens of μm) and long time (over a few minutes), opens a myriad of questions such as, is the retraction driven by active processes or is it a passive visco-elastic relaxation of cytoskeleton under a pre-stress, can one estimate the membrane-cytoskeleton viscosity through this, what keeps the uncut axon from attaining such a geometry etc. We have tried answering a few of them in this work. The experiments carried out in the ATP depleted condition where the retraction still takes place prove that it must be a process involving passive reorganization of the cytoskeleton within the membrane tube, triggered by a discontinuity formed due to the laser cut. The instances (fig. 3.19) where the relaxation saturates to a plateau value indicate visco-elastic relaxation of a pre-stress stored in the cytoskeleton (as the membrane is intact) with the elastic part contributed by the cytoskeleton and the viscous part contributed by the cytoskeleton alone or by membrane-cytoskeleton interaction or both. Retraction is not inhibited by Noco treatment and therefore the hypothesized pre-stress responsible for the retraction might not be stored in the MTs, leaving f-actin and neurofilaments as the remaining two possibilities.

Another possible mechanism for the observed retraction comes from the mechanical transection of axons (fig. 3.22, 3.23) which show that axonal transection leading to axonal retraction is independent of the method of transection. It was reported by Spira et al. [17] that a transection leads to a large Calcium influx from the external medium into the axon. This is shown to result in proteolysis (breaking down of proteins) over a significant length of the axon. We suspect that laser transection may lead to a similar situation. Even in the cases where the membrane tube is seen to remain intact while the cytoskeleton retracts, it is possible that the laser creates small pore(s) in the membrane [18]. Before the pores get sealed due to the line tension in the lipid bilayer, the calcium influx may take place. It needs further experiments like imaging Ca^{+2} waves in axons after laser ablation and their effect on the cytoskeleton.

Thus, laser transection provides a clean way of inducing the commonly observed shape deformations of axons like beading and retraction by *relaxing* the internal stresses or tension as opposed to the earlier studied cases of stress build up like

the osmotic shock induced or stretch induced pearling. Therefore the mechanisms at play also could be different from those studied before. An advantage of the method of laser ablation is that we could conduct these experiments in an ATP depleted environment and showed that the shape transformations observed after laser ablation must be emerging from a passive mechanism. An inquiry for more details of such a mechanism requires further experiments on live neurons which are transfected to express fluorescently labelled cytoskeletal elements.

Bibliography

- [1] N Hirokawa. Cross-linker system between neurofilaments, microtubules and membranous organelles in frog axons revealed by the quick-freeze, deep-etching method. *The Journal of Cell Biology*, 94(1):129–142, 1982. doi: 10.1083/jcb.94.1.129. URL <http://jcb.rupress.org/content/94/1/129.abstract>.
- [2] Sanjay Kumar, Iva Z. Maxwell, Alexander Heisterkamp, Thomas R. Polte, Tanmay P. Lele, Matthew Salanga, Eric Mazur, and Donald E. Ingber. Viscoelastic retraction of single living stress fibers and its impact on cell shape, cytoskeletal organization, and extracellular matrix mechanics. *Biophysical Journal*, 90(10):3762 – 3773, 2006. ISSN 0006-3495. doi: <http://dx.doi.org/10.1529/biophysj.105.071506>. URL <http://www.sciencedirect.com/science/article/pii/S0006349506725565>.
- [3] Bray Dennis. Mechanical tension produced by nerve cells in tissue culture. *Journal of Cell Science*, 37:391–410, 1979.
- [4] T J Dennerll, P Lamoureux, R E Buxbaum, and S R Heidemann. The cytomechanics of axonal elongation and retraction. *The Journal of Cell Biology*, 109(6):3073–3083, 1989. doi: 10.1083/jcb.109.6.3073. URL <http://jcb.rupress.org/content/109/6/3073.abstract>.
- [5] *CNS Regeneration: Basic Science and Clinical Advances*, chapter Neuronal Responses to Axotomy. Academic Press, 1998.

- [6] JD Glass and JW Griffin. Neurofilament redistribution in transected nerves: evidence for bidirectional transport of neurofilaments. *The Journal of Neuroscience*, 11(10):3146–3154, 1991. URL <http://www.jneurosci.org/content/11/10/3146.abstract>.
- [7] Hadas Erez and Micha E. Spira. Local self-assembly mechanisms underlie the differential transformation of the proximal and distal cut axonal ends into functional and aberrant growth cones. *The Journal of Comparative Neurology*, 507(1):1019–1030, 2008. ISSN 1096-9861. doi: 10.1002/cne.21522. URL <http://dx.doi.org/10.1002/cne.21522>.
- [8] Markolf H Niemz. *Laser-Tissue Interactions*. Springer, 2003.
- [9] M F Yanik, H N Cinar, A D Chisholm, Y Jin, and A Ben-Yakar. Functional regeneration after laser axotomy. *Nature*, 2004.
- [10] Christopher V. Gabel. Femtosecond lasers in biology: nanoscale surgery with ultrafast optics. *Contemporary Physics*, 49(6):391–411, 2008. doi: 10.1080/00107510802628263. URL <http://www.tandfonline.com/doi/abs/10.1080/00107510802628263>.
- [11] G. Nageswara Rao, Sucheta S. Kulkarni, Sandhya P. Koushika, and Kaushtubh R. Rau. In vivo nanosecond laser axotomy: cavitation dynamics and vesicle transport. *Opt. Express*, 16(13):9884–9894, Jun 2008. doi: 10.1364/OE.16.009884. URL <http://www.opticsexpress.org/abstract.cfm?URI=oe-16-13-9884>.
- [12] Young-tae Kim, Kailash Karthikeyan, Sajal Chirvi, and Digant P. Dave. Neuro-optical microfluidic platform to study injury and regeneration of single axons. *Lab Chip*, 9:2576–2581, 2009. doi: 10.1039/B903720A. URL <http://dx.doi.org/10.1039/B903720A>.
- [13] Amy N. Hellman, Behrad Vahidi, Hyung Joon Kim, Wael Mismar, Oswald Steward, Noo Li Jeon, and Vasanth Venugopalan. Examination of axonal injury and regeneration in micropatterned neuronal culture using pulsed laser microbeam dissection. *Lab Chip*, 10:2083–2092, 2010. doi: 10.1039/B927153H. URL <http://dx.doi.org/10.1039/B927153H>.

- [14] M Vassalli, M Basso, and F Difato. Measurement of tension release during laser induced axon lesion to evaluate axonal adhesion to the substrate at piconewton and millisecond resolution. *Journal of visualized experiments : JoVE*, 2013.
- [15] Pramod A. Pullarkat, Paul Dommersnes, Pablo Fernández, Jean-Fran çois Joanny, and Albrecht Ott. Osmotically driven shape transformations in axons. *Phys. Rev. Lett.*, 96:048104, Feb 2006. doi: 10.1103/PhysRevLett.96.048104. URL <http://link.aps.org/doi/10.1103/PhysRevLett.96.048104>.
- [16] Sydney Ochs, Rahmna Pourmand, Kenan Si, and Richard N. Friedman. Stretch of mammalian nerve in vitro: Effect on compound action potentials. *Journal of the Peripheral Nervous System*, 5, 2000.
- [17] Micha E. Spira, Ruthi Oren, Ada Dormann, and Daniel Gitler. Critical calpain-dependent ultrastructural alterations underlie the transformation of an axonal segment into a growth cone after axotomy of cultured aplysia neurons. *THE JOURNAL OF COMPARATIVE NEUROLOGY*, 457:293–312, 2003.
- [18] Shigeki Iwanaga, Tomoyuki Kaneko, Katsumasa Fujita, Nicholas Smith, Osamu Nakamura, Tetsuro Takamatsu, and Satoshi Kawata. Location-dependent photogeneration of calcium waves in hela cells. *Cell Biochemistry and Biophysics*, 45(2):167–176, 2006. ISSN 1085-9195. doi: 10.1385/CBB:45:2:167. URL <http://dx.doi.org/10.1385/CBB%3A45%3A2%3A167>.

Chapter 4

Membrane dynamics in axons probed using tether pulling technique

In order to determine whether the nocodazole (Noco) induced beading of axons is a shape instability caused by a sudden rise in the membrane tension, it was essential to measure and compare the membrane tension before and after Noco treatment. The technique of pulling membrane tether or membrane nanotube provides an elegant yet simple way to do the same. Apart from measuring the static tether force on axons subjected to drug treatments, from which the membrane tension values can be compared, we also explored some interesting and unique dynamic properties of the axonal membrane and the underlying cytoskeleton. All the tether pulling experiments described in this chapter were carried out in Prof. Patricia Bassereau's lab in Institute Curie, Physio-chemie Unit, Paris, using an optical trap chiefly developed by Dr. Thomas Bornschlögl. The corresponding experimental results are modelled by a theoretical description developed in collaboration with Prof. Jacques Prost (Institut Curie).

The chapter is structured as follows:

- Theory of Membrane Nanotubes (Basic principles behind the membrane tension measurement)
- Previous experimental findings
- Standard methods of tether pulling
- Results and Discussion
- Conclusion

4.1 Theory of Membrane Nanotubes

A lot of work has been done on the equilibrium or static shape of lipid bilayer structures. The following discussion on the static behaviour of membrane tethers is mostly based on the formulation by Derenyi [1] and Powers [2]. The terms membrane nanotube/tether have been used interchangeably.

4.1.1 Static behaviour

The radius of a membrane nanotube is uniquely determined by the bending modulus of the membrane and the tension on the membrane. Once the radius is measured, one can calculate the tension if the bending modulus is known. We will see how these three quantities are inter-related. Imagine an unbounded flat sheet of lipid membrane being pulled by a point force. It will result into the formation of a cone-like protrusion centred around the point of force application. If the membrane is under tension, it will try to minimize the total surface area in order to minimize the surface energy thus leading to the formation of just a lipid-link of *zero radius* between the point of application of the force and the membrane. But such a thin structure with very high curvature (inversely proportional to the radius) costs a huge bending energy due to finite bending modulus of the lipid bilayer, thus putting a lower limit on the radius of the tether. The result will be formation of a cylindrical lipid tube with a small but finite radius to optimize between the surface energy and the bending energy. The radius of the tube at

equilibrium can be calculated by minimizing the total free energy. In general, the free energy of a lipid bilayer with mean curvature H , in absence of external force has contributions from (i) the Helfrich-Canham curvature energy \mathcal{F}_{H-C} . because lipid bilayers have a finite bending modulus B (ii) Surface energy because the number of lipids exposed to the water-like environment is restricted, giving rise to a surface tension or membrane tension. T (iii) Pressure-volume term in the case of closed shapes, coming from the pressure-difference across the membrane. The Helfrich-Canham energy for a vesicle is

$$\mathcal{F}_{H-C} = \int \frac{B}{2}(2H)^2 dA$$

Here we have not considered the contribution from Gaussian curvature of the vesicle because its integral is a topological invariant for closed shapes. We are also assuming that the environments across the vesicle membrane and the lipid composition of the bilayer are respectively symmetric so that there is no spontaneous curvature. Typically for a vesicle, the total volume V and surface area A are conserved. Then the pressure difference Δp and the membrane tension T are the corresponding Lagrange multipliers. Thus the total free energy for a vesicle is

$$\mathcal{F} = \int \left[\frac{B}{2}(2H)^2 + T \right] dA - \Delta p V$$

Minimizing this free energy will give the equilibrium relationship between Δp , T and shape of the vesicle given the fixed values of V and A . For example, for a spherical vesicle of radius R , $\Delta p = \frac{2T}{R}$.

Now consider the case where an external pulling force f_t operating on a tense vesicle at a point pulls out a stable cylindrical tube of radius R_t and length L_t as shown in fig. 4.1

Here the volume and area of the tether are not the conserved quantities as the tube is connected with the vesicle which acts as the reservoir of lipid and the filling

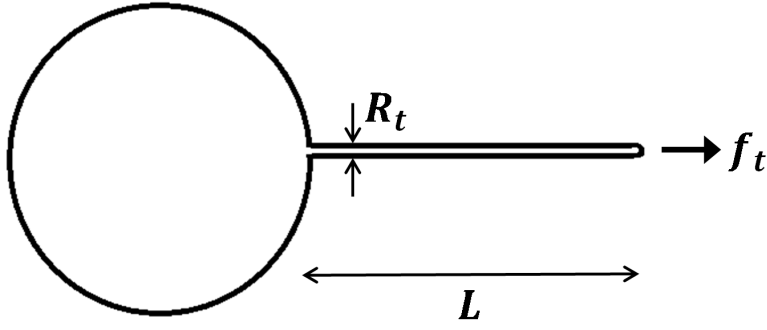


FIGURE 4.1: Tether of radius R_t and length L pulled with force f_t from a vesicle.

medium. Instead the conserved quantities are f_t , Δp and T . At equilibrium the last two quantities are the same as Δp and T for the big vesicle from which the small tether has been pulled. In addition, there will be a contribution $f_t L_t$ to the free energy from the applied force. For a small stable tether, Δp is negligible and it can be shown that it contributes insignificantly towards determining the tether radius. Thus for the cylindrical tube with $H = -\frac{1}{R_t}$ the total free energy is as follows

$$\mathcal{F} = \left[\frac{B}{2} \left(\frac{1}{R_t} \right)^2 + T \right] 2\pi R_t L_t - f_t L_t \quad (4.1)$$

Minimizing the free energy with respect to R_t gives its value at equilibrium (R_0)

$$R_0 = \sqrt{\frac{B}{2T}} \quad (4.2)$$

Thus we see that the tether radius at equilibrium is a function of only the bending modulus and tension of the membrane and is independent of the pulling force. Substituting the expression for R_0 in (4.1) we get

$$\mathcal{F} = (\sqrt{2BT}) 2\pi L - f_t L_t$$

Now the value of applied force required to keep a tube of length L_t pulled at equilibrium (f_0) can be found by equating the above free energy to zero. Thus we get

$$f_0 = 2\pi\sqrt{2BT} \quad (4.3)$$

The force is independent of the tether length. If a tether pulling experiment can measure R_0 and f_0 one can calculate the tension T using (4.2) and (4.3) as

$$T = \frac{f_0}{4\pi R_0} \quad (4.4)$$

Using equations (4.2), (4.3) and (4.4) we can write

$$T = \frac{B}{2R_0^2} \quad (4.5)$$

Or the tension can be expressed in terms of the tether force and bending modulus using equations (4.2) and (4.4) as

$$T = \frac{f_0^2}{8\pi^2 B} \quad (4.6)$$

4.1.2 Dynamic behaviour

The dynamics of tether formation have been studied theoretically by Derenyi et al [3] and experimentally by Koster et al [4]. In the latter work, it is shown that there exists a force barrier for the formation of membrane tubes by applying pulling force and the value of the barrier linearly increases with the radius of the area on which the pulling force is exerted. It is speculated that the formation of membrane tube depends upon how the pulling force is applied. After formation of a tether, the tether force increases as the rate of tether elongation. It was shown through a detailed analysis [5] that when tether from a pure lipid vesicle is elongated by pulling at speed v_t the instantaneous tether force f_t has an additional contribution from the friction between the two bilayers apart from the static force in equation (4.3). The friction arises because the outer layer, having a slightly greater tether radius than the inner layer, gets pulled more. Effecting into a relative movement between lipids in the outer monolayer and those in the inner monolayer. The expression for the instantaneous force is given as follows

$$f_t = f_0 + 2\pi[\eta_m h^2 \ln(\frac{R}{R_t})v_t] \quad (4.7)$$

where f_0 and R_t continue to denote the same quantities as in the discussion on statics of tether force. η_m is the effective viscosity of the bilayer, R is the radius of the vesicle and h is the bilayer thickness. There is an additional contribution to f_t coming from the global difference in area of the two monolayers but it can be shown to be negligible unless the tether length is over hundreds of micron.

4.2 Previously established experimental findings

The technique of tether pulling has been widely employed to understand physical properties of lipid membranes in a variety of systems like synthetic phospholipid vesicles, red blood cells, neuronal growth cones etc. Evans and Yeung [5] validated the relationship between tether radius and membrane tension by pulling tethers from synthetic vesicles and estimated the value of the bending modulus. They also proved the relationship between the instantaneous tether force and the pulling speed (equation (4.7)) and claimed that the major contribution to the membrane viscosity comes from the inter monolayer coupling. Sheetz, Dai and Hochmuth have done extensive work on different types of biological cells where they measured the rest membrane tension and other properties like the bending modulus, coefficient of viscosity due to membrane-cytoskeleton interaction etc. They claimed that the apparent membrane tension measured on biological cells is a combined effect of the in-plane membrane tension and an energy of adhesion between the membrane and the underlying cytoskeleton [6]. This claim was supported by their experiments on neuronal growth cone membrane where it was demonstrated that depolymerization of the cytoskeleton, especially actin, results in smaller values of the apparent membrane tension. In addition they also showed a similar relationship between tether force and the rate of tether elongation, to that shown by Evans and Yeung (fig. 4.2). Notice that equation (4.7) implies that the force instantaneously drops back to f_0 when the pulling is stopped. However, the experiments on a variety of systems like synthetic lipid vesicles [7] as well as

biological systems like red blood cells [8], outer hair cells [9] and *E. coli* [10] show that the force takes a finite time to relax. We report similar behaviour in our experiments on axons which will be later discussed in details. There is no theoretical formalism for this force relaxation process of plasma membrane till now. Thus the measurement of the force relaxation time may help in modelling the mechanism of this phenomenon.

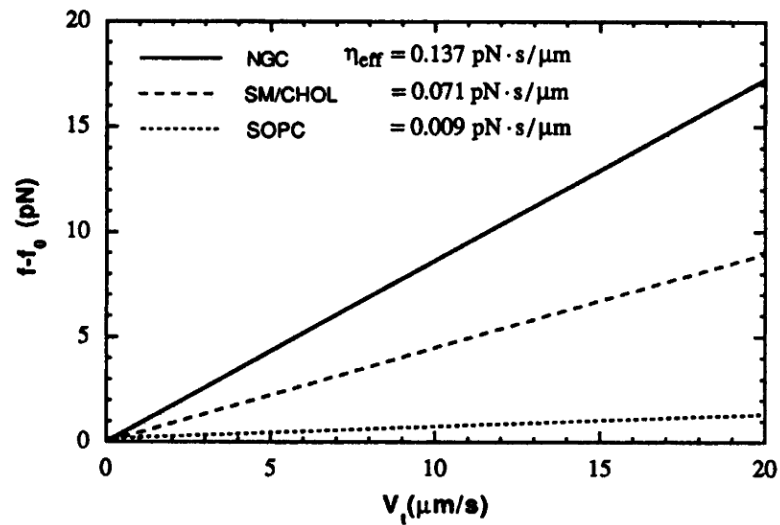


FIGURE 4.2: Tether force v/s pulling speed, taken from [6]. The solid line is for neuronal growth cone membrane, the dashed and the dotted lines are for synthetic lipid vesicles. The slope is the effective viscosity (η_{eff})

Experiments by the Sheetz group on chicken embryonic fibroblast cells demonstrated that there exists a range of tether length for which the tether force remains constant (fig. 4.3).

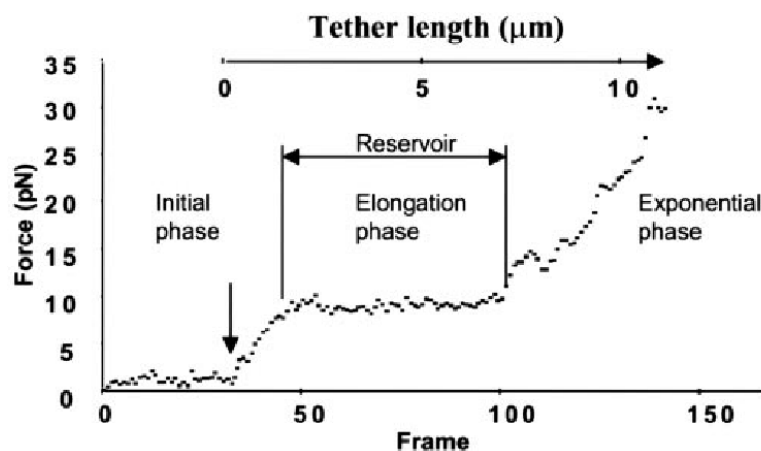


FIGURE 4.3: Tether force with time during tether formation and elongation. Taken from [11]

This observation points towards existence of membrane reservoirs in cells, which are employed to buffer changes in the membrane tension and maintain the membrane tension at a constant value [11]. Recent work by B. Sinha *et al* [12] established caveolae, 60-80 nm cup shaped membrane invaginations as a possible candidate for such reservoirs. They showed that sudden surge in the membrane tension caused by applying osmotic shock or mechanical stretching to HeLa cells triggers flattening and disassembly of caveolae. This makes an extra amount of membrane available to the cells, buffering the membrane tension. It is worth taking a note of the fact that axons are known to be devoid of membrane invaginations like caveolae [13]. However it is experimentally shown that axons from chicken embryos can withstand large hikes (20%) in the membrane area without getting ruptured whereas biological membranes are known to rupture beyond 3 – 5% of stretching [14]. Experiments on molluscan neurons [15] hint towards the existence of different type of membrane reservoirs than invaginations like caveolae, which are responsible for the tension buffering in neurons.

From the point of view of understanding the membrane-cytoskeleton interaction in cells, it is interesting to study the behaviour of the tether-cell junction on the surface of a cell. In synthetic lipid vesicle systems it has been experimentally and theoretically shown that multiple tethers tend to merge [16], [17]. This is possible because there is no hindrance to the movement of a tether-vesicle junction on the surface of a vesicle. However, this is not the case with tethers pulled from

the plasma membrane of many types of cells, for e.g., neutrophils [18], fibroblasts (private communication with Darius Koester) and HeLa cells (data presented in the Results section) where a tether-cell junction is unable to move laterally. The reason is speculated to be a strong connection between the cell membrane and the underneath cytoskeleton, especially the cortical actin at the tether-cell junction which acts as a barrier in the lateral movement of the junction. Our experiments show that in axons, this behaviour is quite different compared to other types of cells.

Recently there has been found yet another signature of a direct linking between the cytoskeleton and the membrane tether force in the form of spontaneous build ups and ruptures of pulling force in the absence of any external perturbation in tethers pulled from mast cells membranes [19] and in the filopodia of HeLa cells [20]. They are proposed to be originating from actin dynamics inside the tethers and the filopodia respectively and may play an important role in the cell motility and functioning. We have observed similar transient features in axonal tether force which are strongly f-actin dependent.

4.3 Experimental Methods of tether pulling

In order to investigate on the viscoelastic properties of bilayer membranes, there have been employed different techniques of tether pulling from synthetic vesicles and biological cell membranes, the most prominent ones being the micropipette aspiration method fig. 4.4 and optically trapped beads method fig. 4.5 [21]. The former is useful for vesicles or cells like RBCs suspended in water-like medium whereas the latter is generally used on adherent cells. The two techniques can also be used in a combined way. In both methods a microbead is first held in contact with the object of interest (a vesicle or a cell) till there is a formation of adhesion and then pulled away from the object in order to form a membrane tube as required. Thus the operating principle is the same but the latter method has a better control and precision in terms of the applied tether pulling force.

4.3.1 Micropipette aspiration method

The object of interest in suspension (a vesicle or a suspended cell) is held aspirated using a micropipette as shown in the right part of fig. 4.4. The suction pressure (or negative) P_p which is controllably applied decides the tension T on the vesicle. A microbead is held aspirated in another micropipette on the other side (left side of fig. 4.4) and brought in contact with the vesicle. When they are held in contact for a sufficient time so as to form an adhesion, the microbead is moved away with the help of the pipette, resulting into tube formation.

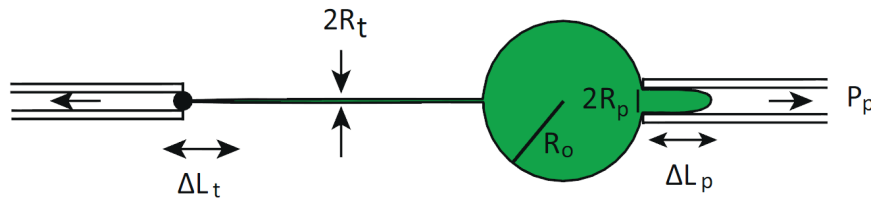


FIGURE 4.4: Micropipette aspiration method of tether pulling, taken from [21]

As tension on the vesicle or cell membrane is controlled by the user in this method, it can not be used to measure rest tension. The tether force can be indirectly estimated from equations (4.2) and (4.3) by measuring the tether radius and tension but it can not be applied controllably. However this method was extensively used to measure bending moduli of lipid bilayers [5]. For investigations on the dynamics of membrane properties it is better to use the optical trap method.

4.3.2 Optical trap method

Here the bead with which a tether is pulled from a vesicle or a cell membrane is held trapped in laser tweezers. The trap acts like a Hookean spring. Thus the tether force can be directly measured from the displacement of the bead (x) away from the centre of the trap by the relation $f_t = -k \cdot x$ where k is the spring constant of the optical/laser trap. This method allows the user to record f_t as a time series if a fast and accurate detection device like a quadrant photodiode is used for measuring x

for a well calibrated trap. The actual working details of this method are explained later. Direct measurement of the tether force allows measuring rest membrane tension using equation (4.4). Tethers can be readily pulled from adherent cells or from suspended cells/vesicles by using a micropipette to aspirate and hold the suspended cell in place.

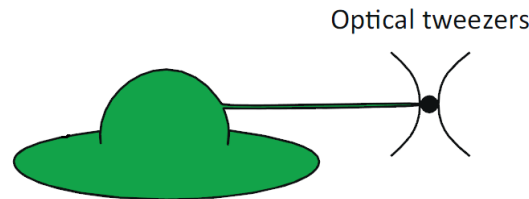


FIGURE 4.5: Optical trap method of tether pulling, taken from [21]

In the following, we explain the basic principles of an optical trap built with a laser.

4.3.2.1 Optical Trap

An optical trap consists of single powerful laser beam focussed at a point in space using a high numerical aperture lens. As shown in the fig. 4.6, just an unobstructed laser beam having a Gaussian intensity profile without an objective lens can work as a 2-dimensional trap in a plane perpendicular to its direction of laser propagation. Here F_1 and F_2 are forces acting on the spherical bead due to refraction of ray 1 and ray 2 respectively. If the bead moves off-centre as shown in the left panel, the net force F_{net} pushes the bead back towards the centre of the trap. However, as shown in the right panel, even when the bead is at the centre of the trap with zero lateral force acting on it, there is a small net force acting on the bead in the direction of laser propagation, which may destabilize the trap.

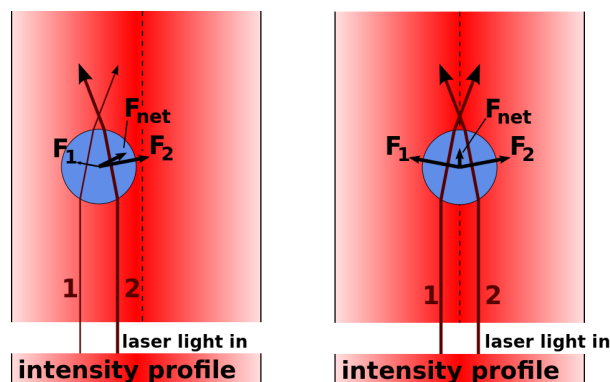


FIGURE 4.6: Ray optics explanation (unfocused laser). When the bead is displaced from the beam center (left panel), the larger momentum change of the more intense rays like ray 2 cause a net force to be applied back toward the center of the laser. When the bead is laterally centered on the beam (right panel), the resulting lateral force is zero. But an unfocused laser still causes a force pointing away from the trap center in the direction of laser propagation. Image source: Wikipedia

Introducing a high numerical aperture objective lens makes trapping possible along the third dimension (direction of the laser propagation) as shown in fig. 4.7.

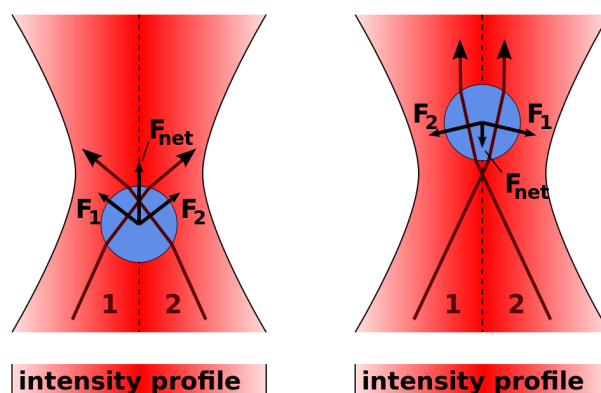


FIGURE 4.7: Ray optics explanation (focused laser). In addition to keeping the bead in the center of the laser, a focused laser also keeps the bead in a fixed axial position: The momentum change of the focused rays causes a force towards the laser focus, both when the bead is in front (left panel) or behind (right panel) the laser focus. So, bead will stay slightly behind the focus, where this force compensates the scattering force.

Image source: Wikipedia

4.3.2.2 Tether pulling using optically trapped beads

We used the method of optical trap as it has a better control on applied force, better accuracy (about 1 pN) and much better use for dynamic force measurements (at the rate of 1 kHz or more) if coupled with a photo-diode for imaging

the trapped bead. A schematic representation of the this set-up is shown in fig. 4.8

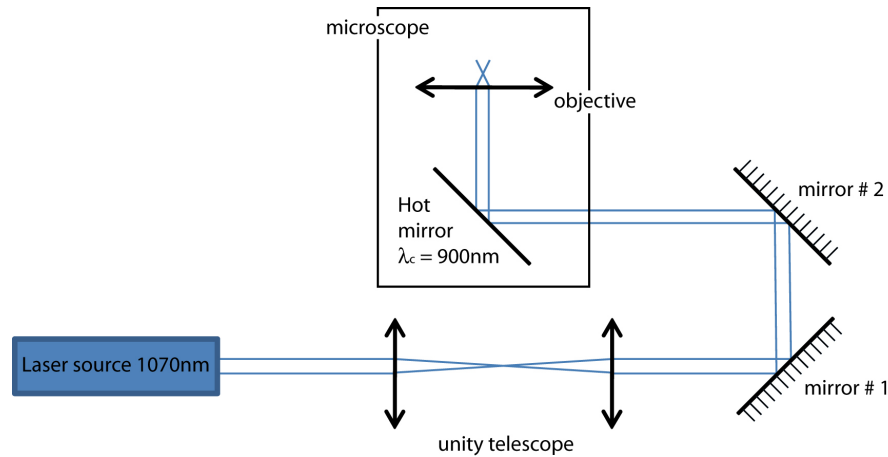


FIGURE 4.8: Schematic of the laser trap.

As shown in fig. 4.8, the trap consists of a Ytterbium fiber laser at 1070 nm (IPG Photonics) and a Nikon TE2000 confocal microscope with a 100x (N.A. 1.3) oil immersion objective. The mirrors are used to direct the beam into the back aperture of the microscope in such a way that finally the laser beam is parallel to the optical axis of the microscope. The power is adjusted to be $\sim 125mW$ at the objective. Once the trap is set, the centre of the trap is fixed in space. Any relative movement between the trap centre and the sample has to be mediated by moving the sample. The sample consists of adherent neuronal cells (Appendix A) with loading medium that contains carboxylated polystyrene beads (Spherotech, $1.85\mu m$ diameter) loaded in a custom made chamber held fixed on the microscope stage. The loaded neuronal cells are kept at 36 ± 1 °C during the experiment by the means of heating the 100x objective using a hot water circulator. The stage is moved using a voltage controlled piezo (MadCityLabs) such that a selected axon is brought in contact with an optically trapped bead, making a non-specific adhesion between the two. Then the axon is moved away from the bead, the movement results in tether formation. Position of the bead can be simultaneously recorded by

- A quadrant photo diode (QPD) sitting in the back-focal plane of the microscope condenser lens which records interference of the unscattered laser beam with laser light scattered by the microbead.

- An infra-red camera ($750\text{ nm} < \lambda < 900\text{ nm}$) which collects light from the microscope condenser.

The imaging arrangement is depicted in fig.4.9

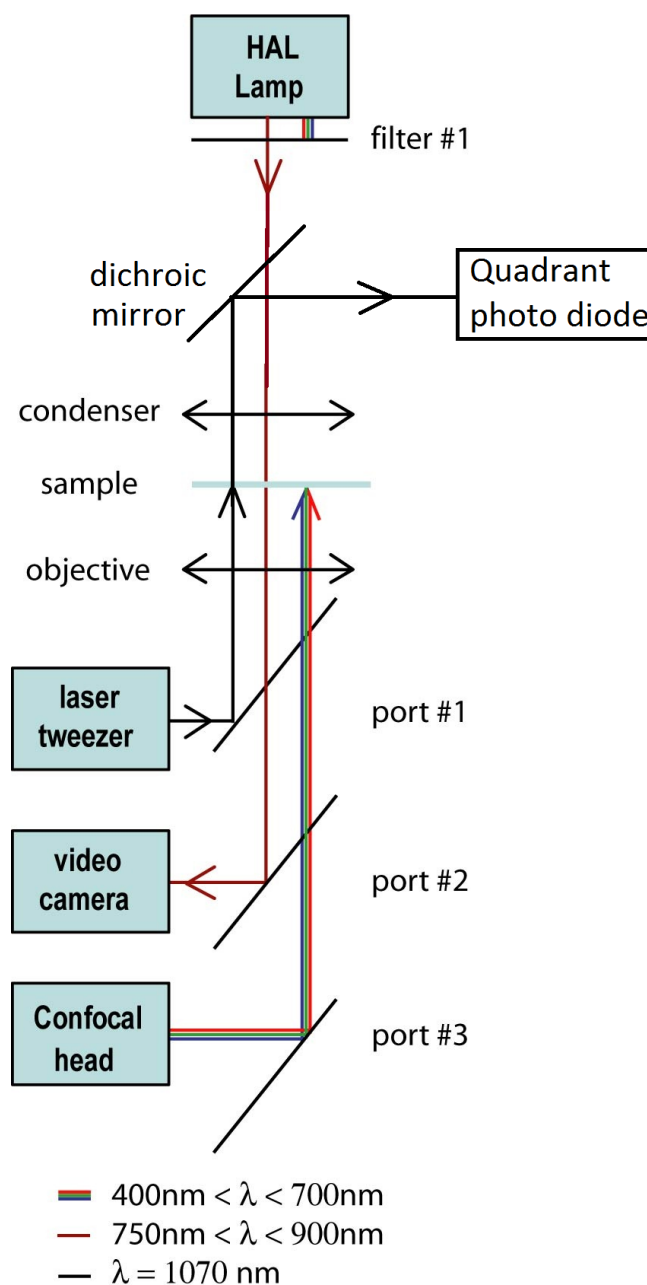


FIGURE 4.9: Schematic of imaging and position detection

Sample preparation: Chicken DRG neurons are grown using the protocol mentioned in the appendix A. About half an hour prior to the experiment, the growth

medium is changed to the experimental medium (without methocel). The axon and the tether are imaged using the confocal photo-multiplier tube by making the membrane fluorescent using a dye FM 4-64 Invitrogen at $14 \mu M$. Wherever mentioned, the cytoskeleton drugs Nocodazole and Latrunculin-A were added to the experimental medium at least 20 and 30 minutes prior to the experiment at $16.7 \mu M$ and $1 \mu M$ respectively.

Trap Calibration:

In the absence of any other force, a trapped bead is sitting at the centre of a parabolic potential well just as if it were attached to a relaxed Hookean spring. Any displacement \mathbf{x} of the bead away from the trap centre results in the force $\mathbf{F} = -k\mathbf{x}$ acting on the bead where k is the trap stiffness. Thus, if the bead is attached to an object which displaces the bead away from the trap centre, one can calculate the force exerted by that object on the bead if k is known. The trap was calibrated along each of the X and Y axes independently (the optical axis of the microscope is Z-axis) to obtain values of k_x and k_y , using two different methods for each axis.

1. Viscous drag method

The simplest and most common way to calibrate a trap is by applying flow of medium surrounding the trapped bead. The bead starts moving due to the viscous drag force of the medium F_D (calculated using Stokes law if the medium viscosity η is known) against the trap force. The latter builds up as the bead gets more and more displaced from the trap centre till it balances the drag force and the bead position gets stabilized at x_0 . At this point,

$$kx_0 = F_D = 6\pi\eta Rv$$

where v is the relative velocity of the medium with respect to the bead and R is the bead radius. Thus k can be calculated by measuring the plateau value x_0 of the bead displacement. Although this is a simpler way of trap calibration, one has to apply a correction to the Stoke's law to take care of the effect of the chamber walls especially if a bead is close to a wall. It is also difficult to do this calibration

in situ. One has to also feed in value of the viscosity of the medium.

2. Fourier Transform method

In this method, the viscosity of the medium is not required to be known. It makes use of the Brownian fluctuations of the position of a trapped bead in the presence of an externally applied sinusoidal movement of the surrounding medium with amplitude A and frequency ν_{drive} [22]. One can write the Langevin equation for the trapped bead. The solution is just a sum of two terms : the Brownian motion part and the driven or applied motion part. The form of the solution gets much simplified when the bead-position distribution is Fourier transformed to the frequency space. Then the power spectral density (PSD) of the bead position is given by

$$P(\nu) = \frac{D}{\pi^2(\nu^2 + \nu_c^2)} + \frac{A^2}{2(1 + \frac{\nu_c^2}{\nu_{drive}^2})} \delta(\nu - \nu_{drive}) \quad (4.8)$$

where $D = \frac{k_\beta T}{\gamma}$ is the diffusion constant, T is the absolute temperature measured around the trapped bead, k_β is the Boltzmann constant and $\nu_c = \frac{k}{2\pi\gamma}$ is the corner frequency of the Lorentzian distribution (first term in (4.8)) coming from the Fourier transform of Brownian motion part of the trapped bead (at trap stiffness k). The second term gives a delta function spike due to the applied sinusoidal displacement at frequency ν_{drive} against the backdrop of the Lorentzian (fig. 4.10). Evolution of the bead position (recorded by the QPD) is Fourier transformed and fit to (4.8) to give values of D and ν_c which in turn can eliminate γ and give the value of trap stiffness k . As the QPD records the signal in Volt, the units of PSD are $Volt^2.s$ and those of k are $NVolt^{-1}$. One needs to calibrate the QPD to convert the signal from Volt to meter so as to get the final value of k in $N \times m^{-1}$.

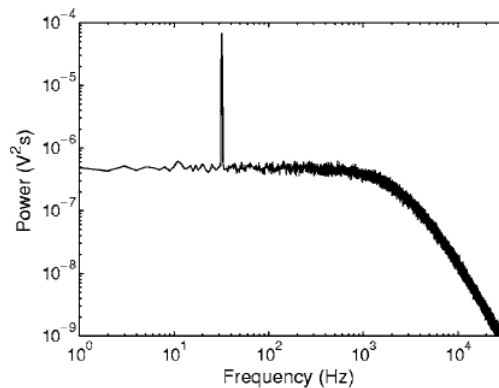


FIGURE 4.10: Power spectrum of a trapped bead with an externally applied sinusoidal perturbation, taken from [22]

4.4 Results and Discussion

This project was primarily aimed at finding out whether the action of Noco results in a higher value of membrane tension which can trigger the shape change from a uniform cylindrical geometry to the beaded geometry. In this light we first made the static force measurements for the control and drug-treated axons to see whether the membrane tension has changed. We noticed some interesting dynamic properties of the axon membrane in response to externally applied step-displacements. We could also record spontaneous rises and falls in the tether force and explored these dynamic properties in further details as described in the following. For a convenience of notation, the co-ordinate axes are chosen in such a way that the axon is always oriented along X-axis while a tether is oriented along Y-axis at equilibrium.

4.4.1 Static tether force measurements

As explained in the experimental set-up section, a selected axon is brought in contact with the trapped bead, held for 2 to 5 s and is then displaced away from the bead in the direction perpendicular to the long axis of the axon such that it resulted in the formation of a tether of length 2 to 5 μm . During the process of tether formation the force exerted by the cell membrane on the bead transiently rises then relaxes and gets stabilized at a value called as static force

(f_0) within 8 to 10 s after the pulling is stopped. Our experiments give the values of $f_0 = 10.75 \pm 1.87 pN$ for 12 axons in control conditions. These values lie between those reported for growth cones of chicken DRG neurons where $f_0 = 6.6 \pm 0.3 pN$ [23] and for mice ganglionic axons where $f_0 = 16 \pm 3 pN$ [24]. We can estimate the value of the membrane tension by putting a value for the bending modulus of chicken DRG axon membranes as measured in [6] i.e. $B = 2.7 \times 10^{-19} N.m$ in equation (4.6). We get the effective membrane tension $T \sim 5.5 \times 10^{-6} N.m^{-1}$, in agreement with the values obtained by the Sheetz group.

In order to decide whether a large hike in the membrane tension causes axon beading after noco treatment, we measured the static tether force f_0 on noco treated and beaded axons. Fig. 4.11 shows a boxplot of the distributions of static tether force values for control, noco beaded and lat-A treated axon populations. Each population consists of 12 tether force measurements (denoted by green open circles), conducted on 12 different axons. On each box, the central mark (red line) is the median, the edges of the box are the 25th and 75th percentiles and the whiskers extend to the most extreme data points. The spread in the f_0 values is due to the cell to cell variation. In addition, the f_0 for a given axon also varies with the location of the tether base along the axon. This variation, being very difficult to quantify, reduces the precision of f_0 measurements. Thus it is difficult to decide the level of significance of the observed rise in f_0 after nocodazole treatment. Surely, the apparent rise is much smaller compared to the almost 100 fold rise in the tether force required to trigger the pearling instability as discussed in Chapter 2 and therefore can not be the cause of the shape transformation of the axon. Lat-A treatment reduces f_0 by 40%, in agreement with [6].

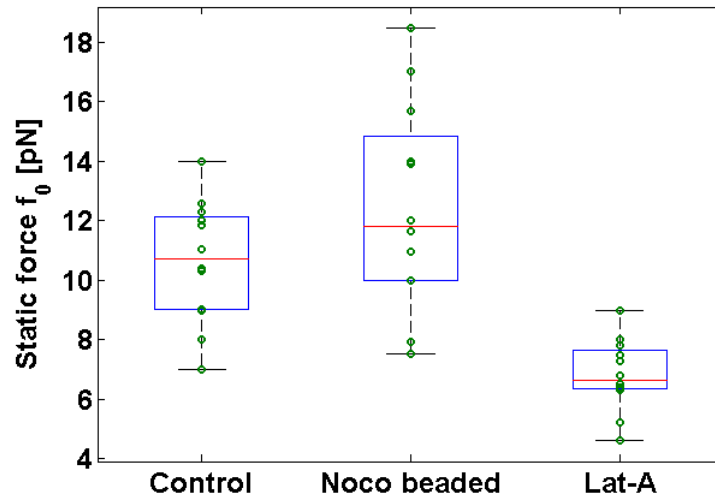


FIGURE 4.11: Distribution of static tether force f_0 for control, nocodazole beaded and lat-A treated axon populations (sample size : 12 each). Each green open circle corresponds to f_0 measured on a different axon. On each box, the central mark (red line) is the median, the edges of the box are the 25th and 75th percentiles and the whiskers extend to the most extreme data points.

In the experiments described in the following sections, a tether of $2 - 5 \mu m$ length is first formed and after the force has stabilized a subsequent pull is applied in order to elongate or to slide the tether in an almost step-like fashion.

4.4.2 Dynamic response to Step-displacements

I. Force relaxation after step-elongation of a tether

A step-elongation ΔL of 2 to $5 \mu m$ of a pre-formed tether at the rate of $10 \mu m s^{-1}$ applied to a tether results in a sudden hike in the tether force which gradually relaxes back to the static force value f_0 as shown in fig. 4.12A. In a few trials we observed that the force relaxed back to f_0 even after multiple elongations in steps of about $5 \mu m$ as shown in fig. 4.12B.

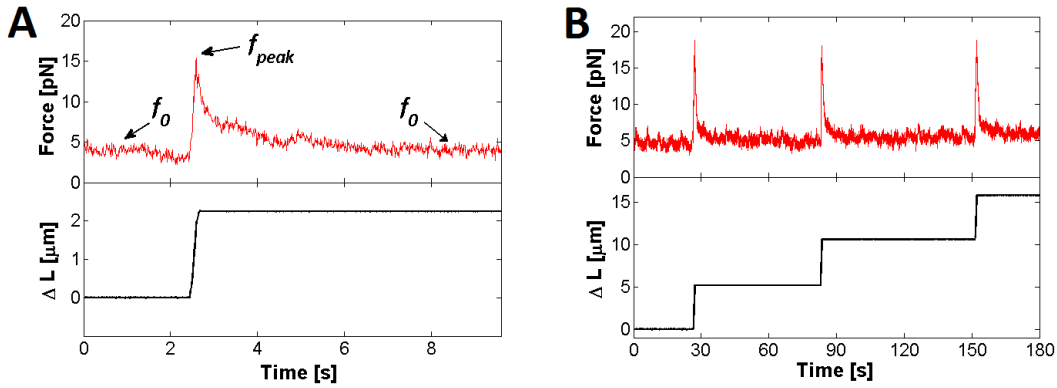


FIGURE 4.12: (A) Evolution of the tether force upon tether elongation. Upper panel shows evolution of tether force with respect to application of a step-like elongation ΔL at speed $10 \mu\text{m s}^{-1}$ as shown in the lower panel. (B) Multiple elongations of a tether. Upper panel shows evolution of tether force with respect to multiple tether elongation by length ΔL as shown in the lower panel. The force can be seen to relax to almost the same value after every step.

Force relaxation behaviours similar to that shown in fig. 4.12 have been reported in many different cell types like outer hair cells [9], E.coli [10] and red blood cells [8]. However, the single exponential function used in these works does not make a good fit to the force relaxation data in our experiments on axonal membrane. There has been an attempt in multi-component synthetic vesicle systems by Campillo et al. at fitting a similar force relaxation behavior to two well-separated relaxation time scales [7]. They conjectured that the fast time scale is an effect of the intermonolayer friction (as theoretically formulated in [5]) whereas the slower time scale comes from an unknown diffusive process over the length of the tether. We now discuss different possible relaxation mechanisms and the associated time-scales.

The force relaxation behavior can be understood by considering relaxation of a tension gradient along a tubular membrane structure with membrane reservoir(s) at its end(s). It has been shown that the tension equilibration in such a case takes place mainly through two diffusive modes called as peristaltic and Lucassen modes [25]. The peristaltic mode defines the time scale over which the shape of the tube adjusts to the external conditions, with diffusion constant $D_p = RT/8\eta$ and a characteristic time $\tau_p = \Delta L^2/(4\pi^2 D_p)$ where R is the equilibrium tether radius, ΔL is the wavelength of the mode, and η is the viscosity of the fluid which fills the tube. For a membrane tether, $R = \sqrt{B/2T}$. For our system, $R \sim 0.1 \mu\text{m}$ and viscosity of the cytoplasm $\sim 10^{-3} \text{N.s.m}^{-2}$, giving $D_p \sim 50 \mu\text{m}^2\text{s}^{-1}$. For the

longest wavelength mode, $\Delta L \sim 5 \mu m$, and the corresponding relaxation time $\tau_p \sim 10^{-2} s$. Note that the inter-monolayer friction, which can play a role in the peristaltic mode, does so at sub-micron wavelengths. Thus, the corresponding relaxation time scale will be even smaller than $10^{-2} s$ implying that in the present work, the inter-monolayer friction cannot be at play.

The other mode which is called Lucassen mode defines the time scale over which the membrane density (number of lipid molecules per unit area) and the membrane tension reach local mechanical equilibrium by adjusting the membrane crumpling amplitude. It is very fast and controlled by the diffusion constant:

$$D_T = \frac{ER(2 \log(\frac{L}{R}) - 1)}{8\eta} \quad \text{with} \quad E = \frac{8\pi BT}{k_B \Theta}$$

where E is the entropic stretching modulus of the membrane [26], L is the tether length, η is the fluid viscosity, and Θ is the absolute temperature. Typical time required for the membrane density to adjust over the whole tether is $\tau_T = \Delta L^2 / (4\pi^2 D_T)$. For our experimental system at $37^\circ C$, the order of magnitude estimate are $D_T \sim 10^{-7} m^2 s^{-1}$ and $\tau_T \sim 10^{-4} s$. Considering these significant modes of relaxation, it is clear that in a one-component membrane system, the tether force and the membrane tension would relax much faster than what is observed from our experiments (fig. 4.12).

In a two-component membrane, apart from the peristaltic and the Lucassen modes there exists one more mode of tension relaxation coming from the concentration gradient of the two components. For simplicity, we consider the case where one component has a much smaller surface density than the other. In this limit the tension T of a membrane composed of a majority constituent with concentration ϕ_1 and minority constituent with concentration ϕ_2 (such that $\phi_1 \gg \phi_2$) has the following form:

$$T = T_1(\phi_1) - \phi_2 k_B \Theta \quad (4.9)$$

where the first term is the tension corresponding to the pure majority constituent and the second term is a reduction brought in by the two-dimensional osmotic pressure of the second constituent.

We propose a model for the tether force relaxation mechanism, which is applicable whenever there is a gradient in the membrane composition from the axon to the tether. We make a hypothesis that the neck region at the base of the tether, where there is a sharp change in the membrane curvature, acts as a potential barrier for the ϕ_2 component. Therefore, immediately after tether formation the part of the tether next to the neck region will sense a membrane tension $T = T_1(\phi_1(y_{neck}))$ as $\phi_2 = 0$ due to the neck barrier (see fig. 4.13(a)). The tether is parallel to the Y-axis as mentioned before and y_{neck} defines the location of the tether neck. Since the chemical potential for the majority component can quickly equilibrate on both sides of the barrier, $\phi_1(y_{neck})$ is close to its equilibrium value ϕ_1^{eq} in the axonal membrane.

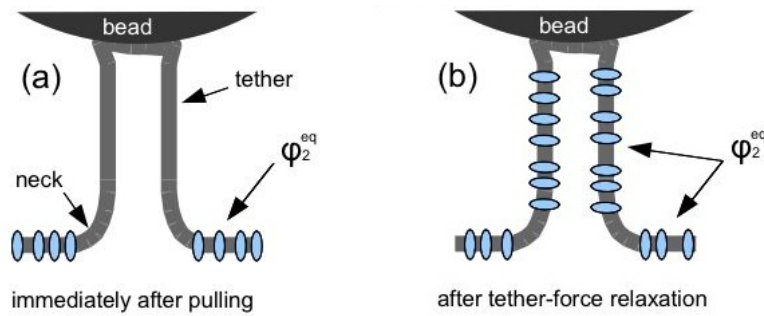


FIGURE 4.13: Schematic showing the evolution of the density of the minority component ϕ_2 subsequent to tether elongation. (a) Immediately after tether formation (or elongation) the concentration ϕ_2 in the tether is below the equilibrium concentration. (b) The tether force relaxes as molecules of the minority component cross the barrier and ϕ_2 equilibrates on both sides of the tether neck.

Mechanical equilibrium at constant constituent composition is reached on the time scale corresponding to the peristaltic mode, which is about a few tens of milliseconds. This means that the tension adjusts to the value $T_1(\phi_1(y_{neck}))$ all along the tether including the region where $\phi_2 = 0$ as well as in the initially pulled region where $\phi_2 = \phi_2^{eq}$ (when an existing tether is elongated). This is achieved by adapting the membrane crumpling in order to maintain the total tension homogeneous along the tether. At this point, the tether force $f = 2\pi\sqrt{2BT_1(\phi_1(y_{neck}))}$. The subsequent force relaxation results from the progressive increase in ϕ_2 as the molecules of the second component cross the barrier at the neck (fig. 4.13(b)). The flux of the second (or minority) component J may be modelled in a simple

way by

$$J = \lambda(\phi_2^{eq} - \phi_2(y_{neck})) = -D_m \frac{\partial \phi_2}{\partial y} |_{y_{neck}}$$

λ is a dynamic parameter characterizing the barrier, akin to the reciprocal of Kapitza resistance in solid state physics. With the initial condition $\phi_2 = 0$ and the Ficks law

$\frac{\partial \phi_2}{\partial t} = D_m \frac{\partial^2 \phi_2}{\partial y^2}$ one obtains

$$\phi_2(y_{neck}, t) = \phi_2^{eq} \left(1 - e^{t/\tau_{cross}} \left(\text{erfc} \sqrt{\frac{t}{\tau_{cross}}} \right) \right)$$

with a cross-over time $\tau_{cross} = D_m/\lambda^2$. Here, erfc is the complementary error function. This expression is approximate in the sense that it neither takes into account the finite size of the depleted region nor the total tether length. It is valid when the diffusion time taken for tether length 5-10 μm is significantly longer than τ_{cross} . If we assume this to be the case, we obtain from eq. 4.9

$$T = T_1(\phi_1^{eq}) - \phi_2^{eq} \left(1 - e^{t/\tau_{cross}} \left(\text{erfc} \sqrt{\frac{t}{\tau_{cross}}} \right) \right) k_B \Theta$$

Using this along with eq. 4.6 we can write the tether force as

$$f(t) = \sqrt{f_{peak}^2 - (f_{peak}^2 - f_0^2)g(t/\tau_{cross})} \quad (4.10)$$

where, the peak force f_{peak} is the tether force immediately after the step-elongation and in this model,

$$f_{peak} = f(t = 0) = 2\pi \sqrt{2BT_1(\phi_1^{eq})}$$

Where f_0 as defined earlier, is the force value after stabilization and in this model,

$$f_0 = f(t = \infty) = 2\pi \sqrt{2B(T_1(\phi_1^{eq}) - \phi_2^{eq} k_B \Theta)}$$

and $g(t/\tau_{cross}) = 1 - e^{t/\tau_{cross}} \left(\text{erfc} \sqrt{\frac{t}{\tau_{cross}}} \right)$. Eq. 4.10 gives a satisfactory fit to the force relaxation curves as shown in fig. 4.14A, giving f_{peak} , f_0 and only one time scale τ_{cross} which is of the order of one tenth of a second as the outputs (Table

S1). The force can be scaled using the relation

$$f_{sc}(t) = \frac{f(t) - f_0}{f_{peak} - f_0} \quad (4.11)$$

so that data from different trials can be seen to overlap (fig. 4.14B), indicating that τ_{cross} falls in a narrow range of values for control cells.

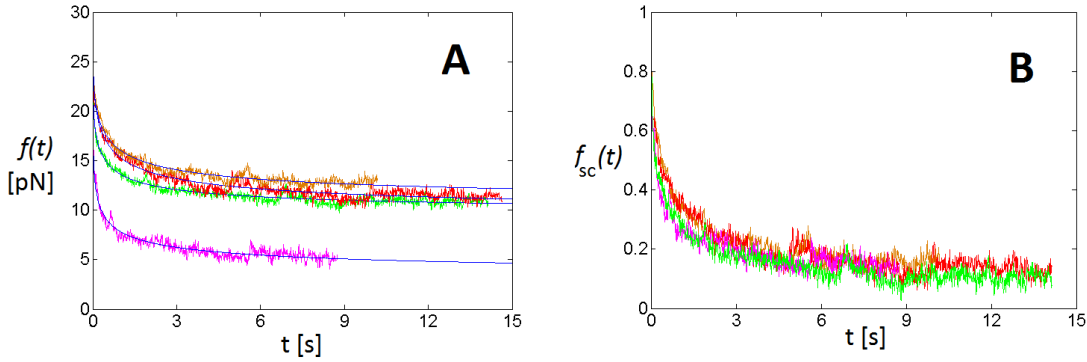


FIGURE 4.14: (A) Relaxation of tether force after a step-elongation applied at $t = 0$. Each color corresponds to a different axon. The corresponding fitting curves obtained using eq. 4.10 are shown in blue. (B) Rescaled force (eq. 4.11) for the four data in (A)

The barrier crossing time value $\tau_{cross} = D_m/\lambda^2$ allows us to estimate the amplitude of the potential barrier seen by the diffusing molecules. With $\lambda = \frac{D_m}{R} \exp(-\frac{W_b}{k_B\Theta})$ where the pre-factor is imposed by scaling, the tether radius $R \sim 0.1\mu\text{m}$ and $D_m \sim 1\mu\text{m}^2\text{s}^{-1}$ [27] we obtain a barrier height W_b of a few times $k_B\Theta$. Matching the experimentally measured values requires $\phi_2 \sim 5 \times 10^{-15}\text{m}^{-2}$ i.e. the typical distance between minority molecules to be of the order of $25 - 30\text{nm}$. This is a small concentration for nano-meter size molecules, justifying our basic approximation. Thus our simple model works surprisingly well. There are many more components in a cell membrane and it would not be surprising to observe a distribution of the corresponding crossing times. What we see here is clearly the diffusion of the slowest component, which turns out to be well separated from the others.

The connection between membrane and the cytoskeleton may have an additional effect on the force relaxation behavior. Our experiments on axons in which f-actin was disrupted using Lat-A (fig. 4.15) or microtubules were disrupted using Noco (fig. 4.16) show that the relaxation behavior still involves a similar dynamics but the values of the barrier-crossing time τ_{cross} are affected by the cortical integrity

(Table 4.1). Particularly, the cross-over time seems to be smaller in the case of Lat-A treated axons in comparison with the control axons (fig. 4.17).

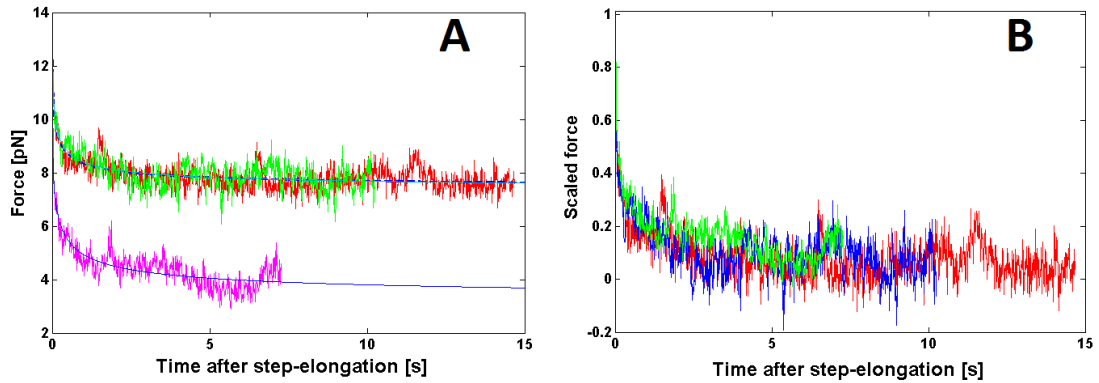


FIGURE 4.15: (A) Relaxation of tether force after a step-elongation applied to tether pulled from Lat-A treated axons at $t = 0$. Each color corresponds to a different axon. The corresponding fitting curves obtained using eq. 4.10 are shown in blue. (B) Rescaled force (eq. 4.11) for the four data in (A)

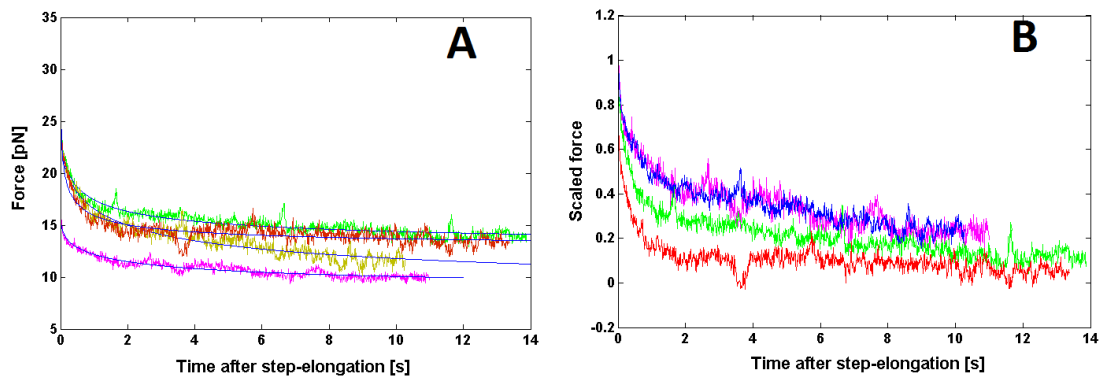


FIGURE 4.16: (A) Relaxation of tether force after a step-elongation applied to tether pulled from Noco treated axons at $t = 0$. Each color corresponds to a different axon. The corresponding fitting curves obtained using eq. 4.10 are shown in blue. (B) Rescaled force (eq. 4.11) for the four data in (A)

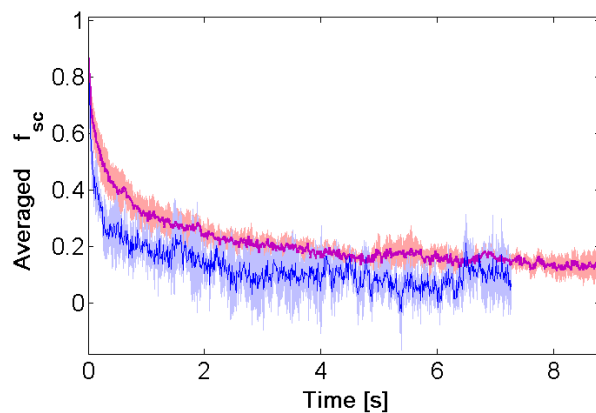


FIGURE 4.17: Force relaxation after tether step-elongation for control axons (purple, averaged over $n = 4$) and Lat-A treated axons (blue, averaged over $n = 3$). Force values are rescaled using eq. 4.11. The corresponding shaded regions around each trace show the standard deviation in the data at each time point.

Treatment	Serial No.	Adjusted R^2 value for the fit	Outputs of the fit		
			f_0 [pN]	f_{peak} [pN]	τ_{cross} [s]
Control	1	0.9297	9.313	24.42	0.132
	2	0.917	2.727	20.7	0.0539
	3	0.924	9.011	27.31	0.1945
	4	0.9424	10.24	26.49	0.2493
Lat-A	5	0.4887	7.364	13.25	0.0520
	6	0.5356	7.312	13.82	0.0517
	7	0.7419	3.121	11.12	0.0545
Noco	8	0.8759	8.273	15.67	1.193
	9	0.90	12.4	25.81	0.354
	10	0.9151	7.407	25.05	0.7241
	11	0.79	12.48	30.23	0.0555

TABLE 4.1: Outputs of the fit to tether force relaxation after step elongation

To conclude, the mechanism of tether force relaxation after a step elongation can be explained purely from gradients formed in the membrane composition. This is consistent with the results obtained from tethers pulled from lipid vesicles with an impurity species in the membrane [7]. It is conceivable that if the actin binding proteins present in the membrane contribute to the barrier at the tether neck, the

presence/absence of actin can modify the value of the cross-over time, without fundamentally changing the form of the force relaxation.

II. Tether sliding

In order to further explore the effect of membrane-cortex interaction on tether dynamics we studied the response of tethers to a lateral step-displacement of the axon, resulting in tether sliding on the surface of the axon as shown in the movie *tether-sliding* and in fig. 4.18. A stable tether is formed on a axon which is parallel to X-axis (fig. 4.18(i)). The stage is then given a step-displacement along +X with respect to the fixed optical trap (fig. 4.18(ii)) and the evolution of the tether is recorded as a function of time. Lateral displacement of the stage also results causes elongation of the tether (fig. 4.18(ii)) because of change in the orientation. We observed that in more than 70% of the cases (fig. 4.20), the base of the tether is able to slide along the axon until the tether once again becomes perpendicular to the axon (fig. 4.18(iii, iv)). A sequence of images before and after sliding is shown in the lower panel of fig. 4.18. The white arrows points to the location of the tether base just before the step displacement. In some cases, after the step displacement is applied, the base of the tether shows a time-lag before moving or sometimes it gets stuck so that any subsequent movement of the sample stage results only in elongation of the tether.

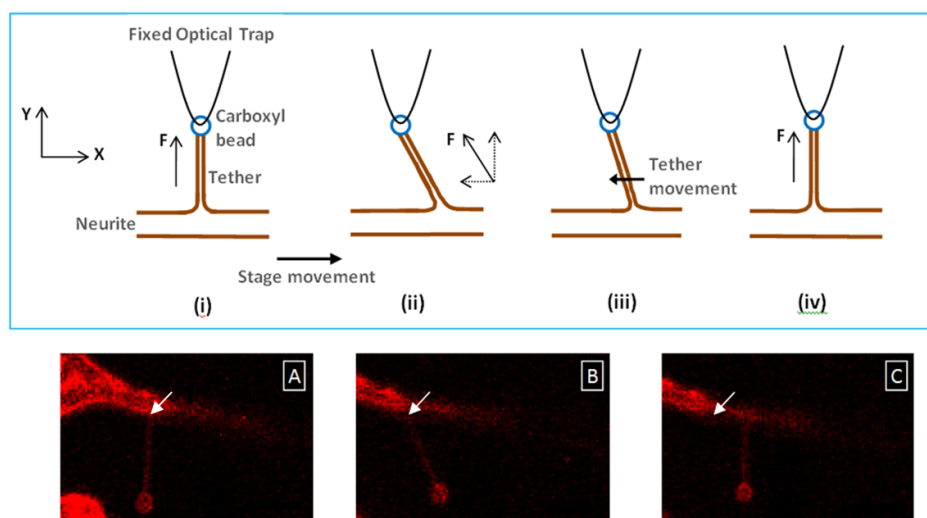


FIGURE 4.18: The upper panel shows a depiction of tether step-sliding experiment. (i) From a axon parallel to X axis a tether is pulled along Y axis (ii) The axon is displaced along $+X$ almost instantaneously. The tether base is stationary with respect to the axon, making the tether slant and elongated. (iii, iv) Tether base slides along X approaching the perpendicular orientation with respect to the axon. Lower panel shows confocal images of a tether (a) just before the step, (b) just after the step where the white arrow points to the location of the tether base on the axon, and (c) after the tether base slides where the white arrow still points to the earlier location of the tether base. Bar: $5\ \mu\text{m}$

Sometimes it can be seen that after a sliding step is applied, the tether base remains stuck on the axon for a while, then starts sliding. One such example is shown in fig. 4.19 wherein a step displacement is applied at $t = 0$ to the stage along X -axis while the tether was oriented along Y -axis. In this case the base of the tether remained stuck on the axon for about 20 s and then began to slide. Due to the applied step displacement to the stuck tether base there is sudden elongation of tether length which results into the peak in tether force at $t = 0$. Thus, the initial force relaxation within $t = 20$ s is similar to that seen in the step-elongation experiment whereas the subsequent relaxation (indicated by the arrow) is due to the tether sliding.

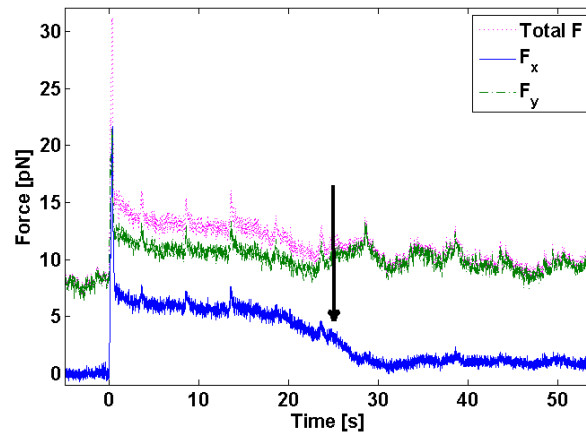


FIGURE 4.19: Force relaxation after a step-like displacement applied along X at $t = 0$ to an axon oriented along X and tether oriented along Y. The X-component of the tether force (F_x) is shown in Blue, Y-component (F_y) in Green and the total tether force (F) in Pink. The base of the tether is stuck till $t = 20$ s after which it slides (2030 s) and tether again becomes perpendicular to the axon. Thus F_x , F_y and F undergo relaxation like that after a step-elongation till $t = 20$ s and then F_x further relaxes due to the change in tether orientation while base of the tether slides

In some cases the tether base remains stuck over several minutes after a step displacement so that any subsequent displacement of the stage results only in elongation of the tether. When a tether is unable to slide for a time longer than the typical waiting duration of 4 to 6 minutes after the applied displacement and any subsequent displacement of the stage results only in an elongation of the tether, the trial is counted as an unsuccessful sliding trial and vice versa. The percentage of the number of successful trials is plotted as a function of the cytoskeleton drug treatments in fig. 4.20. Each trial is performed on a fresh axon. This can be compared with unpublished data by Dr. Thomas Bornschlöggl who inspected the behavior of tethers pulled from HeLa cells with respect to sliding. Tethers pulled from HeLa cells were held at an angle for 5 min. In this condition, 1 out of 5 trials resulted in tether sliding in untreated or control cells. When the cells were treated with Lat-A at a concentration higher than $1 \mu M$ for over 1 hour, 6 out of 8 trials resulted in tether sliding. However, in the case of axons, 70% of the control cells show tether sliding and this percentage is only slightly altered with Noco or Lat-A treatments (fig. 4.20). This is probably due to a sparse distribution of f-actin in the cortex of axons or due to a weak connection between the actin cortex and the axonal membrane. It is also seen that whether a tether can slide on the axonal surface depends upon the location of the tether base. The base may get stuck at

a point and take a few minutes before it slides but may slide without any delay at some other location. The behaviour points towards a heterogeneous cortex. We imaged the f-actin distribution in axons by fluorescent immuno-labelling (fig. 4.21) which is clearly seen to be inhomogeneous in comparison with microtubule and neurofilament distributions, which are uniform along the length of the axon (fig. 4.22).

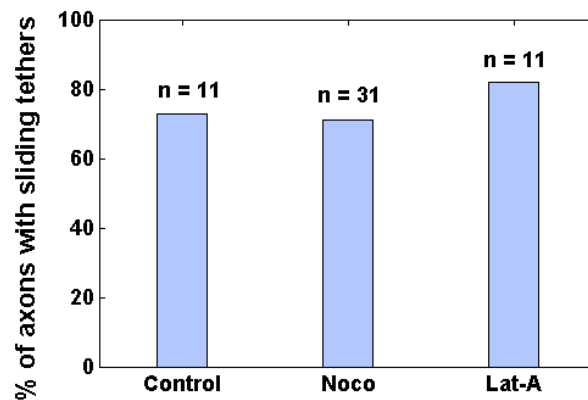


FIGURE 4.20: Comparison of percentage of number of trials in which a tether junction is able to slide within the experimental time of 4 to 7 min. after applying a step displacement to Control, Noco-treated and Lat-A treated neurons. n is the population size in each case.

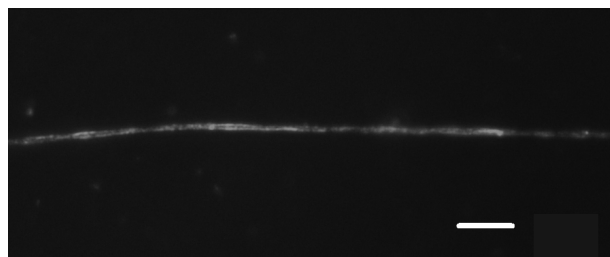


FIGURE 4.21: Fluorescently labelled f-actin in a fixed and permeabilized axon. Bar: $5\ \mu\text{m}$

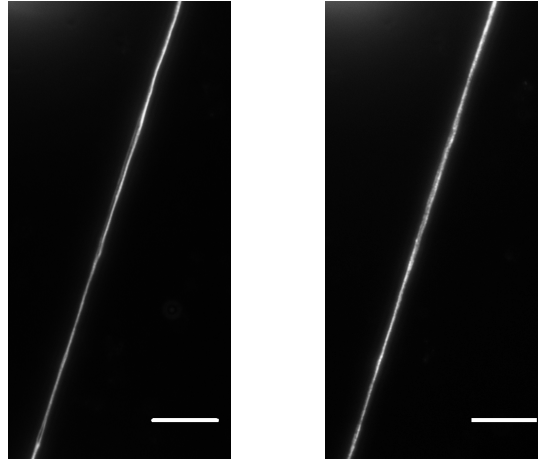


FIGURE 4.22: Fluorescently labelled β -tubulin (Left) and neurofilaments (Right) in a fixed and permeabilized axon. Bar: $5 \mu m$

During the sliding periods one can estimate the friction coefficient between the base of the tether and the axon. From the data of fig. 4.19, the sliding velocity of the tether base ($\sim 0.25 \mu m s^{-1}$) generates a force of the order of a pico-Newton. This corresponds to a friction coefficient $\mu \sim 4 \times 10^{-6} N.s.m^{-1}$. The contributions to friction may come from membrane viscosity, inter monolayer friction due to the differential motion between the two monolayers in the neck region and from the membrane-cortex interaction. Considering the friction originating from membrane viscosity only, one expects, ignoring pre-factors and log corrections, a friction term of the order of $e.\eta_m \sim 4 \times 10^{-10} N.s.m^{-1}$, where $e \sim 4nm$ and $\eta_m \sim 0.1 N.s.m^{-2}$ are respectively the thickness and viscosity of the plasma membrane [27]. This estimate shows that membrane viscosity plays a negligible role in the friction force. Simple scaling arguments suggest that the differential motion of monolayers contribute in a similar amount to friction and is thus also negligible. This suggests that the observed friction must be coming from membrane-cortex connection. Regions of higher cortical density or with stronger connectors may lead to high friction, thus acting as pinning sites for the lateral movement of a tether.

Apart from these passive responses of the axonal tethers, we also observe f-actin dependent spontaneous changes in the tether force as explained next.

4.4.3 Spontaneous dynamics

We report another novel feature of the dynamic nature of tethers pulled from axons in these experiments where the tether force is measured as a function of time without applying any displacement. We see that the tether force occasionally rises above the static force value till a point after which the force rapidly drops and settles back to the static force value. These events stand apart due to their peculiar slow-rise (over seconds) and rapid fall (in tens of milli-second) (fig. 4.23) as opposed to the fast rise and slow relaxation profile of the force seen in tether elongation or sliding experiments. We call them as spontaneous rises or spontaneous peaks in the tether force. For the results presented in the earlier sections, only those parts of the force traces devoid of such spontaneous peaks were considered.

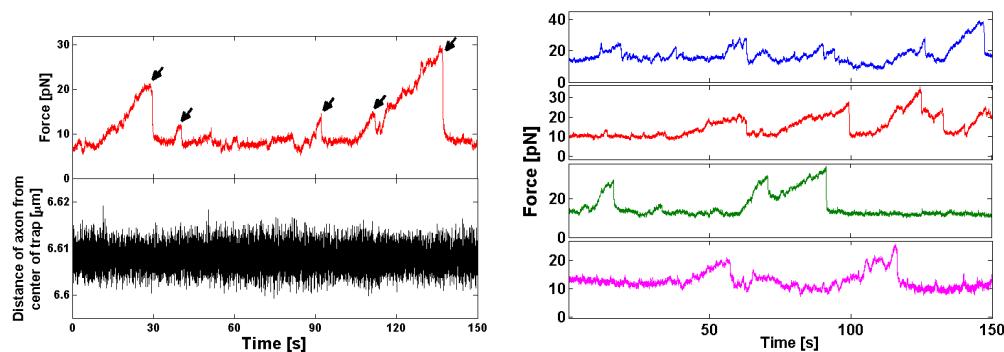
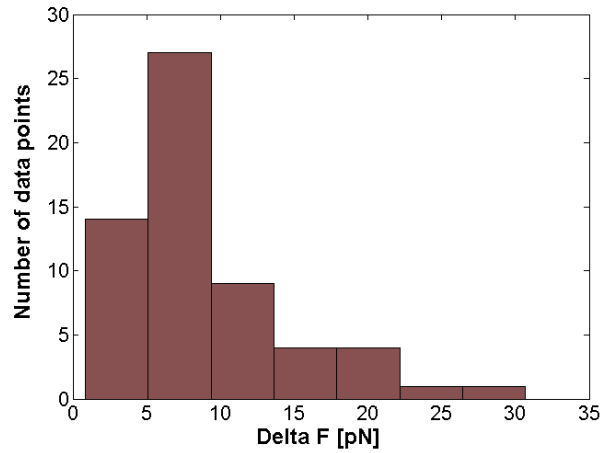


FIGURE 4.23: Left: Spontaneous force peaks (upper panel, pointed by black arrows) during a tether pulling experiment while distance between the axon and centre of the trap (lower panel) is held constant. Right: Tether force traces for four axons showing spontaneous peaks

It can be seen from fig. 4.23 that the peak force and the time intervals between consecutive peaks vary over a wide range. Often the peak force reaches high enough values to pull the bead out of the trap. We define Δf as the difference between the static force and the peak force just before the sudden drop. The wide distribution of Δf from about 2 to 35 pN is shown in fig.4.24.

FIGURE 4.24: Distribution of Δf for active peaks

Many of the spontaneous force peaks show almost linear rise with respect to time. Thus one can estimate the rate of the force build-up (Table 4.2) which is typically about $1 pN/s$ for control cells. For the following measurements we have chosen only the higher peaks ($\Delta f > 8 pN$).

Sr. No.	f_0 [pN]	f_{peak} [pN]	Δf [pN]	Rate of force rise [pNs ⁻¹]
1	7.0	21.0	14.0	0.69
2	8.2	29.8	21.6	0.67
3	11.7	36.9	25.2	1.83
4	16.2	40.5	24.3	1.69
5	9.0	18.0	9.0	1.88
6	16.2	27.5	11.3	0.99
7	13.2	29.7	16.5	1.97
8	11.5	21.6	10.1	0.65
9	5.0	15.5	10.5	3.1
10	10.0	21.3	11.3	0.47
11	10.9	27.7	16.8	0.99
12	15.0	37.5	22.5	0.81

TABLE 4.2: Values of static force, peak force and rate of force rise for spontaneous force peaks on tethers from different axons

We show in fig.4.25 that the occurrence of the spontaneous peaks is highly dependent upon the cytoskeleton integrity of the axon. Here we have plotted the percentage of axons which show spontaneous behaviour in control condition and under the action of different cytoskeleton perturbing drugs. It can be seen that while microtubule depolymerization using Noco does not significantly affect the spontaneous pulling behaviour, f-actin depolymerization using Lat-A clearly suppresses this feature, suggesting that f-actin is directly involved in the force generation process and microtubules may also play a minor role.

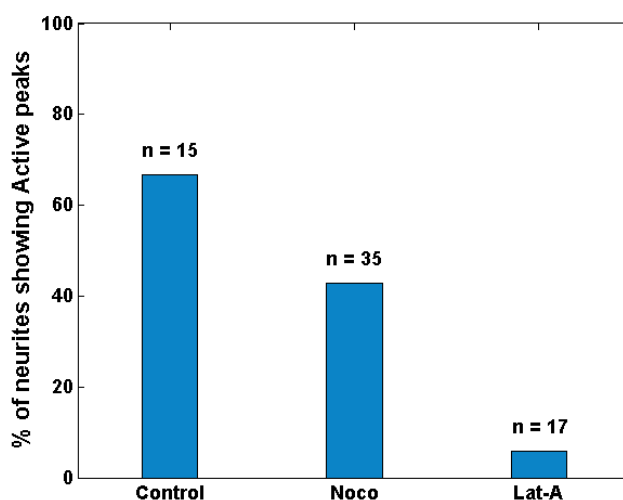


FIGURE 4.25: Percentage of axons showing spontaneous pulling forces on tethers. n indicates the sample size for each condition

Although nailing on the exact mechanism responsible for these force peaks demands further experiments focusing on the membrane-cytoskeleton interaction, we discuss the following possibilities.

- Endocytosis: This process transiently decreases the amount of plasma membrane and thus may give rise to transient increase in the tether force. It is also known that this is an active process and actin cytoskeleton is required at some important stages in endocytosis [28], [29]. However, it is clear from the tether elongation experiments that the tether force is almost independent of tether length, which is indicative of the presence of excess membrane to buffer the force. This, along with the fact that the force-relaxation time scales (less than a second) are far smaller than the observed time of the spontaneous

rise in force ($\sim 10s$) makes this an unlikely mechanism for the spontaneous peaks.

The next two mechanisms involve myosin motor activity. It is known that myosin type I, II, V, VI and IX are found in neurons [30]. There have been reports of un-conventional myosins contributing to membrane tension [31].

- Pulling via actin filaments inside the tether: This mechanism would depend on the presence of actin filaments inside the tether, being anchored in the cell cortex and making adhesive contact with the tip of the tether. It was recently shown in fibroblasts that actin can fill an initially empty membrane tube that was pulled from the cell membrane [32]. Such actin filled membrane tubes can show saw-tooth like pulling behaviour as it was observed in mast cells [19]. A similar saw tooth like pulling behaviour was observed in membrane tubes pulled from filopodia [20]. In actin filled membrane tubes, f-actin depolymerisation or active rearward movement of actin e.g. due to molecular motors such as myosin II mini-filaments or myosin V would automatically result in a force pulling on the bead (fig. 4.26(a)). With just a few motors the pulling force could match the experimentally observed one since these motors stall force is of the order of a few pico-Newton (typically 2.5 pN for myosin V). In this scenario, the observed force distribution could correspond to the statistical distribution of the number of bound motors.

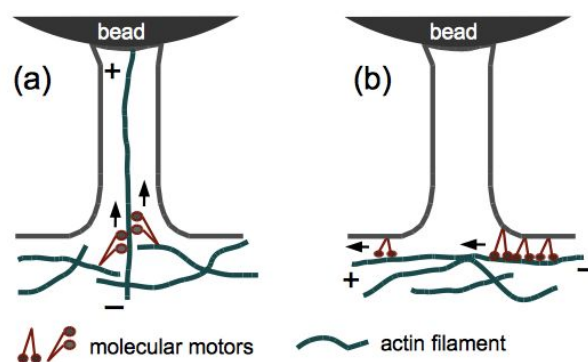


FIGURE 4.26: Proposed models for Myosin-driven generation of active force peaks. The arrows indicate the direction of the walking motors. (a) Actin filaments grow inside the tether and get attached to the bead. These are pulled by myosin motors present in the cortex. (b) Membrane bound motors like myosin I generate a torque on the membrane as they approach the neck of the tether. Motors moving away from the tether do not contribute to any force.

- Zipping effect due to membrane associated motors: There are processive, membrane binding motors like myosin Ia and myosin V [30] in neurons, which can walk on the cortical actin filaments and generate a torque at the base of a tether as shown in fig. 4.26(b). This is because motors walking towards the tether would produce a zipping effect due to a torque generated at the neck the tether in order to stay bound to both the membrane and the actin cortex. This torque will result in a spontaneous pulling force on the tether. The force is always of pulling nature irrespective of the orientation of the actin filament and the directionality of the motor (towards +/- end) because only those motors which move towards the tether neck contribute to the torque. The motors may act collectively as shown in fig. 4.26(b) and may detach stochastically in a force dependent manner, resulting in a sudden force drop with large fluctuations in the peak force due to the variation in number of motors at work at a given point of time. This behavior is to be expected for a small number of motors working co-operatively. The next occurrence of the force peak may depend upon the re-attachment of the motors at the base of the tether, which is a stochastic process. This mechanism also requires the presence of f-actin in the cortex for its operation but it doesn't require the actin filaments to grow in the tether.

4.5 Conclusion

We have explored various aspects of axonal membrane tension with a particular focus on the role played by the underlying cytoskeleton. We show that the tether force relaxation behavior in response to step-elongation of a tether can be explained by a model where the tether neck forms a potential barrier for a membrane component(s), thus giving rise to a gradient(s) in the membrane composition. This mechanism need not involve the cytoskeleton. Our experiments also reveal hitherto unreported features of axonal membrane, namely, the ability of tether-membrane junction to slide on axonal membrane and spontaneous saw-tooth like peaks in the tether force which are f-actin dependent. While the former finding suggests that the membrane-cortex linkage is weaker in axons compared

to other cell types where tether sliding is not possible, the latter points towards occasional bouts of the cortical activity. Recent high-resolution imaging of axons revealing actin organized as periodically arranged rings [33] highlights the significant structural differences between neuronal cells and other cell types. Further investigations where the cytoskeleton, especially the f-actin is imaged in live axons while the tethers are dragged along the axonal surface or while the spontaneous peaks occur are necessary to understand the mechanisms underlying these features. Photo-bleaching experiments may also shed light on the dynamics of cortical actin which may play a role in some of the effects described above. Such experiments are challenging in the view of small diameter of axons (about $0.5 \mu m$) but might be possible with the improving imaging techniques.

Bibliography

- [1] I Derenyi, G Koster, M M van Duijn, A Czovek, M Dogterom, and J Prost. Membrane nanotubes. *Lect. Notes Phys.*, 2007.
- [2] Thomas R Powers, Greg Huber, and Raymond E Goldstein. Fluid-membrane tethers: Minimal surfaces and elastic boundary layers. *Phys. Rev. E*, 65:041901, Mar 2002.
- [3] Imre Derényi, Frank Jülicher, and Jacques Prost. Formation and interaction of membrane tubes. *Phys. Rev. Lett.*, 88:238101, May 2002.
- [4] Gerbrand Koster, Angelo Cacciuto, Imre Derényi, Daan Frenkel, and Marileen Dogterom. Force barriers for membrane tube formation. *Phys. Rev. Lett.*, 94:068101, Feb 2005.
- [5] E. Evans and A. Yeung. Hidden dynamics in rapid changes of bilayer shape. *Chemistry and Physics of Lipids*, 73(12):39 – 56, 1994.
- [6] R M Hochmuth, Jin-Yu Shao, Jianwu Dai, and M P Sheetz. Deformation and flow of membrane into tethers extracted from neuronal growth cones. *Biophysical Journal*, 70(1):358–369, Jan 1996.
- [7] Clement Campillo, Pierre Sens, Darius Koster, Lea-Laetitia Pontani, Daniel Levy, Patricia Bassereau, Pierre Nassoy, and Cecile Sykes. Unexpected membrane dynamics unveiled by membrane nanotube extrusion. *Biophysical Journal*, 104(6):1248 – 1256, 2013.

- [8] W C Hwang and R E Waugh. Energy of dissociation of lipid bilayer from the membrane skeleton of red blood cells. *Biophysical journal*, 72:2669 – 2678, June 1997.
- [9] Zhiwei Li, Bahman Anvari, Masayoshi Takashima, Peter Brecht, Jorge H. Torres, and William E. Brownell. Membrane tether formation from outer hair cells with optical tweezers. *Biophysical Journal*, 82(3):1386 – 1395, 2002.
- [10] Liselotte Jauffred, Thomas Hnger Callisen, and Lene Broeng Oddershede. Visco-elastic membrane tethers extracted from escherichia coli by optical tweezers. *Biophysical Journal*, 2007.
- [11] D Raucher and M P Sheetz. Characteristics of a membrane reservoir buffering membrane tension. *Biophysical Journal*, 77(4):1992–2002, Oct 1999.
- [12] Bidisha Sinha and Darius K. Cells respond to mechanical stress by rapid disassembly of caveolae. *Cell*, 144(3):402 – 413, 2011.
- [13] S L Shyng, J E Heuser, and D A Harris. A glycolipid-anchored prion protein is endocytosed via clathrin-coated pits. *The Journal of cell biology*, 125(6):1239–1250, June 1994. PMID: 7911471.
- [14] Pramod A. Pullarkat, Paul Dommersnes, Pablo Fernández, Jean-Fran çois Joanny, and Albrecht Ott. Osmotically driven shape transformations in axons. *Phys. Rev. Lett.*, 96:048104, Feb 2006.
- [15] Jianwu Dai, Michael P. Sheetz, Xiaodong Wan, and Catherine E. Morris. Membrane tension in swelling and shrinking molluscan neurons. *The Journal of Neuroscience*, 18(17):6681–6692, 1998.
- [16] E Evans, H Bowman, A Leung, D Needham, and D Tirrell. Biomembrane templates for nanoscale conduits and networks. *Science*, 273(5277):933 – 935, August 1996.
- [17] D Cuvelier, I Derenyi, P Bassereau, and P Nassoy. Coalescence of membrane tethers: Experiments, theory, and applications. *Biophysical Journal*, 88:2714 – 2726, April 2005.

- [18] Baoyu Liu and Jin-Yu Shao. Tangential tether extraction and spontaneous tether retraction of human neutrophils. *Biophysical Journal*, 103:2257 – 2264, 2012.
- [19] Brenda Farrell, Feng Qian, Anatoly Kolomeisky, Bahman Anvari, and William E. Brownell. Measuring forces at the leading edge: a force assay for cell motility. *Integrative Biol*, 5:204–214, 2013.
- [20] Thomas Bornschlöggl, Stéphane Romero, Christian L. Vestergaard, Jean-François Joanny, Guy Tran Van Nhieu, and Patricia Bassereau. Filopodial retraction force is generated by cortical actin dynamics and controlled by reversible tethering at the tip. *Proceedings of the National Academy of Sciences*, 2013.
- [21] Alba Diz-Muoz, Daniel A. Fletcher, and Orion D. Weiner. Use the force: membrane tension as an organizer of cell shape and motility. *Trends in Cell Biology*, 23(2):47 – 53, 2013.
- [22] Simon F. Tolic-Norrelykke, Erik Schaffer, Jonathon Howard, Francesco S. Pavone, Frank Julicher, and Henrik Flyvbjerg. Calibration of optical tweezers with positional detection in the back focal plane. *Review of Scientific Instruments*, 77(10):–, 2006.
- [23] M. P. Sheetz and J. Dai. Mechanical properties of neuronal growth cone membranes studied by tether formation with laser optical tweezers. *Biophysical Journal*, 68:988–996, March 1995.
- [24] Bruno Pontes, Yareni Ayala, Anna Carolina C. Fonseca, Luciana F. Romo, Racele F. Amaral, Leonardo T. Salgado, Flavia R. Lima, Marcos Farina, Nathan B. Viana, Vivaldo Moura-Neto, and H. Moyss Nussenzweig. Membrane elastic properties and cell function. *PLoS ONE*, 8:e67708, 07 2013.
- [25] P. G. Dommersnes, O. Orwar, F. Brochard-Wyart, and J. F. Joanny. Marangoni transport in lipid nanotubes. *EPL (Europhysics Letters)*, 70(2):271, 2005.

- [26] R.M. Servuss, V. Harbich, and W. Helfrich. Measurement of the curvature-elastic modulus of egg lecithin bilayers. *Biochimica et Biophysica Acta (BBA) - Biomembranes*, 436(4):900 – 903, 1976.
- [27] Yegor A. Domanov, Sophie Aimon, Gilman E. S. Toombes, Marianne Renner, Francois Quemeneur, Antoine Triller, Matthew S. Turner, and Patricia Bassereau. Mobility in geometrically confined membranes. *Proceedings of the National Academy of Sciences*, 108(31):12605–12610, 2011.
- [28] Elizabeth Smythe and Kathryn R. Ayscough. Actin regulation in endocytosis. *Journal of Cell Science*, 119(22):4589–4598, 2006.
- [29] Drazen Raucher and Michael P. Sheetz. Membrane expansion increases endocytosis rate during mitosis. *J Cell Biol.*, 144(3):497–506, Feb 1999.
- [30] Paul C. Bridgman and Lisa L. Elkin. Axonal myosins. *Journal of Neurocytology*, 29(11-12):831–841, 2000.
- [31] Rajalakshmi Nambiar, Russell E. McConnell, and Matthew J. Tyska. Control of cell membrane tension by myosin-i. *Proc Natl Acad Sci U S A*, 106(29):11972–11977, 2009.
- [32] B. Pontes, N.B. Viana, L.T. Salgado, M. Farina, V.Moura Neto, and H.M. Nussenzveig. Cell cytoskeleton and tether extraction. *Biophysical Journal*, 101(1):43 – 52, 2011.
- [33] Ke Xu, Guisheng Zhong, and Xiaowei Zhuang. Actin, spectrin, and associated proteins form a periodic cytoskeletal structure in axons. *Science*, 339(6118):452–456, 2013.

Chapter 5

Summary and Outlook

So far we saw that axonal beading and retraction which are very commonly seen features of neuronal atrophies, can be mimicked in multiple and diverse ways *in vitro*, e.g. by application of mechanical perturbations like hypo-osmotic shock [1], dynamic stretch injury [2], laser ablation, by exposure to neuro-toxic factors like Nitric oxide [3] or in pharmacological way by treatment with Nocodazole (a microtubule disrupting drug) or Latrunculin-A (a f-actin disrupting drug). It should be noted that the underlying *physical* mechanism of the shape change may differ from case to case, depending upon the nature of the perturbation applied. In the case of osmotic shock and nerve stretching, the shape change has been shown to be due to an instability arising from a sudden rise in the membrane tension. The dynamic stretch injury causes local bending of microtubules at multiple locations along an axon, which later develop into sites of microtubule breakages and accumulation of vesicles and organelles, thus giving rise to beading. In rest of the cases concerning axonal beading and almost all cases of axonal retraction, the physical mechanisms underlying the shape change are poorly explored.

It is known that neuro-degenerative diseases like the Alzheimer's disease show signatures of malfunction with respect to microtubules organization or microtubule associated proteins and lead to axonal beading [4], [5]. The work described in this thesis attempts to investigate the process of axonal beading induced by Noco treatment. This is a clean way of specifically disrupting the MT structure and therefore it may throw some light on the mechanism of neuro-degeneration in the

cases of MT related neural disorders. It was previously hypothesized that Noco induced beading takes place due to disruption of microtubules tracks along the axon, leading to traffic jams in the intra-axonal transport [6]. However, this claim was made on the basis of electron micrographs of beaded nerves, without any emphasis on the dynamics of the process. Therefore, a more careful examination was required in order to determine the cause of the shape change.

This thesis also presents and discusses for the first time in our knowledge, the case of axonal retraction induced by exposure to Lat-A. It is seen that this retraction is often accompanied with bead formation, although the beads get merged with the retraction front and therefore the beaded appearance doesn't prevail for a long time as opposed to the case of Noco induced beading.

Apart from these pharmacological ways where the cytoskeleton disrupting drugs were applied globally to axons, we find axonal beading and retraction induced by a very local perturbation actuated by laser ablation of axons. The cases involving partial cut where the ablating laser leaves the membrane intact but creates a breakage in the cytoskeleton are of special interest. In such cases, the cytoskeleton alone shows retraction and beading within the membrane tube (see the movie *Partial_cut-intact-membrane-tube* which can be found at www.rri.res.in/thesis_Anagha_movies with username: thesis and password: An@rri_th in the folder chapt3).

A summary of the shape dynamics of axons induced in these three ways, namely Noco treatment, Lat-A treatment and laser ablation is depicted in fig. 5.1.

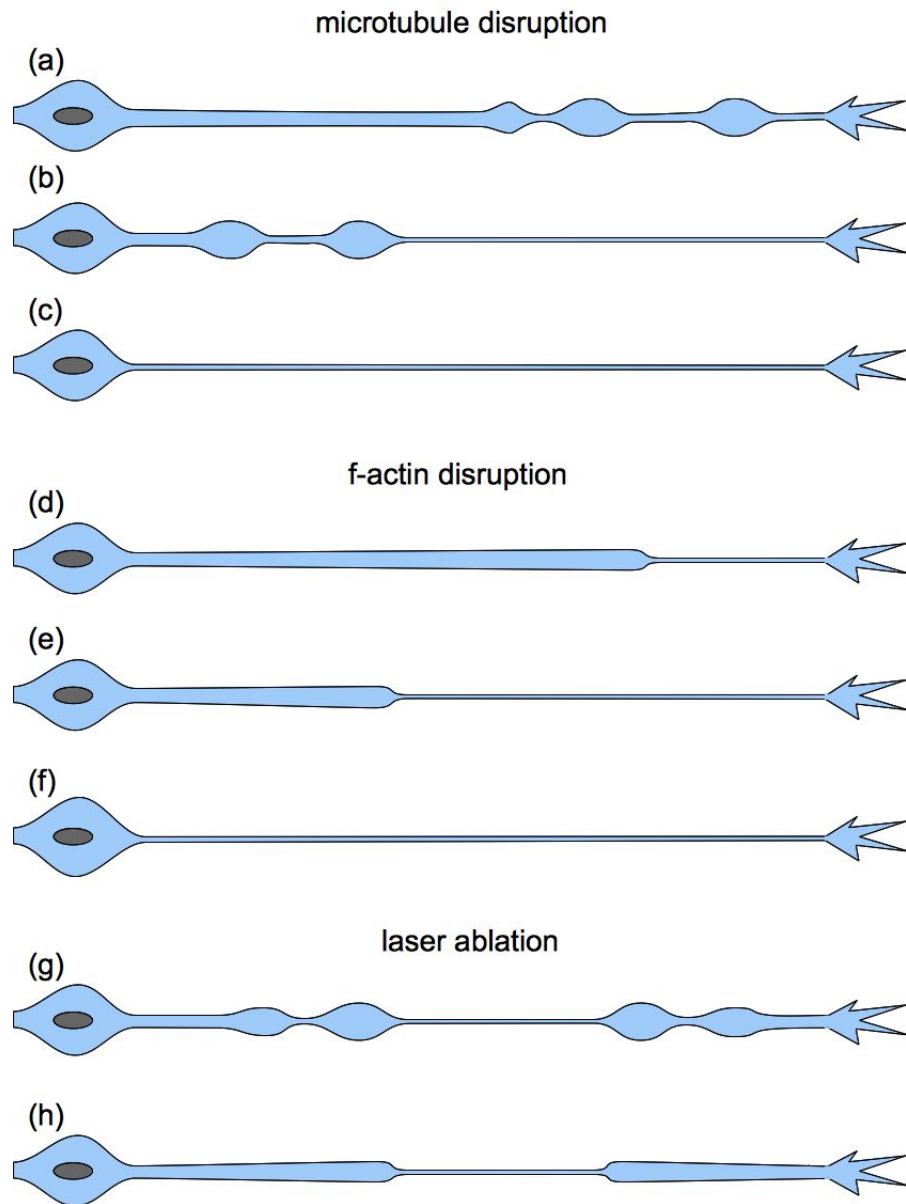


FIGURE 5.1: Different types of shape dynamics seen in axons after microtubule disruption using Nocodazole, f-actin disruption using Lat-A and Laser ablation at the centre of an axon. After MT disruption, (a) beading begins from the growth cone (GC) end, (b) beads start retracting towards the soma, (c) the material gets retracted into the soma leaving a thin tube behind. In the case of f-actin disruption (d) retraction begins from the GC, either with a clear retraction front or with bead formation (e) retraction proceeds towards the soma (f) all the material gets retracted in the soma, leaving a thin tube behind. In the case of partial laser ablation at the centre of an axon (g) beading and/or (h) retraction proceed away from the point of ablation in either direction.

Our experimental investigation helps ruling out some of the earlier proposed mechanisms of the shape change and narrow down to a few possible mechanisms which demand further experiments for validation. Even though the mechanism in each of these three cases has not been nailed down, our work gives a better insight into

the dynamics of axonal shape and stability and makes considerable progress in understanding the physical picture, as discussed in the following.

We have established that Noco induced beading is not caused by a fast rise in the membrane tension or by traffic jam of intra-axonal transport. Acto-myosin contractility also doesn't not have an essential role in this shape change. Membrane tension measurements reveal that axons have a small rest membrane tension T of the order of $10^{-6} N.m^{-1}$. This value does not change much after Noco treatment. The critical tension σ_c required for axonal beading which is a function of the bulk compressibility modulus K of the cytoskeleton can be estimated to be $\sim 1.7 \times 10^{-3} Nm^{-1}$ [1]. It shows that the rest membrane tension is far insufficient to cause beading if the cytoskeletal bulk modulus is unchanged. However, if the action of Noco mediates softening of the MT cytoskeleton, thus drastically reducing the value of K and hence σ_c , it is possible that the cylindrical shape becomes unstable to a beaded shape, thus causing the shape to change. The non-periodic nature of Noco beading could be due to a differential reduction in the bulk modulus of the cytoskeleton along the axonal length. This aspect needs to be theoretically verified.

Fluorescence imaging of tubulin and neurofilaments shows that there is a complete reorganization of these two components in beaded axons. This suggests another possible mechanism of the shape change as follows. The MT-disrupting action of Noco relaxes a pre-stress stored in the axonal cytoskeleton, mainly MTs and NFs. Such a relaxation may lead to spatial reorganization or local condensation of the cytoskeleton, resulting in the observed beading.

To explore this hypothesis, we performed laser ablation on axons which results in snapping and retraction away from the point of ablation. A complete cut which creates a discontinuity in the membrane and the cytoskeleton can be expected only to relax the membrane tension. Therefore the observation of beading in such cases is puzzling and could be driven only by a sudden stress relaxation in the cytoskeleton. ATP depletion does not prevent beading or retraction in laser ablated axons, suggesting that the pre-stress must be stored in the passive processes.

In the case of partial cuts where there is a breakage in the cytoskeleton which still keeps the membrane tube intact, both beading and retraction have been observed. These shape changes are very similar in morphology to those seen after Noco treatment. Even though the membrane tube is intact in this case, the retraction and beading behaviour can not be accounted for by the small value of axon membrane tension alone. Therefore it shows that the cytoskeleton is indeed under a pre-stress. However, after laser ablation, the beads or the retracting fronts propagate away from the point of ablation in either direction, unlike in the cases of Noco and Lat-A treatment where the axons start beading or retracting from the GC. This suggests that the direction of bead formation or retraction may be set by gradients in the depolymerization rate (in the case of Noco or Lat-A) and by the changed boundary condition in the case of laser ablation. In both of these cases, the existence of a pre-stress in the cytoskeleton may cause the flow of material while the stress relaxes.

In laser ablation experiments on cells, it is not clear if the ablation at a spot could result in a long range perturbation or depolymerization of the cytoskeletal filaments. We cannot rule out possibility of chemical changes occurring inside an axon as a result of the ablation. For example, it is shown that laser irradiation can cause transient poration of cell membranes [7] through which Calcium influx can occur, owing to the huge difference between the extracellular (1 mM) and intracellular ($0.1\ \mu\text{M}$) concentration of free Calcium. The laser ablation is also shown to induce generation of Calcium waves by perturbing the Calcium storing organelles like mitochondria [7]. Through electron micrographs of mechanically transected axons it was shown that MT and NF structures in the vicinity of the transection get disrupted, possibly due to elevated levels of calcium in this region [8]. Therefore, more experiments are needed to probe the extent of cytoskeleton damage created after complete or partial laser ablation of axons.

Another possibility for the reorganization of NFs may lie in the observations of phase transition of NF networks from gel expanded to gel condensed state due to change in the osmotic pressure [9]. Noco mediated disruption of MTs or the action of laser may lead to changed osmotic conditions, thereby triggering condensation of axonal NFs.

Beading and retraction result in a complete atrophy of the axonal cytoskeleton as shown by the fluorescent imaging in both Noco treated and lat-A treated axons. One may wonder what drives this process. As already mentioned, stress relaxation in the cytoskeleton can cause directional retraction. Another driving force may come from the membrane tension itself. It is known that membrane tethers pulled from synthetic vesicles, cells or axons attain a uniform cylindrical shape at equilibrium with a characteristic radius (eq. 4.2, Chapter 4). This is because the energetics prefer a thin tube connected to the vesicle or the cell body as it minimizes the surface area. Thus, if the cytoskeletal rigidity is affected such that it becomes a viscoelastic fluid as opposed a viscoelastic solid, then the membrane tension can drive material into the cell body driving the system towards equilibrium at long time scales. Besides this, we observe coalescence of beads and it seems that neighbouring beads attract (they accelerate towards each other when the distance is short (few microns)). Bead merging can happen due to interactions mediated by membrane curvature (if the net curvature is reduced by merging of beads) or due to the pressure difference in neighbouring beads which can cause a flow from the smaller bead to the larger one due to Laplace effect. In our experiments the former mechanism is likely to be at play as we see a translocation of the beads before merger.

We have shown that studying the dynamics of beading as well as probing physical properties of the membrane and the cytoskeleton is important in understanding the beading process. We demonstrate a new method to test these processes by laser ablation. The fact that we can cut the cytoskeleton leaving the membrane intact provides important hints regarding the beading or retraction mechanism. Furthermore, these multiple methods show that beading and retraction may be different morphological manifestations of the same driving mechanism. Such studies are of vital importance, as understanding these processes can provide clues to understanding axonal degeneration leading to atrophy.

Bibliography

- [1] Pramod A. Pullarkat, Paul Dommersnes, Pablo Fernández, Jean-Fran çois Joanny, and Albrecht Ott. Osmotically driven shape transformations in axons. *Phys. Rev. Lett.*, 96:048104, Feb 2006.
- [2] Min D. Tang-Schomer, Victoria E. Johnson, Peter W. Baas, William Stewart, and Douglas H. Smith. Partial interruption of axonal transport due to microtubule breakage accounts for the formation of periodic varicosities after traumatic axonal injury. *Experimental Neurology*, 233(1):364 – 372, 2012. Special Issue: Stress and neurological disease.
- [3] Yan He, Wenquian Yu, and Peter W. Baas. Microtubule reconfiguration during axonal retraction induced by nitric oxide. *Journal of Neuroscience*, 22:5982–5991, July 2002.
- [4] Gorazd B. Stokin, Concepcin Lillo, Toms L. Falzone, Richard G. Brush, Edward Rockenstein, Stephanie L. Mount, Rema Raman, Peter Davies, Eliezer Masliah, David S. Williams, and Lawrence S. B. Goldstein. Axonopathy and transport deficits early in the pathogenesis of alzheimer’s disease. *Science*, 307(5713):1282–1288, 2005.
- [5] Daphney C Jean and Peter W Baas. It cuts two ways: microtubule loss during alzheimer disease. *The EMBO Journal*, 32(22):2900–2902, 2013.

-
- [6] J R Jacobs and J K Stevens. Experimental modification of pc12 neurite shape with the microtubule-depolymerizing drug nocodazole: a serial electron microscopic study of neurite shape control. *The Journal of Cell Biology*, 103(3):907–915, 1986.
- [7] Shigeki Iwanaga, Tomoyuki Kaneko, Katsumasa Fujita, Nicholas Smith, Osamu Nakamura, Tetsuro Takamatsu, and Satoshi Kawata. Location-dependent photogeneration of calcium waves in hela cells. *Cell Biochemistry and Biophysics*, 45(2):167–176, 2006.
- [8] Micha E. Spira, Ruthi Oren, Ada Dormann, and Daniel Gitler. Critical calpain-dependent ultrastructural alterations underlie the transformation of an axonal segment into a growth cone after axotomy of cultured aplysia neurons. *THE JOURNAL OF COMPARATIVE NEUROLOGY*, 457:293–312, 2003.
- [9] Roy Beck, Joanna Deek, Jayna B. Jones, and Cyrus R. Safinya. Gel-expanded to gel-condensed transition in neurofilament networks revealed by direct force measurements. *Nature materials*, 9:40–46, November 2010.

Appendices

Appendix A

Cell culture, media preparations and Drug treatments

A.1 Primary DRG neurons

Eight day old chicken embryo dorsal root ganglia (DRGs) were dissociated using Trypsin with EDTA (Gibco 15400) dissolved in HBSS (without Ca, Mg) at the final concentration of 0.25%, then plated and grown on clean, uncoated glass coverslips in the growth medium described below. A good growth of axons (about 150 μm in length) is seen after 14 hours of incubation at 37 °C.

A.2 Culture media

1. Growth medium

L-15 medium (Gibco 11415) was made viscous by adding Methocel E4M (Col-orcon ID 34516) at 0.3 *gm* to 50 *ml* and stirring overnight at 4 °C. This was supplemented with 10% heat inactivated Fetal Bovine Serum (Gibco 10100) and 33.3 *mM* D-Glucose (Sigma G6152). For a good neurite growth, a Nerve Growth Factor NGF 7S (Invitrogen 13290-010) at the final concentration of 20 ng per ml was added to the cells seeded in the growth medium.

2. Medium without methocel

All the ingredients are exactly the same and in the same proportions as in the Growth medium except there is no methocel added. Thus this medium has water like viscosity. This medium was used for all the experiments where a drug was required to be added uniformly to a sample and its action on the cells was expected to begin at almost the same instant irrespective of the location of the cell in the dish. This medium was also used in all experiments where a flow chamber was used. It was seen that changing the medium from with methocel to without methocel itself induced a mild osmotic shock pearling of axons. This established that osmotic shock pearling can be induced by non-ionic entities.

3. NGF stock preparation

NGF 7S ((Invitrogen 13290-010) comes as a white powder, available in ampules containing $100\mu g$ each, to be stored at $-20^{\circ}C$. For making the stock solution, an ampule was first brought to the room temperature. $1 ml$ of L-15 medium supplemented with 10% FBS was directly added into the NGF ampule and mixed thoroughly using a micropipette till a transparent solution was obtained and stored at $-20^{\circ}C$ in aliquots of $10\mu l$ for up to one year. The secondary stock solution was made by adding $1\mu l$ of this to $500\mu l$ growth medium. $10\mu l$ of this was added per $1 ml$ growth medium for the overnight incubation of neuronal cultures to get the final concentration of $20 ng$ per ml.

A.3 Drugs and other treatments buffers

1. Nocodazole (Sigma M1404)

Nocodazole (Noco) comes as a white powder with a slight yellowish tinge, available in ampules containing $2 mg$ each, to be stored at $4^{\circ}C$. For preparing the stock solution at $16.7 mM$, an ampule was first brought to the room temperature to which $400\mu l$ pre-warmed DMSO was directly added and mixed thoroughly using a micropipette till a transparent solution with a yellow tinge was obtained and stored at room temperature in aliquots of $20\mu l$ for

up to 1 month. The appropriate concentration and exposure time of the drug were deduced by the characterization experiment as explained in Chapter 2.

2. Latrunculin A (Life Technologies L12370)

Latrunculin A (Lat-A) comes in a powder form, available in ampules containing 0.5 mg each, to be stored at -20°C . For preparing the stock solution at 0.47 mM, an ampule was first brought to the room temperature. 500 μl DMSO at room temperature was directly added to the Lat-A ampule and mixed thoroughly using a micropipette till a transparent solution was obtained. It was then stored at -20°C in aliquots of 10 μl or 5 μl for up to 6 months.

3. Blebbistatin (B0560 - Sigma-Aldrich)

Blebbistatin comes in a powder form, available in ampules containing 1 mg each, to be stored at -20°C . For preparing the stock solution, an ampule was first brought to the room temperature to which 500 μl DMSO at room temperature was directly added and mixed thoroughly using a micropipette till a transparent yellow solution was obtained. It was then stored at -20°C in aliquots of 10 μl or 5 μl for up to 6 months.

4. ATP depletion buffer

L-15 + 10 mM Sodium azide (Riedel-de Haën 13412) + 10 mM 2-Deoxy-D-glucose (Sigma D6134)